5-2009

Anisotropic electron-phonon coupling on a two-dimensional isotropic fermi contour [Gamma-bar] surface state of Be(0001)

Te-Yu Chien
University of Tennessee

To the Graduate Council:

I am submitting herewith a dissertation written by Te-Yu Chien entitled "Anisotropic electron-phonon coupling on a two-dimensional isotropic fermi contour [Gamma-bar] surface state of Be(0001)." I have examined the final electronic copy of this dissertation for form and content and recommend that it be accepted in partial fulfillment of the requirements for the degree of Doctor of Philosophy, with a major in Physics.

Ward Plummer, Major Professor

We have read this dissertation and recommend its acceptance:

Accepted for the Council:

Carolyn R. Hodges

Vice Provost and Dean of the Graduate School

(Original signatures are on file with official student records.)

To the Graduate Council:

I am submitting herewith a dissertation written by Te-Yu Chien entitled "Anisotropic Electron-Phonon Coupling on a Two-Dimensional Isotropic Fermi Contour: $\overline{\Gamma}$ Surface State of Be(0001)." I have examined the final electronic copy of this dissertation for form and content and recommend that it be accepted in partial fulfillment of the requirements for the degree of Doctor of Philosophy, with a major in Physics.

Ward Plummer

Major Professor

We have read this dissertation
and recommend its acceptance:

Takeshi Egami

Pengcheng Dai

Hanno Weitering

Jian Shen

Accepted for the Council:

Carolyn R. Hodges

Vice Provost and Dean of
the Graduate School

(Original signatures are on file with official student records.)

Anisotropic Electron-Phonon Coupling on a Two-Dimensional Isotropic Fermi Contour: $\overline{\Gamma}$ Surface State of Be(0001)

A Dissertation Presented for
the Doctor of Philosophy Degree
The University of Tennessee, Knoxville

TeYu Chien

May 2009

ACKNOWLEDGEMENTS

Graduate study at the University of Tennessee, Knoxville, was a very smooth program for me. When I was first admitted to the graduate program, I had no funding. At that time, my financial situation was very crucial, and my first and immediate goal was to find an assistantship position as soon as possible. My sincere thanks and appreciation go to Prof. Ward Plummer who let me join his research group even before I passed the qualifying exam. With Prof. Plummer's help, I was able to travel extensively to do experiments all over the world with visits to synchrotron facilities in Denmark, Berkeley, and Taiwan. Through collaborations with many top scientists, including Philip Hofmann, Norman Mannella, Wan-Li Yang, Sung-Kwan Mo, Timur Kim, Emile Rienks, Chen-Maw Cheng, Ku-Ding Tsuei, Shu-Jung Tang, Maria Jensen, and others, I was able to establish my own research style very gradually. I would like to thank them for their friendship and their scientific help. Prof. Plummer also advised me in many aspects of doing research. He never forced me to do things his way, but helped me in how to make my own decisions. Thus, I learned to be an independent researcher in his group. Again, I offer my appreciation to Prof. Plummer.

Throughout my graduate study, I have also had the full support of my family. My parents, Yi-Hui Chien and Mei-Hua Yang, and my older brother, Chao-Chan Chien, support me with all their hearts which allowed me to work hard in this foreign country without feeling lonely. Also, my fiancée, Chih-Yu, supported me without complaining about my hard working status.

In my early studies in Prof. Plummer's group, one person, Hong Liu, who was a postdoc working with Prof. Plummer, was instrumental to my success, and I would like to thank her. She helped me gain tremendous knowledge about UHV systems and many basic concepts, and she

traveled with me to Berkeley to do experiments. She also taught me how to use AutoCAD, a software in which she is an expert. Special thanks to Norman Mannella, who was the beamline manager when I doing experiment in Advanced Light Source. We do experiment overnight together and had very interesting discussion, in which I learn a lot about the angle-resolved photoemission spectroscopy. Also thanks to John Wendelken, who is my host in Oak Ridge National Laboratory (ORNL). His help facilitate my work in ORNL in any aspects. I would also like to thank our group members—Minghu Pan, Von Braun Nascimento, Xiaobo He, Rob Moore, Kenji Fuchigami, Zac Ward, Noppi Widjaja, Biao Hu, and Guorong Li. Through their participation, my research life is much richer, and I sincerely hope we will be research partners in our future careers.

ABSTRACT

Here, we studied an isotropic, free-electron-like 2D electronic band structure system—the Be(0001) $\overline{\Gamma}$ surface state. We revealed that the EPC on Be(0001) is anisotropic.

Mass enhancement factors are closely related to the strength of the electron-phonon coupling (EPC). Large values of mass enhancement factors represent a strong EPC. For beryllium, the mass enhancement factors, λ, of the surfaces are large when compared with the bulk values. However, the reported values of λ of the surfaces are inconsistent among the values obtained from different experiments or theories. One of the possible reasons is that λ is strongly $\vec{k}$-dependent. We did systematic measurements to understand that the inconsistency originated from the anisotropic nature of the EPC on the Be(0001) surface.

The details of EPC are described by Eliashberg function (ELF) – so called coupling function. This function describes the coupling between the electron and phonon as a function of energy and momentum. To understand the EPC, ELF is required to be extracted from angle-resolved photoemission spectroscopy experimental data. With a set of extra-high quality data, we accurately extracted the ELF for the Be(0001) $\overline{\Gamma}$ surface state for the first time. With comparison to the measured bulk and surface phonon density of states, we found that the bulk phonon contributes to the high energy part of the ELF; while the surface phonon contributes to the low energy part of the ELF. The contribution from the surface phonon to λ is found to be about 77%, equals to 0.72 out of the total value of 0.94.

To quantitatively extract λ we did simulations to understand the effects from the linear approximation used for analyzing data—from the energy and momentum resolutions in instruments and from the noise in the data. We concluded that (a) the linear approximation can work in a very wide range; (b) the momentum resolution plays a minor role in

determining λ ; (c) the energy resolution would severely distort the extracted dispersion near the Fermi energy and kink, hence, affecting the resulting λ ; and (d) λ is robust against the noise.

TABLE OF CONTENTS

Chapter **Page**

LIST OF TABLES

Table **Page**

LIST OF FIGURES

Figure **Page**

Chapter I
Introduction

Historical Review

Charge transportation in materials has drawn the attention of physicists since the electronic nature of materials was found—even before the electron was discovered (in the year 1897 by J. J. Thomson). In materials, electrons live in an environment full of ions and other electrons. The many-body nature of the electronic properties in materials has proven that the modeling of the electronic properties is a very difficult task. Among different materials, metals have the most common properties in the same category. For example, metal always has high electronic and high thermal conductivities. In the condensed matter physics, the Drude model, in which the electrons in metals were modeled as an electron gas without interactions (free electron gas), has described electronic properties for simple metals surprisingly well, despite the many-body nature of the electrons' environment in metals. Also, the Drude model uses classical statistics, the Maxwell-Boltzmann distribution, to perform calculations of the electronic properties of metals. It is surprise that the simple Drude model can model the properties of metals very well. Soon after the discovery of the Pauli exclusion principle for electrons, Sommerfeld applied quantum mechanics and the Fermi-Dirac distribution for the free electron gas model. With the more accurate modification, the Sommerfeld theory solved some puzzles that had been thrown out by the Drude model, such as the Wiedemann-Franz law. However, it still ignored the many-body nature of the electron environment in metals. A problem for the free electron gas model, including the Drude and Sommerfeld models, has been that it ignores the interactions between electrons and ions. As one consequence, the relaxation would not happen, because the

relaxation, in general, needs interactions in order for it to be achieved. A more complicated model is needed for materials with strong interactions between electrons and other degrees of freedom, such as spin, lattice, and orbital. For example, Landau's approach for electron-electron interactions is now referred to as the Fermi liquid theory.

In materials, ions are the other particles in addition to electrons. Because ions are heavier and less mobile particles than electrons, the electronic and thermal properties are more likely to be contributed from electrons. From this point of view, it seems that the function of the ions is just to hold the neutrality of the materials and nothing else. In fact, the ions play a much more important role in materials. First, the ion provides a periodic potential environment in crystals for electrons. This leads to electrons developing energy bands. A different structural symmetry of the lattice would result in a very different electron band structure. Further, ions can move, or more precisely, can vibrate around the equilibrium position. The vibration carries energy, and the energy can be quantized as the so-called "phonon." Phonons contribute to the thermal transportation and specific heat, and they rule the thermal expansion of the solid. Phonons also are the main source of the resistance when talking about the electronic properties in many solid materials. Electrons collide with phonons and transfer energy to phonons to generate the resistant heat. In fact, the specific heat is contributed from both the electrons and the phonons. At low temperatures, the specific heat is mainly from electrons, because the vibration of the ions would be frozen. At higher temperature ranges, the specific heat is mainly from phonons. The cross-over region can be given by [1]:

$$T_0 = 0.145\left(\frac{Z\Theta_D}{T_F}\right)^{1/2}\Theta_D \qquad (1\text{-}1)$$

where Z is the atomic number; Θ_D is the Debye temperature; and T_F is the Fermi temperature. In most cases, Z is a number less than 100; the

Debye temperature is on the order of room temperature; and the Fermi temperature is on the order of tens of thousands K. Hence, the typical T_0 is just a few percent of the Debye temperature. If you take beryllium as an example, Z = 4; Θ_D = 1000 K; $T_F = 16.6 \times 10^4 K$. Therefore, $T_0 = 0.0225\Theta_D = 22.5K$.

To model the phonon contribution to the specific heat, Albert Einstein constructed a phonon model—the so-called Einstein model—to describe phonons. The Einstein model assumes the phonon density of states (DOS) is a delta function at a certain energy, which is called the Einstein energy ($\hbar\omega_E$). However, because of the simplicity of the Einstein model, the description of the phonon DOS is not accurate enough and hence underestimates the specific heat of solid materials. Later, Peter Debye constructed a more sophisticated model, the so-called Debye model, to describe phonons. The Debye model shows the phonon DOS as a quadratic function of energy and has a cut-off energy, which is called the Debye energy ($\hbar\omega_D$); above it, there is no phonon. Although the Debye model has more structures in the phonon DOS, the model itself is still very simple. Surprisingly, the simple Debye model works for reproducing the specific heat quiet well. This is an indication that the actual phonon DOS is more similar to the Debye model than to the Einstein model. For comparison, figure 1.1 illustrates the schematic graph of the Einstein model and the Debye model DOS as well as the measured beryllium phonon DOS [2, 3]. For the case of the bulk beryllium, the phonon DOS agrees well with the Debye model, except some fine structures.

Other than simple metals, more complicated models are needed for understanding the physics of the condensed matter. Moreover, the interactions between these degrees of freedom in materials can no longer be neglected.

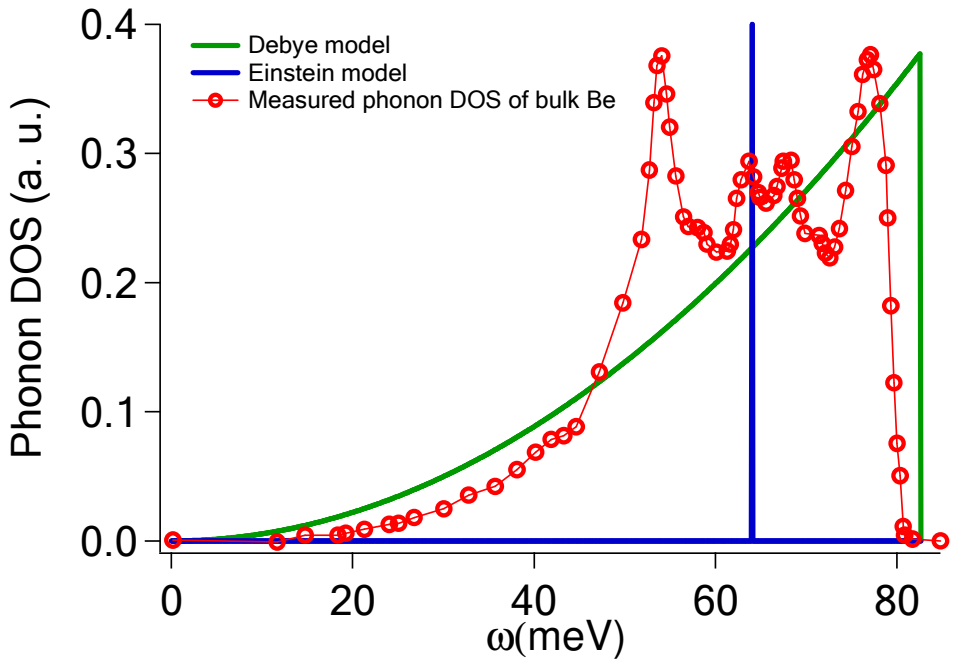

Figure 1.1. *Comparison of the Debye and Einstein models with measured bulk beryllium phonon DOS [2, 3].*

Complex Materials

In recent decades, the condensed matter community has focused on systems with strong interactions, such as the high-T_c superconductors [4–6], the colossal magnetoresistive (CMR) manganites [7], superconducting MgB_2 [8], and sheets of graphene [9]. This indicates that the interactions between different degrees of freedom could result in a variety of the functionalities. As a consequence, the way condensed matter physicists have considered physics has shifted from the concept of reduction to complexity [10]. Couple charge, spin, lattice, and orbital degrees of freedom together can emerge as functionalities. For example, coupled charge and lattice (electron-phonon coupling) can have BCS-type superconductors; coupled charge and spin (electron-spin coupling) can give spintronics, including CMR and the Kondo effect; and the Jahn-Teller effects are from the coupling between the lattice and orbital.

One of the most studied systems in the condensed matter community is the high-T_c superconducting materials [11]. The unusual transport properties of such materials originate from the strong coupling between the electrons and bosons. It is very similar to the BCS-type superconductors, in which strong EPC introduces superconductivity in the metal phase. Despite intense studies of the high-T_c superconductors, an outstanding question still remains unsolved: What kind of boson is responsible for the strong EBC in these materials? One of the most important techniques used for studying this issue is angle-resolved photoemission spectroscopy (ARPES) because of the great improvements in energy and angular resolution of the instruments. ARPES can be used to map out the Fermi contour as well as the energy-momentum dispersion relation in crystalline materials. From studies of the Fermi contour area, one can find the amount of the electron/hole doping [12] and the symmetry of the electron band nature [13]. From studies of the energy-momentum dispersion, one can directly map out the band structure [13] and can

determine the EBC coupling strength [14–22] and even the coupling function [14, 20].

One of the signatures of the EBC is the “kink” feature in the energy-momentum dispersion relation of the quasiparticles near the Fermi energy [1]. It is well-known that the energy where the kink appeared is related to the energy of the coupled bosons with the electrons. In the high-T_c materials, kinks were found in at least two different energy scales. Based on the energy, one is referred as the low-energy kink, which has an energy scale around several tens meV [for example, see the review article (Ref. [4]) and references therein]; while the other is referred as the high-energy kink [23–25], which has an energy scale around a few hundreds meV. The high-energy kink is attributed to the spinon and holon sources; while the low-energy kink is believed to be the key to understanding the secret of the high critical temperature of the superconductivity. However, the source of the coupling boson is still a mystery.

From studies of the kink in the energy-momentum dispersion, physicists already understand that the EBC is anisotropic in $\vec{k}$ space [26]. Figure 1.2 shows the first Brillouin zone (BZ) of the underdoped $Bi_2Sr_2CaCu_2O_{8+\delta}$ at temperatures (a) below T_c; (b) right above T_c, and (c) much higher than T_c. The (0,0) to (π,π) direction ($\overline{\Gamma}-\overline{Y}$ direction) is called the nodal direction; while the $(\pi,0)$ to (π,π) direction ($\overline{M}-\overline{Y}$ direction) is called the anti-nodal direction. The terminologies of “nodal” and “anti-nodal” are from the behavior of the momentum-dependent gap. When the temperature decreases toward the critical temperature, the gap starts to open from the anti-nodal direction and propagates toward the nodal direction [27]. The nodal direction is gapless even when the temperature is lower than the critical temperature. It is also found that the kink, which describes the EBC, behaves differently along the nodal and anti-nodal directions. Hence, the EBC on cuprates are considered as

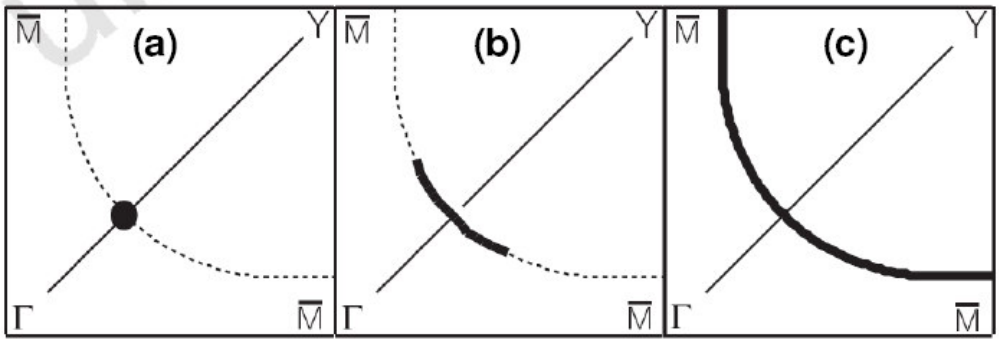

Figure 1.2. *The Fermi surface mapping for the underdoped* $Bi_2Sr_2CaCu_2O_{8+\delta}$ *at temperature (a) below* T_c*; (b) right above* T_c*, and (c) much higher than* T_c*. The* $\bar{\Gamma}-\bar{Y}$ *direction is referred to as the "nodal" direction; while the* $\bar{M}-\bar{Y}$ *direction is referred to as the "anti-nodal" direction. (From Ref. [27]).*

anisotropic. In BCS-type superconductors, the EPC is considered as an isotropic interaction, in which the Cooper pairs are *s*-wave [28–30]. From this point of view, phonons should be excluded as the candidates responsible for the EBC in high-T_c superconductors just because of the anisotropic nature of the EBC. However, recently, T. Valla et al. reported a result on the anisotropic EPC on the system of graphene on CaC_6 [9]. As shown in figure 1.3 (c), the kink is very different at different points in $\vec{k}$ space. The extracted mass enhancement factor (the coupling strength), figure 1.3 (d), shows that it is indeed anisotropic and follows the symmetry of the Fermi contour very well. The stronger coupling strength appears at the corner of the triangular-shaped Fermi contour. In this case, the only possible boson source in graphene is the phonon. This leads to another explanation for the anisotropic EPC—the anisotropic EBC/EPC might occur just because of the anisotropic nature of the Fermi contour, since the Fermi contours of the graphene and cuprates are anisotropic and the coupling strength follows the symmetry of the Fermi contour very well. This comes to the question of this thesis: Can a simple metal with isotropic Fermi contour have an anisotropic EPC?

Anisotropic EPC on the Isotropic Fermi Contour?

To address this question, we chose beryllium (Be) as an example for the following reasons: (1) Be is a simple metal with atomic number 4 and with the electron configuration $1s^2 2s^2$; (2) although the EPC in bulk Be is weak, the EPC on the Be surfaces are relatively strong, which is ideal for studying EPC; (3) Be has well-defined surface states, which are located in the gap of the bulk states, making the Be surface state an ideal sample for the EPC measurements; (4) one of the surface states, the $\overline{\Gamma}$ surface state of the Be(0001) surface, has a isotropic Fermi contour, offering a great test ground for the question we plan to address. With the help of the

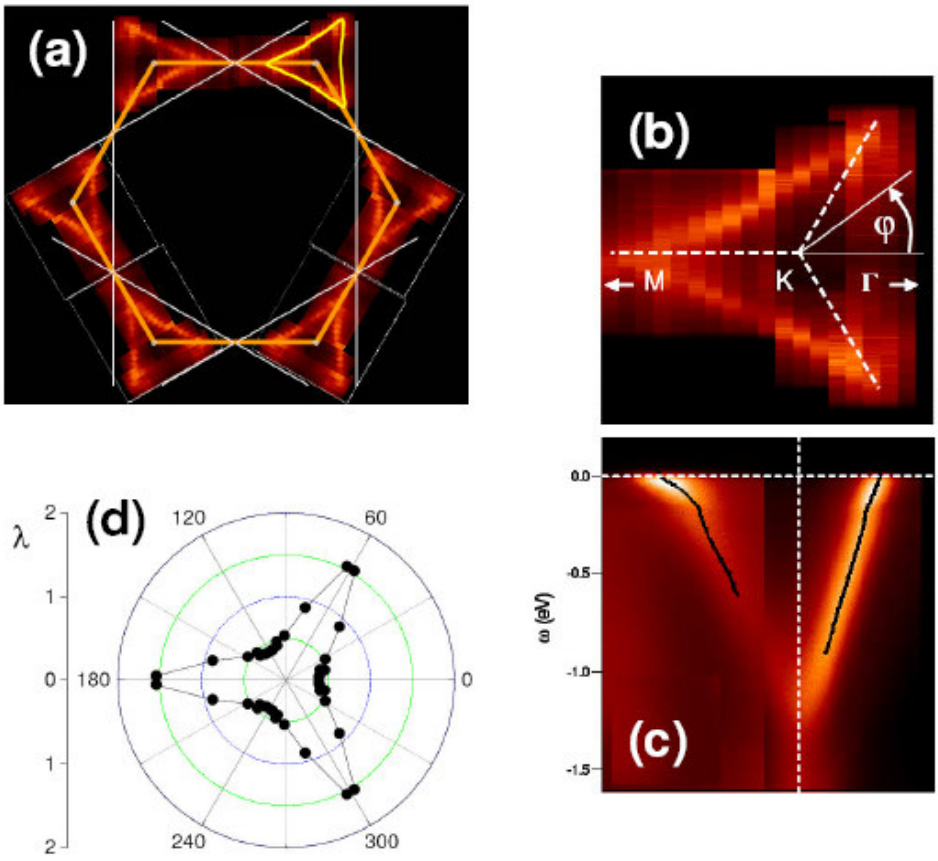

Figure 1.3. *(a) Fermi surface mapping for graphene on CaC_6 along with the corresponding surface Brillouin zone; (b) zoom-in view of the Fermi surface mapping onto a single triangular feature; (c) energy-momentum mapping along the $\overline{M}-\overline{K}-\overline{\Gamma}$ direction; (d) the extracted mass enhancement factor as a function of angle φ, defined in (b). (From Ref [9]).*

ARPES experimental technique, we demonstrate in this thesis that the EPC on this isotropic Fermi contour of the simple metal is anisotropic.

Bulk Beryllium Properties

Beryllium has many applications in the modern world. Because of its physical properties, such as low density (1.86 g/cm^3), high melting point (1278℃) and low thermal expansion coefficient, beryllium is used in the aerospace industries as light-weight structural materials. In addition, because of its low *Z* number (proton number), beryllium has a very low cross-section for X rays. Thus, beryllium is an ideal material to be used as the X-ray window. In this application, beryllium serves as a window between the vacuum and ambient air pressure allowing X-rays to penetrate. Scientifically, beryllium can be used as a test ground for many theories. The reason is mainly because beryllium is very easy to model because of its low atomic number. Density functional theory (DFT), *ab initio*, and first-principle calculations can model bulk beryllium very well. Beyond the simplicity of the beryllium, the beryllium surfaces have many unusual properties. These theoretical approaches are facing challenges and are going to be improved by studying simple materials, including beryllium.

The structure of beryllium is a hexagonal close-packed (hcp) structure, as shown in figure 1.4 [31]. The real space structure of beryllium is shown in figure 1.4 (c) with $t_1 = t_2 = 2.285\text{Å}$ and $t_3 = 3.582\text{Å}$; while (b) shows the first Brillouin zone (BZ). The small unit cell of the hcp structure of beryllium gives a relatively big BZ with $\Gamma - M = 1.59\text{Å}^{-1}$, $\Gamma - K = 1.84\text{Å}^{-1}$, and $\Gamma - A = 0.877\text{Å}^{-1}$. The 2D BZ of the (0001) and (10$\bar{1}$0) surfaces are displayed in figure 1.4 (a) and in figure 1.4 (d), respectively. Figure 1.5 shows the electronic band structure of bulk beryllium [3]. From the right panel of figure 1.5, it is obvious that there is a

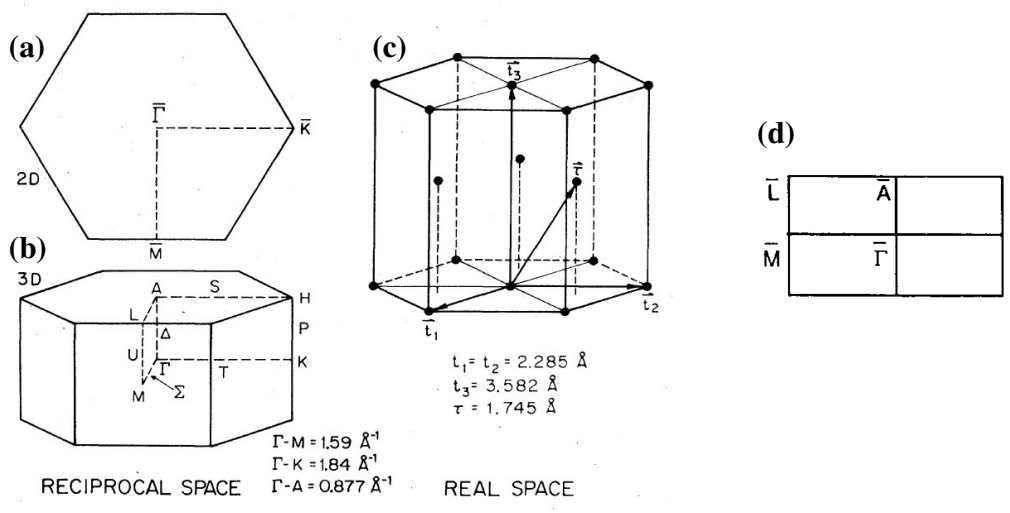

Figure 1.4. *(c) The real space structure of beryllium; (b) the corresponding reciprocal structure; and the 2D Brillouin Zone of (a) the (0001) surface and (d) the (10$\bar{1}$0) surface. (From Ref. [31]).*

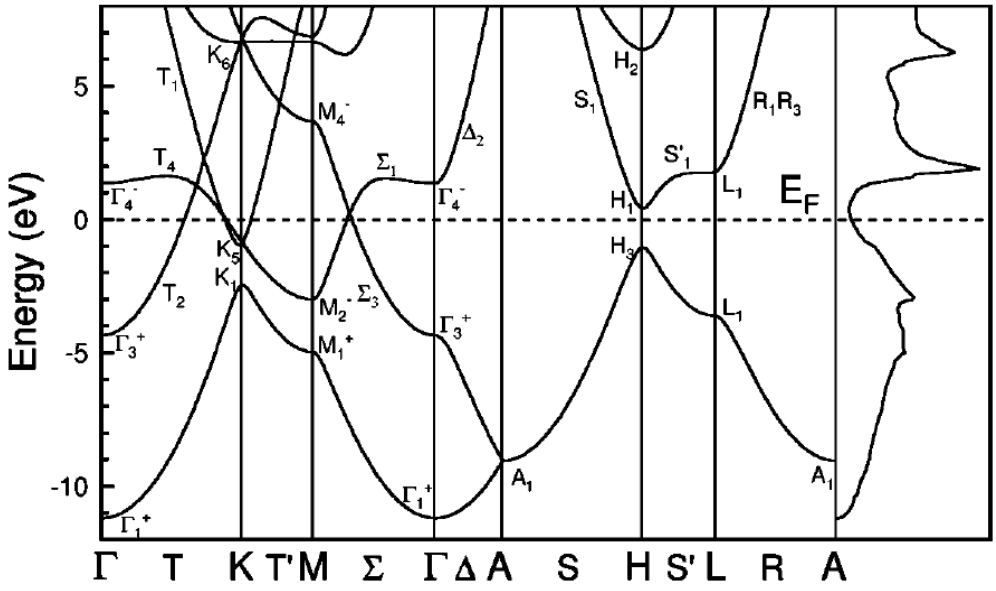

Figure 1.5. *The calculated electronic band structure of bulk beryllium. The right panel is the corresponding electron DOS. (From Ref. [3]).*

local minimum in the electron DOS at the Fermi energy. This results in beryllium being a marginal metal. Figure 1.6 shows the measured (dots) and the calculated (lines) phonon dispersion relation of bulk beryllium [2, 32]. The phonons of beryllium have a relatively high phonon energy compared with other materials. For example, silicon has an optical phonon energy around 65 meV; while beryllium has an optical phonon energy around 85 meV.

Beryllium is also found to have a superconducting phase with a critical temperature of 0.024 K. Electron-phonon coupling is responsible for the superconducting phase in beryllium, because beryllium is a BCS-type superconductor. Theoretically, a mass enhancement factor is used to describe the strength of the EPC. The definition of the mass enhancement factor, λ, is as follows [33, 34]:

$$\lambda = \frac{m_{eff}}{m_0} - 1 \tag{1-2}$$

where m_{eff} is the effective mass of the electrons with EPC renormalization; while m_0 is the effective mass of the electrons without EPC renormalization. The meaning of the mass enhancement factor is the fraction of the increased effective mass due to the EPC. For BCS-type superconductors, the critical temperature, T_c, is closely related to the mass enhancement factor, λ, by McMillan's equation:

$$T_c = \frac{\omega_{\log}}{1.2} \exp\left(\frac{-1.04(1+\lambda)}{\lambda - \mu^*(1+0.62\lambda)} \right) \tag{1-3}$$

where μ^* is the effective Coulomb interaction which is typically 0.1 [18]; $\omega_{\log}$ is the average phonon frequency, the definition will be described in next chapter. Figure 1.7 shows the superconducting critical temperature, T_c, of several BCS-type superconductors versus the mass enhancement factor, λ. From figure 1.7, it is obvious that T_c has a positive correlation

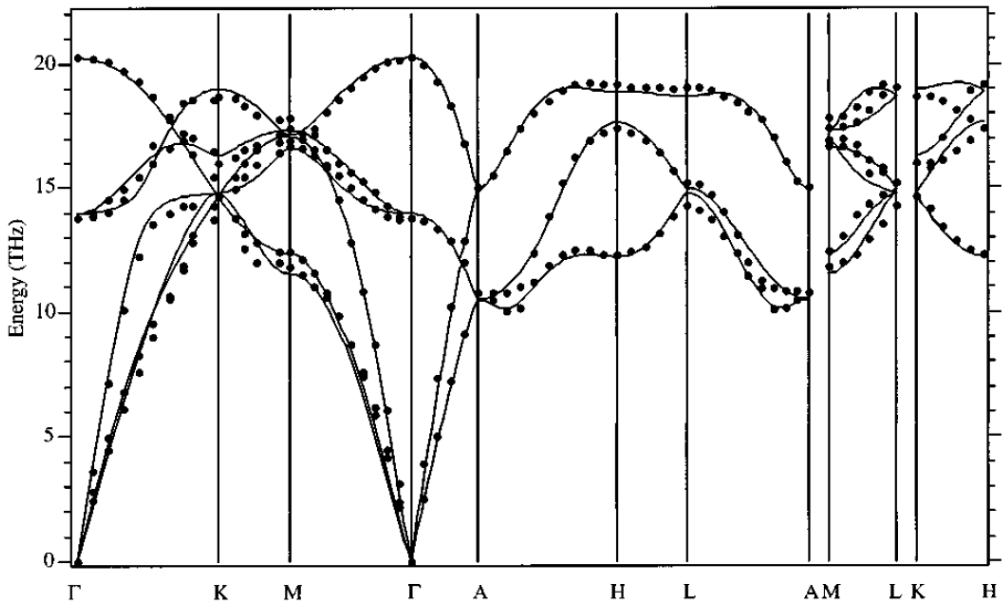

Figure 1.6. *The measured (dots) and the calculated (lines) phonon dispersion relation of bulk beryllium. (From Refs. [2, 32])*

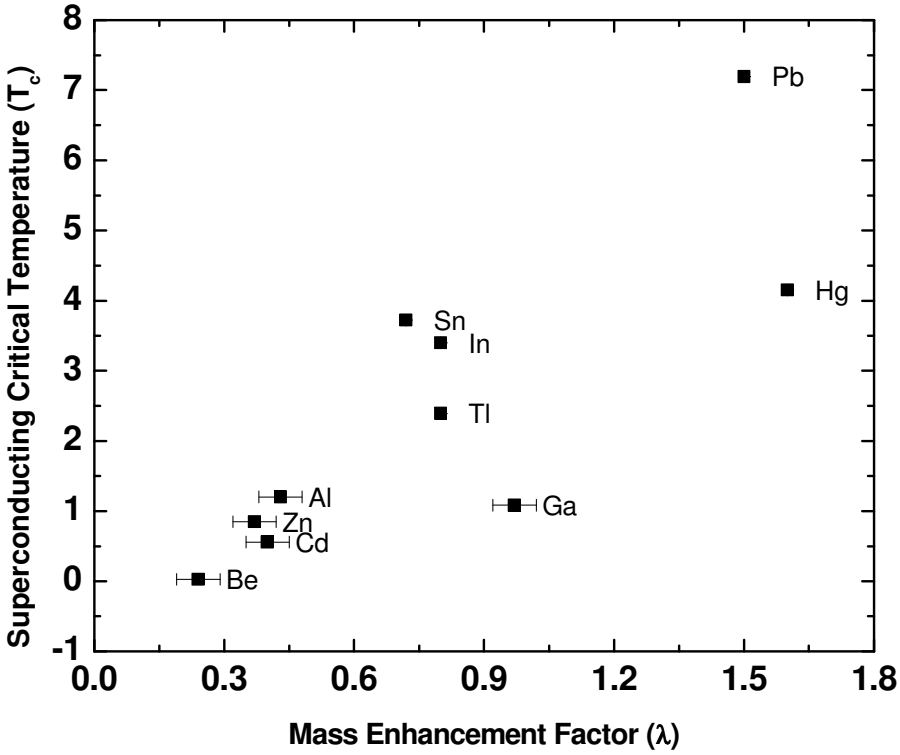

Figure 1.7. *The superconducting critical temperature, T_c, of several BCS-type superconductors versus the mass enhancement factor, λ. (From Ref. [33, 34]).*

with λ. For beryllium, the λ is low, only 0.24, and T_c is only 0.026 K [35]. In contrast, mercury (Hg) has λ equal to 1.6 and T_c equal to 4.153 K; while lead (Pb) has λ equal to 1.5 and T_c equal to 7.193 K. A more detailed description of the mass enhancement factor will be discussed in the next chapter.

N. E. Alekseevskii et al. reported the thickness-dependent critical temperature of amorphous beryllium [36]. The highest T_c reported is 8.6 K, which is much higher than the bulk value (0.026 K). This high critical temperature leads to a possible explanation that the surfaces of beryllium have very strong EPC.

Beryllium Surface Properties

There are many different surfaces of beryllium. The surface properties are very different from the bulk properties. Figure 1.8 shows the (0001) surface structure, which is not reconstructed. The inset indicates the location of the (0001) surface in a bulk structure. Because hcp has a stacking sequence of ABAB…, there are two possible terminations. In addition, for a single termination, there are two possible sets of lattice unit vectors, as shown in figure 1.8. From LEED-IV measurements [37], the interplanar distance shows a large expansion - $\Delta d_{12} = (+5.8 \pm 0.4)\% d_0$, where d_0 is the interplanar distance in the bulk. This is much larger when compared to that of close-packed fcc (111) surfaces. The extraordinary large expansion of the first layer should induce very interesting surface properties, such as soft phonon modes and two-dimensional electronic properties. Furthermore, the thermal expansion coefficient of the topmost layer is found to be extraordinary large— $\alpha_s = 70 \times 10^{-6} K^{-1}$ [38], which is 6 times the bulk value of $\alpha_b = 12 \times 10^{-6} K^{-1}$.

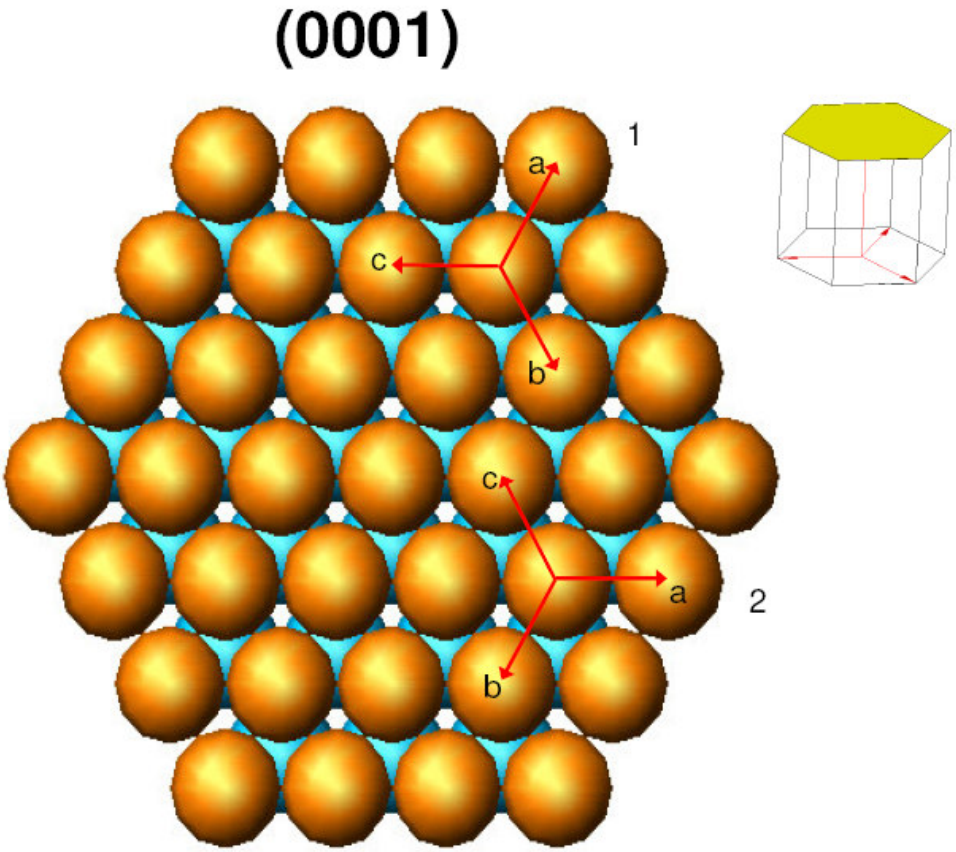

Figure 1.8. *Model of the (0001) surface structure. The inset indicates the location of the (0001) surface.*

Figure 1.9 shows the $(10\bar{1}0)$ surface structure of beryllium. There are two different terminations, indicated as "1" and "2." The inset indicates the location of the $(10\bar{1}0)$ surface in a bulk structure. This surface has an oscillating interplanar expansion/contraction [39]. The first and third interlayer spacings contract; while the second and fourth interlayer spacings expand. After studying the temperature-dependent interlay spacing, Ismail et al. extracted the thermal expansion coefficients for the topmost four layers as: $\alpha_{12} = -23.8(\pm 9.0)\times 10^{-5} K^{-1}$; $\alpha_{23} = +9.1(\pm 5.4)\times 10^{-5} K^{-1}$; $\alpha_{34} = -1.0(\pm 9.8)\times 10^{-5} K^{-1}$; and $\alpha_{45} = +10.2(\pm 7.2)\times 10^{-5} K^{-1}$ [39]; while the bulk value is $\alpha_b \approx 1.2\times 10^{-5} K^{-1}$. On the other hand, the Be$(11\bar{2}0)$ surface is reconstructed. Figure 1.10 shows the top view (top panel) and side view (bottom panel) of the (1×3) missing row structure of the Be$(11\bar{2}0)$ surface [40].

In addition to the surface structure, the surface dynamics are another interesting property of the Be surface. The measured surface phonon dispersion on the Be(0001) surface revealed a reduction in the magnitude of noncentral forces at the surface. Such a reduction is compatible with the electronic structure of the Be(0001) surface, which is more free-electron-like than that of bulk Be [32]. Figure 1.11 shows the surface phonon dispersion on (a) the Be(0001) surface and on (b) the Be$(10\bar{1}0)$ surface. The shadowed area is the projected bulk phonon. From figure 1.11 (a), the surface phonon dispersion has lower energy at $\bar{M}$ point than that at $\bar{K}$ point. Despites the inconsistent between the measured values (dots) and the theoretical values (line), the overall agreements are good. On the other hand, figure 1.11 (b) shows the surface phonon on Be$(10\bar{1}0)$ surface. On this surface, the phonons are not dispersing. The theoretical calculated values (line) disagree with the measured values (dots). Thus, it concludes that the bonding on Be$(10\bar{1}0)$ surface is more complicated than on Be(0001) where the qualitative

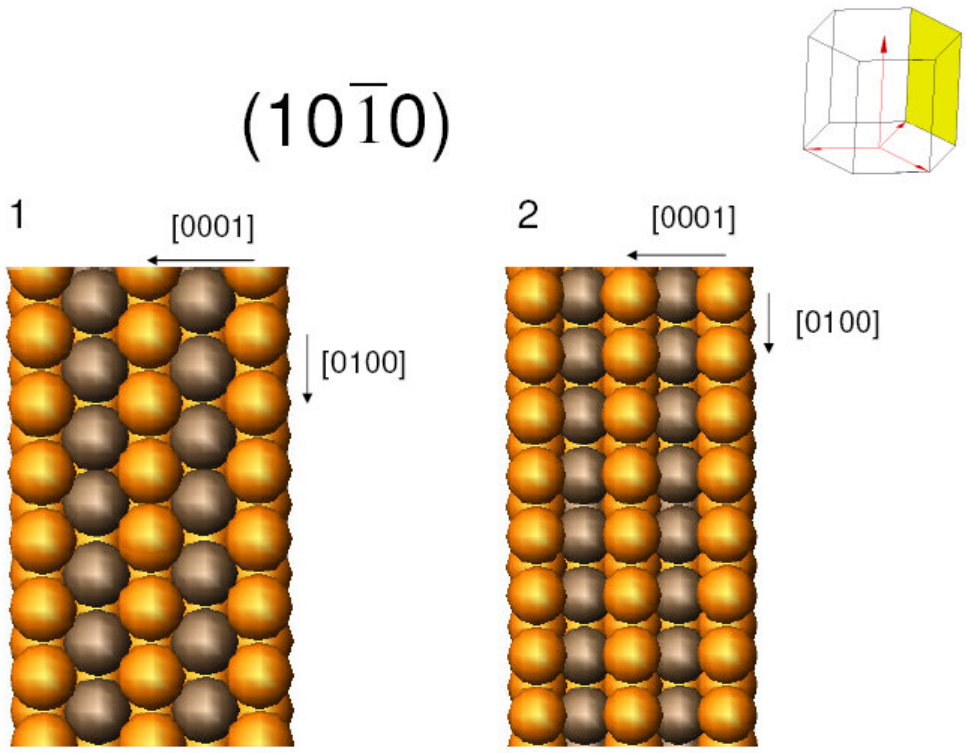

Figure 1.9. *Model of the (10$\bar{1}$0) surface structure of beryllium. There are two different terminations. The inset indicates the location of the (10$\bar{1}$0) surface.*

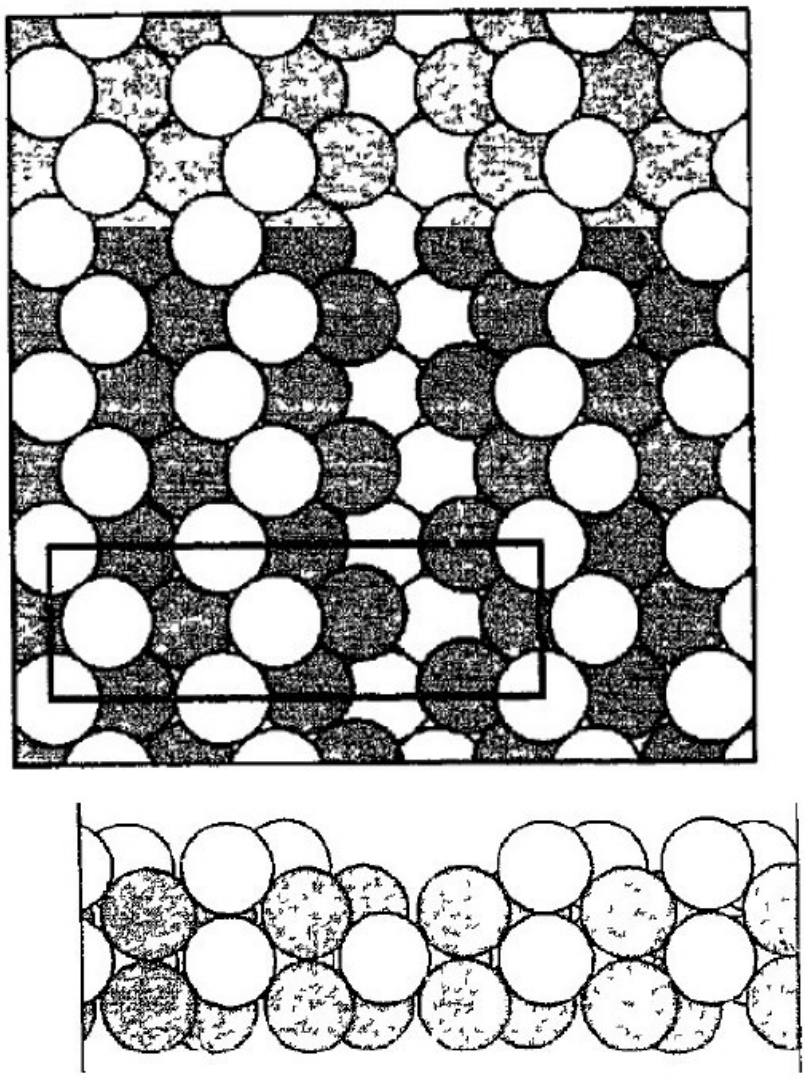

Figure 1.10. *The top view (top panel) and the side view (bottom panel) of the (1 × 3) missing row structure of the Be(11$\bar{2}$0) surface. (From Ref. [40]).*

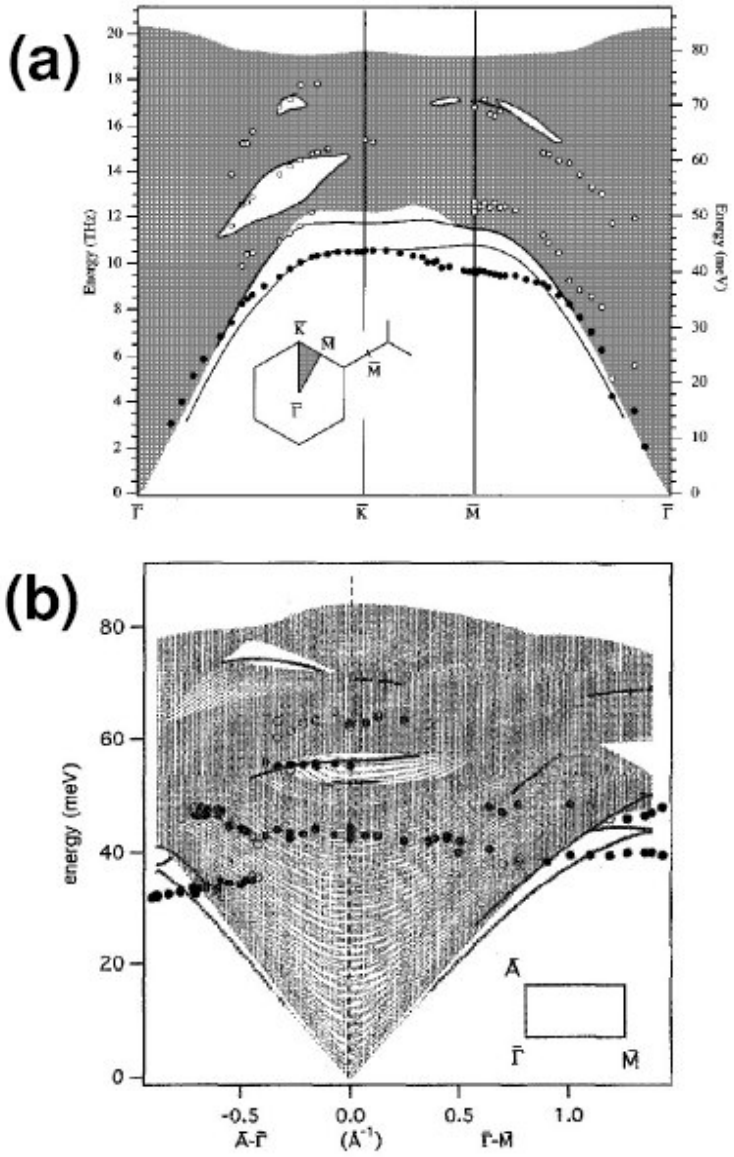

Figure 1.11. *The surface phonon dispersion on (a) the Be(0001) surface and on (b) the Be(10$\bar{1}$0) surface. The shadowed area is the projected bulk phonon. (From Refs. [32, 41])*

feature of the surface phonon dispersion can be described within a simple central force model [41].

Surface electronic states are the most intriguing part of the properties of the Be surfaces. Due to the large expansion/contraction of the surface interlayer distance, the surface electronic states are well separated from the bulk states. Figure 1.12 shows the Fermi surface of the (a) Be(0001) and (c) Be($10\bar{1}0$) surfaces and the electron energy-momentum dispersion relation along high symmetric lines in the surface BZ for (b) Be(0001) and (d) Be($10\bar{1}0$) surfaces [42, 43]. The shaded area is the projected bulk states. On the Be(0001) surface, there are three surface states with two of them crossing the Fermi energy. One is centered at the $\bar{\Gamma}$ point with a circular shape, with less than 1% deviation. The bottom of the band is about 2.78 eV binding energy; while the Fermi momentum of this state is about 0.947 $\AA^{-1}$. The other two surface states are centered at the $\bar{M}$ point with an eclipse shape. The major axis is along the $\bar{K}-\bar{M}-\bar{K}$ direction, while the minor axis is along the $\bar{\Gamma}-\bar{M}$ direction. For the Be($10\bar{1}0$) surface, the surface state centered at $\bar{A}$ has an eccentricity ε = 0.684, with a Fermi momentum of 0.450 $\AA^{-1}$ and 0.308 $\AA^{-1}$ along the $\bar{A}-\bar{L}$ and $\bar{A}-\bar{\Gamma}$ directions, respectively [22]. The bottom of the band is about 320 meV binding energy [42]. Among the different surfaces of beryllium, Be(0001) is the most intensely studied surface [14–18, 32, 43–52]; while the Be($10\bar{1}0$) surface is the second most studied [19–22, 39, 48, 53].

One of the interesting electronic properties of the beryllium surface is the giant Friedel oscillations [54, 55]. On the Be(0001) surface, P. T. Sprunger et al. used STM to observe the electron density wave [54]. They found that the amplitude of the charge density wave is extraordinary large and occurred near the defects on the surface. After using Fourier-transform STM, they found that the wavelength of the charge density wave

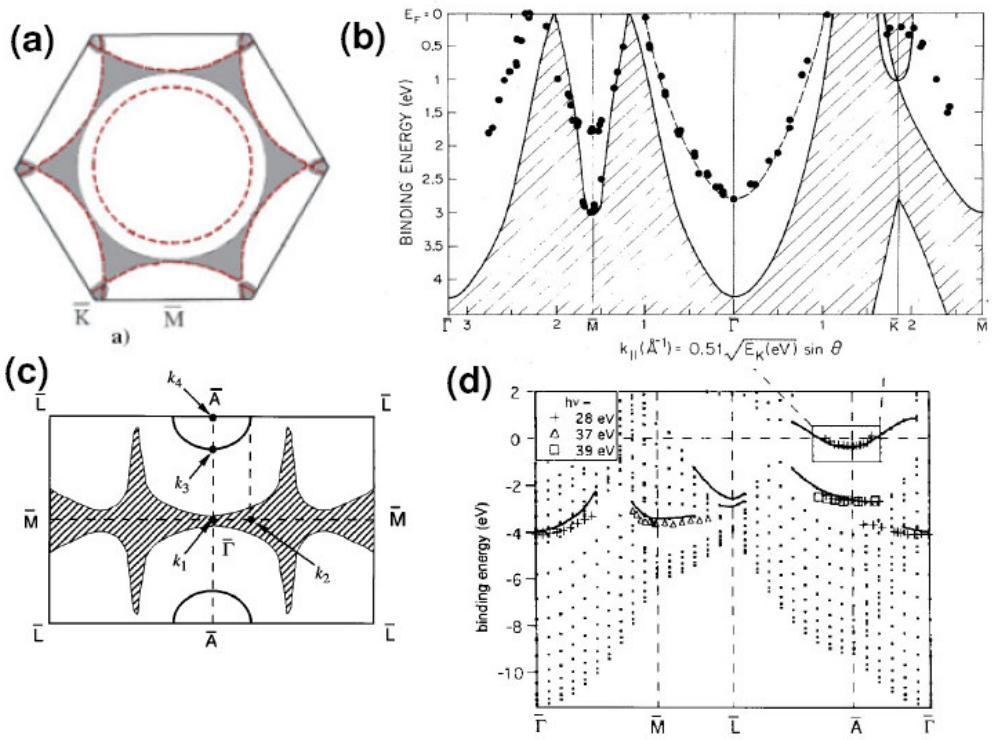

Figure 1.12. *The Fermi surface of the (a) Be(0001) and (c) Be(10$\bar{1}$0) surfaces and the electron energy-momentum dispersion relation along high symmetric lines in surface BZ for (b) Be(0001) and (d) Be(10$\bar{1}$0) surfaces. The shaded area is the projected bulk states. (From Refs. [42, 43]).*

has a $2k_F$ feature, which is shown to be the screening effect described by the Friedel oscillation mechanism. On the other hand, Ph. Hofmann et al. also found an anisotropic two-dimensional Friedel oscillation on the Be(10$\bar{1}$0) surface [55]. The anisotropic nature originated from the nature of the Fermi surface on Be(10$\bar{1}$0).

As mentioned above, some experiments measured the critical temperature of the amorphous beryllium to be about 8.6 K [36, 56, 57], which is more than 300 times larger than that of the bulk beryllium, 0.026 K [35]. One explanation is that the surface ratio of the amorphous beryllium is higher than that of the crystalline beryllium and the fact that the mass enhancement factors of the surfaces are larger. Indeed, the electron-phonon coupling on the surfaces is revealed to be very strong [14-22, 34, 44, 45]. On the Be(10$\bar{1}$0) surface, the mass enhancement factor is measured to be around 0.6 [19, 21–22], which is much larger than the value of the bulk – 0.24. For Be(0001), several papers reported the mass enhancement factor of the $\bar{\Gamma}$ surface state to be very large [14–18, 44, 45]. However, the values of the enhancement factors are inconsistent with each other. The values listed in Table 1.1 range from 0.59 to 1.18. It is worthy to mention that the values are extracted from different methods and that the data were taken from different positions in the reciprocal space, such as $\bar{K}$, $\bar{M}$, and $\bar{M} \leftrightarrow \bar{K}$. Hence, possible reasons for this inconsistency of the mass enhancement factors might be (1) the mass enhancement factors are dependent on the position in the reciprocal space, i.e., momentum-dependent; (2) there are inherent differences between the different methods used, and (3) sample quality plays a major role on the inconsistency.

Table 1.1. *The values of the mass enhancement factors obtained from both theory and experiment [14]. The reference numbers indicated in the table follow Ref. [14].*

λ	$\omega_{\log}(meV)$	k in SBZ	T	procedure	Reference
1.18		$\overline{M}$	12K	$d\,\mathrm{Re}\Sigma(\varepsilon)/d\varepsilon$	[6]
0.7 ± 0.1		$\overline{M} \leftrightarrow \overline{K}$	40K	Fitting $\mathrm{Re}\Sigma(\varepsilon)$ with Debye model	[7]
0.87		$\overline{K}$	0K	First principle calculations	[14]
0.70 ± 0.08	33.6	$\overline{M}$	0K	MEM extracted $\alpha^2F(\varepsilon)$	This work
0.59 ± 0.07	35.7	$\overline{M} \leftrightarrow \overline{K}$	0K	MEM extracted $\alpha^2F(\varepsilon)$ from [7]	This work
0.88	49.0	$\overline{K}$	0K	Calculated from $\alpha^2F(\varepsilon)$ of [14]	This work

Chapter II
Introduction to Electron-Phonon Coupling (EPC) and Angle-Resolved Photoemission Spectroscopy (ARPES)

Electron-Phonon Coupling

As mentioned in Chapter I, the electrons in many systems interact with other degrees of freedom. These interactions are not weak enough to be neglected. The interactions include electron-phonon, spin-charge, electron-electron, and electron-impurity interactions. Each of them is, now, at the center of condensed matter physics. For example, electron-phonon coupling (EPC) is the mechanism for the conventional superconductors, which can be well-described by BCS theory [1–3]. BCS theory reveals that conventional superconducting is closely related to the EPC. Electrons attract each other with the assistance of phonons and form Cooper pairs. In this process, one electron interacts with lattice ions when passing by the lattice. This causes the lattice to deform slightly due to the coulomb interaction between electrons and ions. Then, the deformed ion lattice creates a relatively positive environment around the area where the first electron just passed by. The second electron is then attracted by this positive area, resulting in the attractive force in the Cooper pair.

On the other hand, electron-electron interactions are also becoming very important. Now, materials with strong electron-electron interactions are referred to as strongly correlated materials. In these types of materials, the Fermi liquid or marginal Fermi liquid model are needed to describe their electronic properties. The electron-impurity interaction is also a very important issue, because the impurity has always appeared in real materials. Understanding the interactions between the electrons and

the impurities and controlling the impurities are now very important issues in commercial applications.

In BCS theory, electrons pair up by the assistance of the phonons and form Cooper pairs. To describe the electron-phonon interaction, one can utilize the Fröhlich Hamiltonian as follows [4]:

$$H = H_0 + H_{\text{int}} \tag{2-1}$$

where H_0 is the unperturbed Hamiltonian, related to the electron and phonon energies, and H_{int} is the interacting part of the Hamiltonian between electrons and phonons. H_0 and H_{int} can be written in the following form:

$$H_0 = \sum_{\vec{p}} \varepsilon_{\vec{p}} a_{\vec{p}}^{+} a_{\vec{p}} + \frac{1}{2} \sum_{\substack{\vec{q} \\ |\vec{q}|<q_m}} \omega_{\vec{q}} \left(b_{\vec{q}}^{+} b_{\vec{q}} + b_{-\vec{q}} b_{-\vec{q}}^{+} \right) \tag{2-2}$$

$$H_{\text{int}} = \sum_{\substack{\vec{p},\vec{q} \\ |\vec{q}|<q_m}} \upsilon(\vec{q}) a_{\vec{p}+\vec{q}}^{+} a_{\vec{p}} \left(b_{\vec{q}} + b_{-\vec{q}}^{+} \right) \tag{2-3}$$

where a and a^+ are the annihilation and creation operators of electrons, respectively; b and b^+ are the annihilation and creation operators of phonons, respectively; and ε, ω, and v are the energy of the electrons, the energy of the phonons, and the interacting potential between the electrons and phonons, respectively. $\vec{p}$ and $\vec{q}$ are the momentum of electrons and phonons, respectively. q_m is the maximum momentum the phonon can have. Figure 2.1 shows the Feynman diagram of the electron-phonon interaction for the interacting part of the Fröhlich Hamiltonian (Eq. (2-3)). In this process, the electron with momentum $\vec{p}$ adsorbs a phonon with momentum $\vec{q}$ or emits a phonon with momentum $-\vec{q}$ and then scatters to the final state with final momentum $\vec{p}+\vec{q}$. Using this Hamiltonian, one can deduce the transition probability from the initial state with N electrons in the system to the final state as the expression [5]:

$$\left\langle \alpha', \beta' \middle| H_{tot} \middle| \alpha, \beta \right\rangle = -\sum_{j} g\left(\vec{k}, \vec{k}'; s\right) \cdot e^{i\vec{q}\cdot\vec{R}_j^0} e^{i\left(\vec{k}-\vec{k}'\right)\cdot\vec{R}_j^0} \frac{1}{N} \left[n(q,s)\right]^{1/2} \tag{2-4}$$

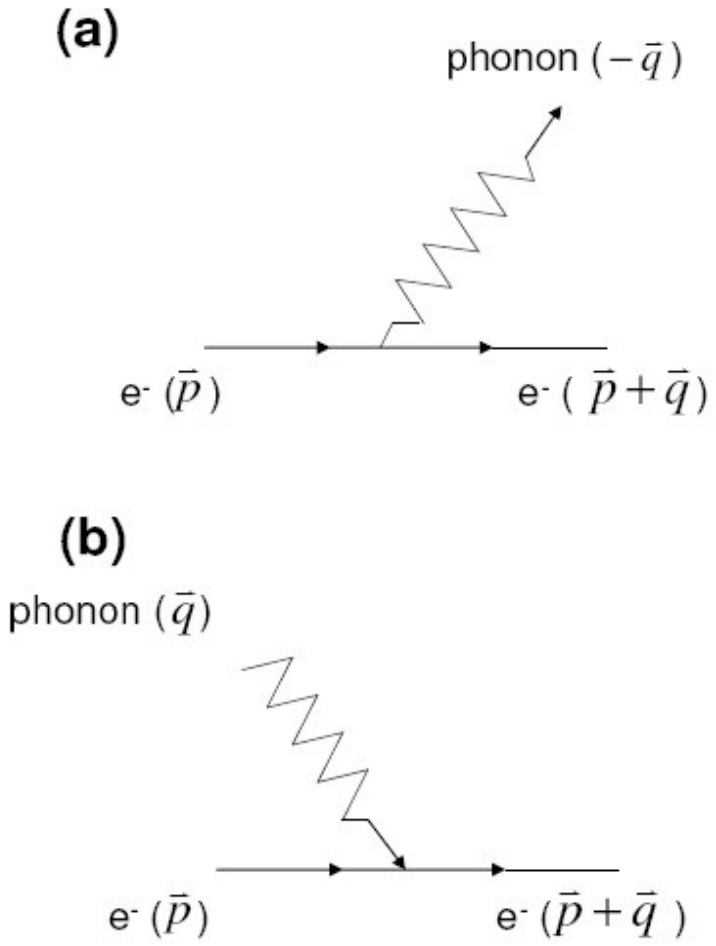

Figure 2.1. *Feynman diagram of the electron-phonon interaction for the Fröhlich Hamiltonian.*

where α and β denote the electron part and the phonon part of the eigenstates, respectively; s is the polarization of the phonon; $n(q,s)$ is the Bose-Einstein distribution function; and $g(\vec{k},\vec{k}';s)$ is defined as the coupling function, which refers to the scattering from the initial state at point $\vec{k}$ to the final state at point $\vec{k}'$ in reciprocal space. However, in many applications, it is more interesting to know the scattering rate from a state at $\vec{k}$ with energy E_k to all other final states with energy $E_k \pm \hbar\omega$, summing all possible states. The definition of the coupling function considering the scattering with respect to the energy, which is called the Eliashberg function, is shown as follows [5]:

$$\alpha^2 F(\omega,\vec{k}) = \frac{V}{\hbar(2\pi)^3}\sum_s \int_{S_F} \frac{d^2\vec{k}'}{v_{k'}} \left| g(\vec{k},\vec{k}';s) \right|^2 \delta(\hbar\omega - \hbar\omega(\vec{q},s)) \qquad (2\text{-}5)$$

This function gives the electron-phonon coupling between an initial state on the Fermi surface S_F and all other states $\vec{k}'$ on S_F which differ in energy from the initial state by $\hbar\omega$. Often, the average of Eq. (2-5) over all $\vec{k}$ on S_F is called the Eliashberg coupling function and defined as [5]:

$$\alpha^2 F(\omega) = \frac{\frac{V}{\hbar(2\pi)^3}\sum_s \int \frac{d^2\vec{k}}{v_{\vec{k}}} \int \frac{d^2\vec{k}'}{v_{\vec{k}'}} \left| g(\vec{k},\vec{k}';s) \right|^2 \delta(\hbar\omega - \hbar\omega(\vec{q},s))}{\int \frac{d^2\vec{k}}{v_{\vec{k}}}} \qquad (2\text{-}6)$$

Hence, with the Eliashberg coupling function, the first moment of this function can generate a McMillan-Hopfield parameter, η, as [5]:

$$\int_0^{\omega_{\max}} \alpha^2 F(\omega)\omega d\omega = \frac{\eta}{2M} \qquad (2\text{-}7)$$

and another very important moment is the mass enhancement factor, λ, as [5]:

$$2\int_0^{\omega_{\max}} \frac{\alpha^2 F(\omega)}{\omega} d\omega = \lambda \qquad (2\text{-}8)$$

where $\omega_{\max}$ is the maximum phonon frequency. Also, the average phonon frequency, $\omega_{\log}$, is defined as [6]:

$$\ln \omega_{\log} = \frac{2}{\lambda}\int_0^{\omega_{\max}} \frac{d\omega}{\omega}\alpha^2 F(\omega)\ln \omega \tag{2-9}$$

Theoretically, once you have the Eliashberg function, all quantities associated with the EPC can be deduced from it. For instance, the real and the imaginary parts of the self energy of the quasiparticles can be expressed as follows [5]:

$$\mathrm{Re}\,\Sigma(\omega;T) = -\int_{-\infty}^{\infty} d\nu \int_0^{\omega_{\max}} d\omega' \alpha^2 F(\omega') \frac{2\omega'}{\nu^2 - \omega'^2} f(\nu+\omega) \tag{2-10}$$

$$\mathrm{Im}\,\Sigma(\omega;T) = \pi\hbar\int_0^{\omega_{\max}} d\omega' \alpha^2 F(\omega')[1 - f(\omega-\omega') + 2n(\omega') + f(\omega+\omega')] \tag{2-11}$$

The real part of the self energy contains the information of the renormalized energy of the quasiparticle compared to the bare particle. The imaginary part of the self energy indicates the life time of the quasiparticle. Furthermore, the mass enhancement factor can also be related to the real part of the self energy by the following equation:

$$\lambda = \left.\frac{\partial\,\mathrm{Re}\,\Sigma(\omega)}{\partial\omega}\right|_{\omega=E_F,T=0} \tag{2-12}$$

To study the EPC, the two most important quantities need to be deduced. One is the coupling strength, which is characterized by the mass enhancement factor, λ. The other, even more important, quantity is the coupling function, which is described by the Eliashberg function, $\alpha^2 F(\omega)$. In general, the Eliashberg function can be considered as the phonon DOS, $F(\omega)$, multiplying the coupling constant, $\alpha^2(\omega)$. The Eliashberg function shows the details of the coupling between the electrons and phonons as a function of energy.

The question now is: how can these quantities be deduced from the experiment? To answer this question, one needs to know the signature of the EPC and then try to measure it. Figure 2.2 shows the

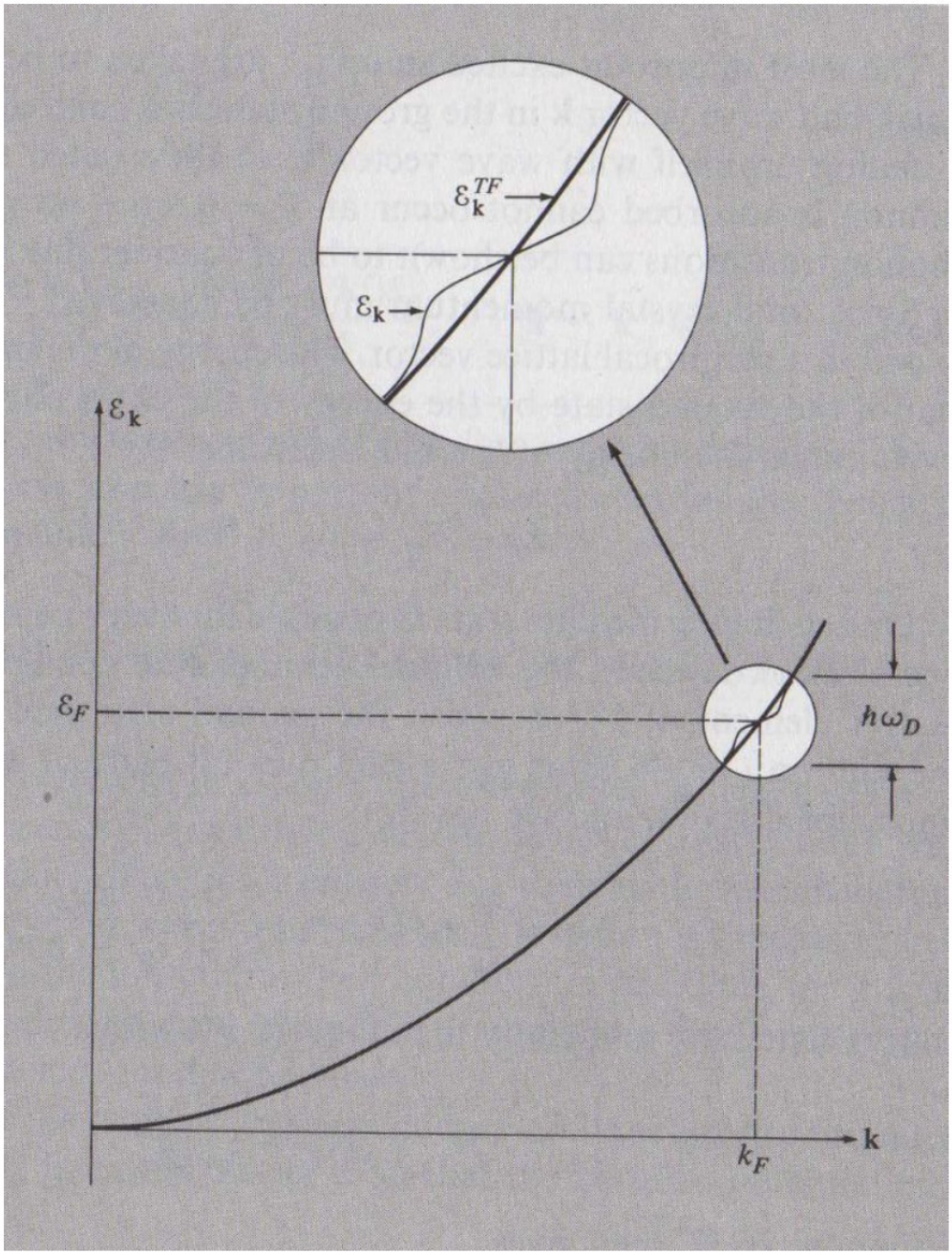

Figure 2.2. *Electron band structure of a free-electron-like system with a non-negligble EPC, which induces a slope kink near the Fermi energy. (From Ref. [7]).*

electron band structure of a free-electron-like system with a non-negligible EPC, which induces an abrupt slope change near the Fermi energy [7]. The energy renormalized region is within the phonon energy, which is the Debye frequency, ω_D, in this case. The abrupt slope change is denoted as the "kink" feature in the energy-momentum dispersion relation. From the ratio of the slope at the Fermi energy and the slope away from the kink, one can obtain the effective mass enhancement factor. Experimentally, ARPES can map out the Fermi contour and the electron band dispersion. Hence, using ARPES, it is possible to extract the kink information and the EPC strength. Next, we shall discuss the ARPES technique.

Angle-Resolved Photoemission Spectroscopy

Historically, the first experiments that revealed the interaction between light and electrons in solids were performed by Heinrich Hertz and Wilhelm Hallwachs in 1877 [8]. The experimental setup used by Hallwachs is shown in figure 2.3. Light was emitted from the light source, passed through the filter, and then was screened. Next, the light impinged on the charged gold-leaf electroscope with a grounded body. The conclusion of this experiment was that the negative charge can be removed by shining the ultraviolet light on the surface of the gold-leaf, while the positive charges cannot be removed. This phenomenon of the photoelectron remained a mystery until Einstein's explanation from the viewpoint of the quantization of the light-photon.

At the beginning of the 20th century in 1905, Einstein's famous work related to the photoelectric effect was published. His breakthrough idea was that the energy of the light is quantized, called a "photon," which won him the Nobel Prize. In his theory, the photon is a energy package with the minimum energy unit, ε, as follows:

$$\varepsilon = h\nu \tag{2-13}$$

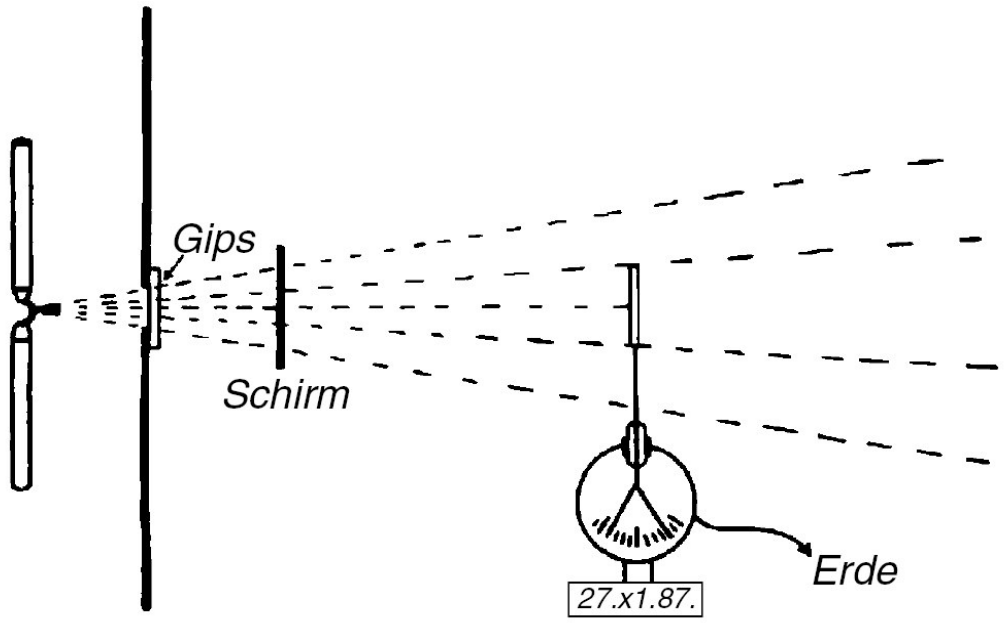

Figure 2.3. *The experimental setup used by Hallwachs. Light was emitted from the light source and then passed through a filter (Gips) and a screener (Schirm) to reach a charged gold-leaf electroscope with a ground body (Erde). (From Ref. [8]).*

where *h* is a constant, called the Plank constant, which is $6.626\times10^{-34} J\cdot s$ and ν is the frequency of the light. From this viewpoint, lights with different colors have different amounts of energy packages, because the frequency is different. The intensity of light on the surface indicates the amount of the energy packages—the photon, hitting on the surface per unit time per unit area. Another concept is that the electrons in metals can only either accept all the energy of the photon or reject it. This concept shows that even if you have a very intense red light (low frequency), you can never obtain the photocurrent for some metals with high work function, which is the barrier for electrons to over before escaping. This explained the photoelectric effect very well at that time.

Einstein's explanation of the photoelectric effect follows the equation of energy conservation:

$$E_k^{\max} = h\upsilon - \Phi_0 \tag{2-14}$$

where $E_k^{\max}$ is the maximum kinetic energy that electrons may have after escaping from the surface; *h* is the Plank constant; *v* is the frequency of the incident light; and Φ_0 is the work function of the metal. The work function describes the potential barrier that the electron at the Fermi energy needs to overcome before escaping from the surface. This quantity is a physical property of the solid surface, which is very sensitive to the condition of the surface. Hence, the change of the work function can be used to study the surface passivation. However, this equation only describes the electrons at the Fermi surface, because it only describes the maximum kinetic energy. In fact, the electrons can stay in the solid with a finite binding energy. Beyond the equation proposed by Einstein, the binding energy is defined as the difference between the Fermi energy and the energy of the state where the electrons stay. One can write the following equation according to the concept of the energy conservation again as follows:

$$E_k = h\nu - \Phi_0 - E_B \tag{2-15}$$

where E_B is the binding energy of the initial state of the emitted electron. This equation is adequate for describing the electrons in the core lever, because the core level has no momentum dependence. Figure 2.4 shows the schematic view of the photoemission process in the single-particle picture [8]. Electrons with binding energy E_B can be excited above the vacuum level E_{vac} by photons with energy $h\nu > E_B + \Phi_0$. Using an electron energy analyzer, one can obtain the photoelectron distribution as a function of energy, $I(E_k)$. This quantity is proportional to the electron DOS in the sample.

For valence bands, in addition to the information of the kinetic energy of the photo-emitted electron, one has to consider the energy-momentum relation, which is called a dispersion relation. To determine the momentum of the electron in the initial state, one needs the concept of momentum conservation. Because the electron only senses the potential barrier perpendicular to the surface, the momentum parallel to the surface will be conserved before and after the photoemission process; while the momentum perpendicular to the surface will be not conserved. According to parallel momentum conservation, the momentum of the initial state and final state and the momentum of the photon would relate to each other as:

$$\vec{k}_{f\parallel} = \vec{k}_{i\parallel} + \vec{k}_{photon\parallel} \tag{2-16}$$

where $\vec{k}_{f\parallel}$ and $\vec{k}_{i\parallel}$ are the final and initial parallel-momenta of the emitted electron, respectively, and $\vec{k}_{photon\parallel}$ is the photon parallel-momentum. However, the momentum of the photon is usually very small compared with the momenta of the electrons and can be neglected. Thus, when the final parallel-momentum is detected, the initial parallel-momentum can be obtained by this momentum conservation law. To measure the momentum of the emitted electron, the electron energy

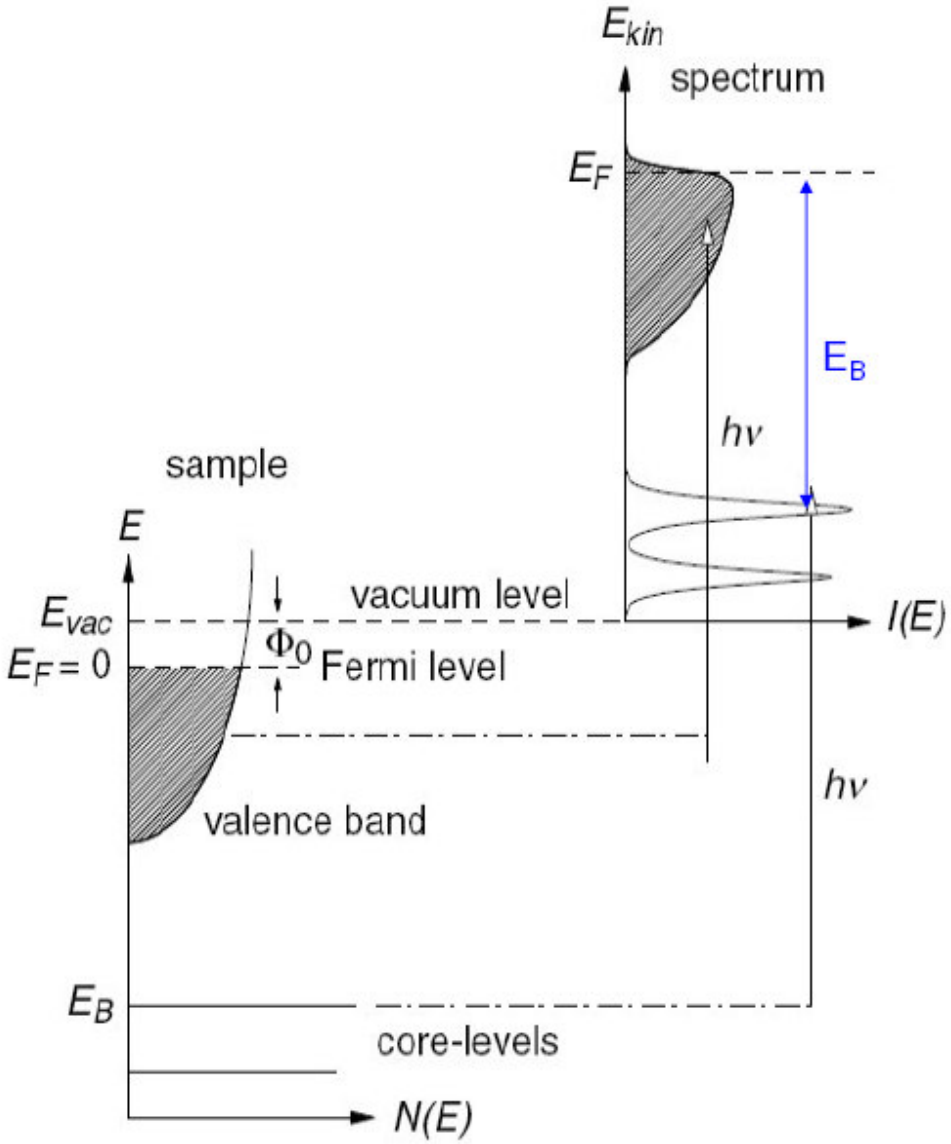

Figure 2.4. *Schematic view of the photoemission process in the single-particle picture. Electrons with binding energy, E_B, can be excited above the vacuum level E_{vac} by photons with energy $h\nu > E_B + \Phi_0$. (From Ref. [8]).*

analyzer should have the angle-resolved function, because the momentum is a vector parallel to the velocity of the electron.

Figure 2.5 shows a typical scheme of the ARPES experiment [9]. The electrons were emitted from the sample after irradiation of the light. The outgoing electron contains information on the emission angles, θ and φ, as well as the kinetic energy. All of this information can be detected by an electron energy analyzer. Thus, it is straightforward to deduce the parallel momentum of the electrons in the final state by

$$k_{\parallel}(i) = k_{\parallel}(f) = \frac{\sqrt{2mE_k(f)}}{\hbar}\sin(\vartheta) \qquad (2\text{-}17)$$

Hence, one can obtain information on the binding energy and the parallel component of the momentum of the electrons in the initial state in the solid. To scan any angle at any energy desired, one can obtain the quasiparticle dispersion or the constant energy mapping. Recently, the electron energy analyzer used for ARPES experiments has significant improvement. Figure 2.6 (b) shows the picture of the Scienta R4000, which is a electron energy analyzer, from VG Scienta. The instrument consists of a hemisphere, which serves as a electron energy selector, and a cylinder, which serves as a electron lens system. Figure 2.6 (a) shows the schematic diagram of the state-of-the-art electron energy analyzer. The electrons emitted out from the sample at different angles are collected through the aperture located at the sample-end of the analyzer. Then the lens system focuses and directs electrons at different angles to different final position, thus angle resolved. After entering the hemisphere, the voltage difference between the inner and outer hemisphere serves as the energy selector, thus energy resolved. Figure 2.6 (c) shows the raw data of the ARPES experiment. The energy and the angle are resolved simultaneously. Using typical ARPES data, the Be(0001) surface is shown in figure 2.7. Figure 2.7 (a) shows the Fermi surface mapping, which is obtained by setting the energy at the Fermi energy and scanning

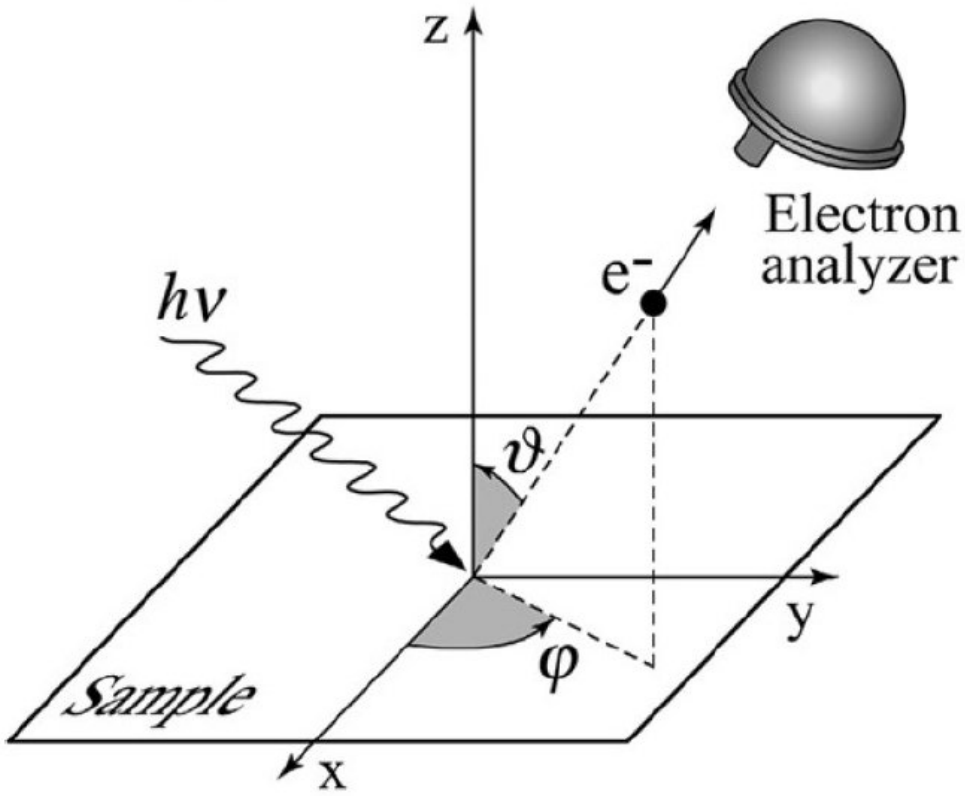

Figure 2.5. *Typical scheme of the ARPES experiment. The electrons were emitted from the sample after irradiation of the light. The outgoing electron has information on the emission angle and kinetic energy, which can be detected by an electron energy analyzer. (From Ref. [9]).*

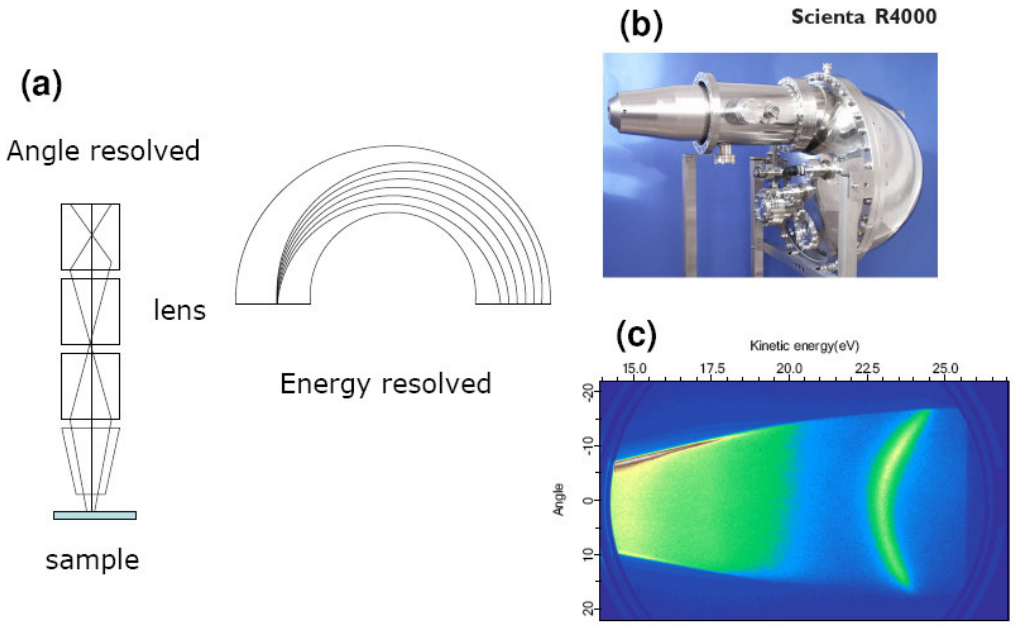

Figure 2.6. *(a) The schematic graph for the electron energy analyzer; and (b) the picture of the state-of-the-art instrument from VG-Scienta (Scienta R4000); (c) The raw data of the ARPES.*

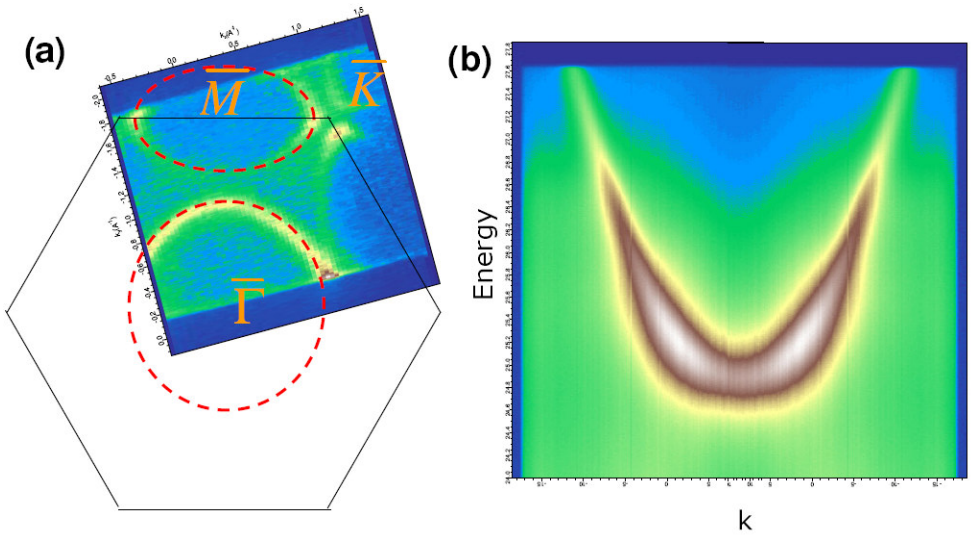

Figure 2.7. *Typical ARPES data. (a) Fermi surface mapping and (b) energy-momentum intensity mapping.*

all angles; while (b) shows the energy-momentum intensity mapping, which is obtained by setting a fixed momentum direction and scanning all the energies and momenta along that direction.

A few more important issues concerning ARPES need to be discussed here. The mean-free path of the electrons in the sample restricts the depth that can be detected using ARPES. Figure 2.8 shows the "universal" mean-free path for excited electrons in a solid as a function of the kinetic energy of the electrons [10]. For the typical ARPES experiment, the excited electrons have kinetic energies around a few tens eV, thus making the mean-free path of the excited electrons to be around the order of 1 nm. This very short mean-free path indicates that the ARPES experiment can only collect the electrons initially staying around a 1-nm surface, which makes ARPES a surface-sensitive tool.

In order to increase the detected intensity from the energy analyzer, one either has to (1) increase the data collection efficiency, (2) increase the photon source intensity, or (3) choose the right photon energy for high cross section. To solve the first issue, the choice of an energy analyzer is essential. A high-quality spherical energy analyzer is now available, allowing one to collect data with kinetic energy and angle information simultaneously. To solve the second and third issues, one has to use synchrotron radiation as the light source because, first, the synchrotron has a very intense light at a wide range of spectra. This will fulfill the requirement of the high-intensity light source. Second, the ability to choose the appropriate photon energy is an essential part of the ARPES experiment. For example, figure 2.9 shows a cross section of the Be(0001) $\overline{\Gamma}$ surface state as a function of photon energy. It is clear that the It is clear that the Be(0001) $\overline{\Gamma}$ surface state has high cross section at 16 eV and 30 eV; and has low cross section at 20 eV and above 40 eV. Remember that it is log scale in figure 2.9. If 45 eV is chosen for the photon energy, the measured intensity would be 10 times less than the

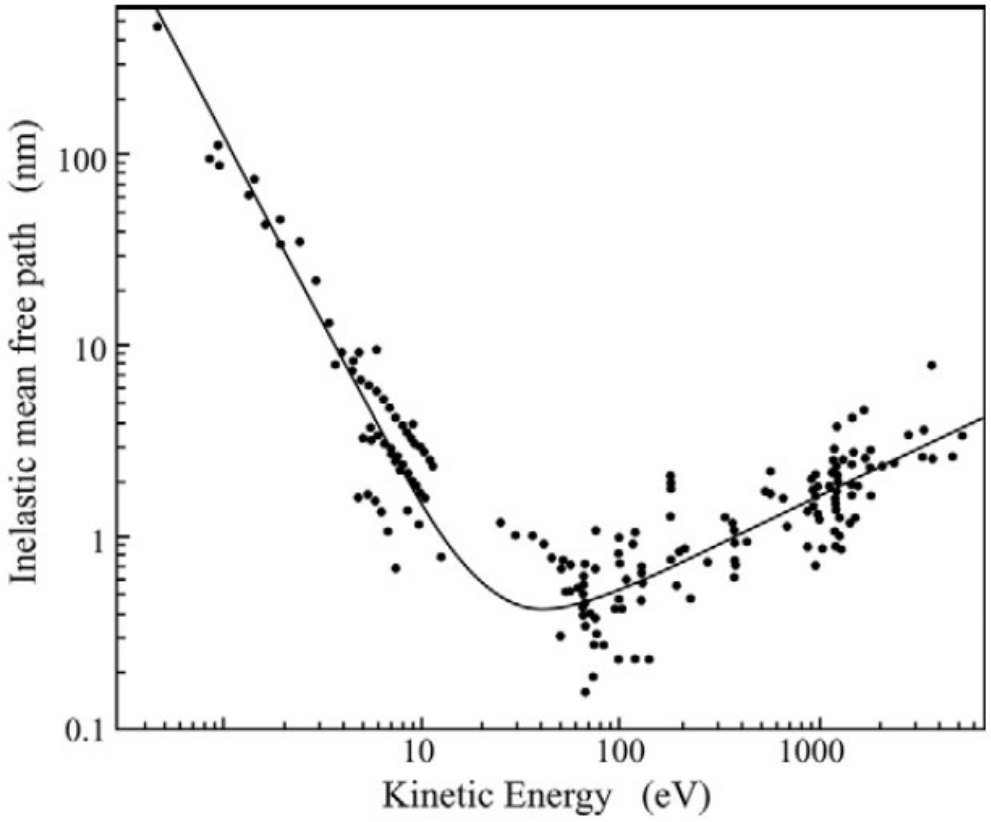

Figure 2.8. *"Universal" mean-free path for excited electrons in a solid as a function of the kinetic energy of the electrons. (From Ref. [10]).*

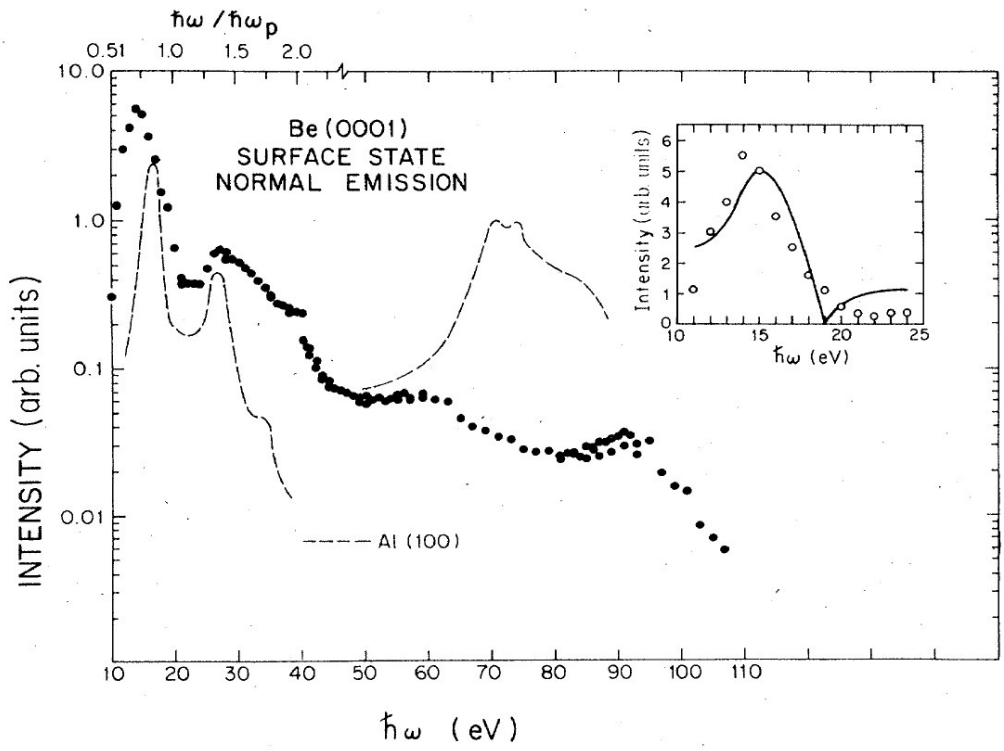

Figure 2.9. *Cross section of the Be(0001) $\overline{\Gamma}$ surface state, as a function of photon energy. (From Ref. [21]).*

case of 30 eV photon energy; and would be about 100 times less than the case of 16 eV photon energy.

In ARPES measurement, there are many different scanning modes [11], e.g., energy distribution curves (EDCs); and momentum distribution curves (MDCs). The EDC mode consists of setting the constant detecting angle and the photon energy and then scanning the energy that the analyzer detects; while the MDC mode consists of setting the constant detecting energy and photon energy and then scanning the detecting angle. One has to be careful that the linewith deduced from the EDC is not directly equal to the inverse lifetime of the quasiparticle. For the case of the 2D system, it can be correlated by the following correction equation [11]:

$$\mathrm{Im}\,\Sigma(\omega,T) = 2 \cdot FWHM\,(EDC) \cdot \left[1 - \frac{m v_{i\parallel} \sin^2 \theta}{\hbar k_{\parallel}} \right] \qquad (2\text{-}18)$$

The ARPES data are closely related to the electron self energy. To connect ARPES to the theory quantities, we shall first begin with the theory. Theoretically, the foundation is based on the Green's function formalism [9]. To describe the single electron in a many-body system, one can utilize the time-rdered one-electron Green's function $G(t-t')$, which describes the probability amplitude of adding or removing an electron to a many-body system. After completing the Fourier transformation, the Green's function can be expressed as $G(\vec{k},\omega) = G^{+}(\vec{k},\omega) + G^{-}(\vec{k},\omega)$, where $G^{+}(\vec{k},\omega)$ and $G^{-}(\vec{k},\omega)$ are the one-electron addition and removal Green's function, respectively. In order to take the electron-electron and electron-phonon interactions into account, the self-energy of the electrons needs to be included. The self-energy of the electrons contains all the information related to the interactions, which will cause the energy renormalization and the life time of the electron state. In the sense of the self-energy, the Green's function can be written as [9]:

$$G(\vec{k},\omega)=\frac{1}{\omega-\varepsilon_{\vec{k}}-\Sigma(\vec{k},\omega)} \tag{2-19}$$

where ω is the renormalized energy of the electron and $\varepsilon_{\vec{k}}$ is the bare electron energy. The self energy of the electrons can be written as $\Sigma(\vec{k},\omega)=\Sigma'(\vec{k},\omega)+i\Sigma''(\vec{k},\omega)$. The spectral function is related to the Green's function as $A(\vec{k},\omega)=-(1/\pi)\,\mathrm{Im}\,G(\vec{k},\omega)$ and can be expressed as:

$$A(\vec{k},\omega)=-\frac{1}{\pi}\frac{\Sigma''(\vec{k},\omega)}{\left[\omega-\varepsilon_{\vec{k}}-\Sigma'(\vec{k},\omega)\right]^2+\left[\Sigma''(\vec{k},\omega)\right]^2} \tag{2-20}$$

The ARPES data can be directly related to the spectral function, Eq. (2-20). Moreover, because ARPES can only detect the occupied states, the intensity of the ARPES data can be expressed as the spectral function times the Fermi distribution function:

$$I(\vec{k},\omega)=A(\vec{k},\omega)\cdot f(\omega-E_F) \tag{2-21}$$

As mentioned above, there are two most commonly used ways to analyze ARPES data. One is to plot the intensity as a function of the momentum with a constant energy. This will generate MDCs. The other way is to plot the intensity as a function of energy with a constant momentum. This will generate EDCs. The EDCs can be fit as a Lorentz function when the binding energy is far enough from the Fermi energy. According to Eq. (2-20) and Eq. (2-21), if the binding energy is too close to the Fermi energy, the spectrum will be asymmetric because of the effect of the Fermi distribution function, and then it is hard to fit with a Lorentz function. In addition, the self-energy is strongly dependent on the binding energy near Fermi energy. This makes using EDCs very difficult in doing quantitative analyses. The other way is to analyze the MDCs. For MDCs, the Fermi distribution function will not affect the line shape, because the Fermi distribution function has the same effect on every momentum at the same binding energy. With the assumption of the linear bare dispersion, the MDCs can be considered as a Lorentz function. Also, for MDCs, the

momentum range is small enough to assume that the self-energy is independent of the momentum. Then, the width of the MDCs represents the imaginary part of the self energy as:

$$FWHM\,(MDCs) = \frac{2\left|\mathrm{Im}\,\Sigma(\omega)\right|}{v} \tag{2-22}$$

where v is the local velocity, defined as $v = \partial\varepsilon_0/\partial k$. Thus, the imaginary part of the self energy can be obtained from the width of the MDCs. In addition, from Eq. (2-20), it is clear that the peak position is determined by $\omega = \varepsilon_{\vec{k}} + \Sigma'(\vec{k},\omega)$. The real part of the self energy is the different between the measured dispersion, $\omega(\vec{k})$, and the bare dispersion, $\varepsilon(\vec{k})$. Thus, from an analysis of the MDCs, the real part and the imaginary part of the self-energy can be obtained. Hence, the self-energy can be fully obtained from the experiment. Figure 2.10 shows the relationship between the ARPES data and the self-energies, including the real and the imaginary parts. The real part of the self-energy, $\mathrm{Re}\,\Sigma$, is defined as the energy difference between the renormalized energy and the bare energy, as indicated in figure 2.10 (b). The imaginary part of the self-energy is related to the FWHM (full width of half maximum) of the spectrum, as shown in figure 2.10 (a).

To extract the mass enhancement factor (coupling strength) and the Eliashberg function (coupling details), self-energy information is the key. In the literature, there are three methods used to extract the mass enhancement factors; one of them can even extract the Eliashberg function: (1) the slope method [12–14] which is based on the relation between the mass enhancement factor and the real part of the self energy, Eq. (2-12). One can extract the mass enhancement factor from the slope of the real part of the self-energy near the Fermi energy; (2) the phonon model method [15–18] which uses the assumption for the Eliashberg function. One can use the Einstein model, the 2D Debye model, or the 3D

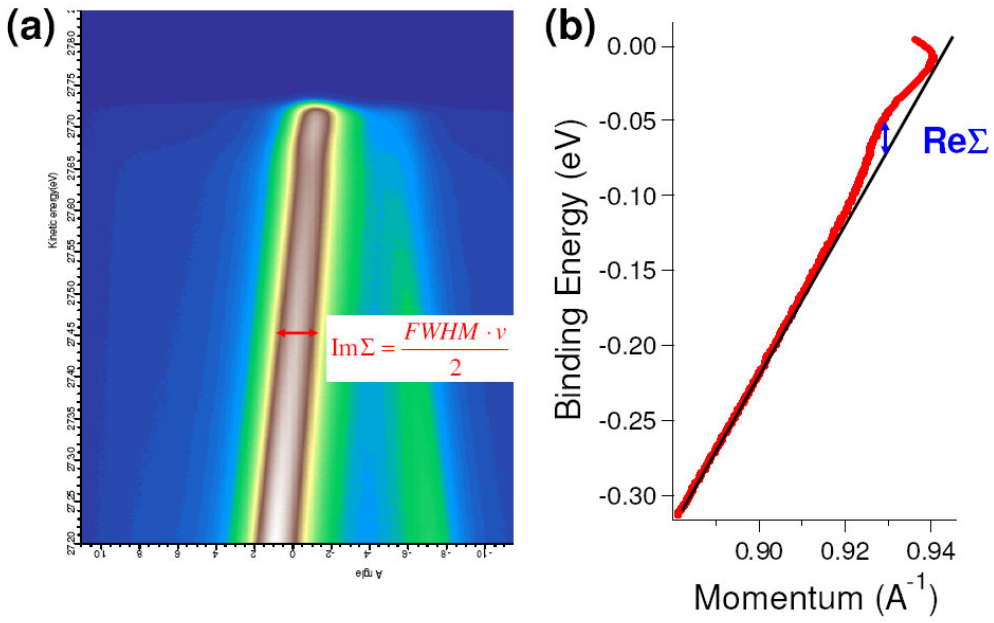

Figure 2.10. *Relationship between the ARPES data and the self energies, including the real and the imaginary parts.*

Debye model to approximate the Eliashberg function. Then, using Eq. (2-10) and Eq. (2-11), it is possible to fit the experimental real or imaginary parts of the self-energies as a function of binding energy or temperature with λ as a fitting parameter; and (3) the maximum entropy method (MEM) [6, 19, 20] where after the real part of the self-energy is obtained from the experiment, one can use Eq. (2-10) to do the integral inversion to extract the Eliashberg function. Because the integral inversion is very sensitive to the noise presented in the data, J. Shi *et al.* proposed using a constraint for the integral inversion. Using this method, one can extract the Eliashberg function and then calculate the mass enhancement factor from the extracted Eliashberg function from Eq. (2-8).

There are intrinsic advantages and disadvantages for these methods. For the slope method, the definition of Eq. (2-12) is the slope of the real part of the self-energy at zero energy (Fermi energy) and zero temperature. Basically, zero temperature is impractical. Further, as the temperature increases, the slope of the real part of the self-energy would change, thus giving different values of the mass enhancement factor. For the phonon model method, a problem arises from the approximation of the phonon model itself. Because the Eliashberg function is a very complex function, simple models, such as the Debye or Einstein models, cannot match the details of the Eliashberg function. For example, the 2D Debye model approximates the Eliashberg function as $\alpha^2 F(\omega') = \lambda(\omega'/2\omega_D)$; while the 3D Debye model uses $\alpha^2 F(\omega') = \lambda(\omega'/\omega_D)^2$ and the Einstein model uses $\alpha^2 F(\omega') = (\lambda\omega_E/2)\delta(\omega - \omega_E)$. Figure 2.11 shows the theoretical Eliashberg function and 2D, 3D Debye and Einstein models for comparison. The complexity of the Eliashberg function is obvious and that these simple models can not approximate it well. This will always give an uncertainty of the results. For MEM, the ability of the method to extract coupling strength and function is very powerful. The only problem that

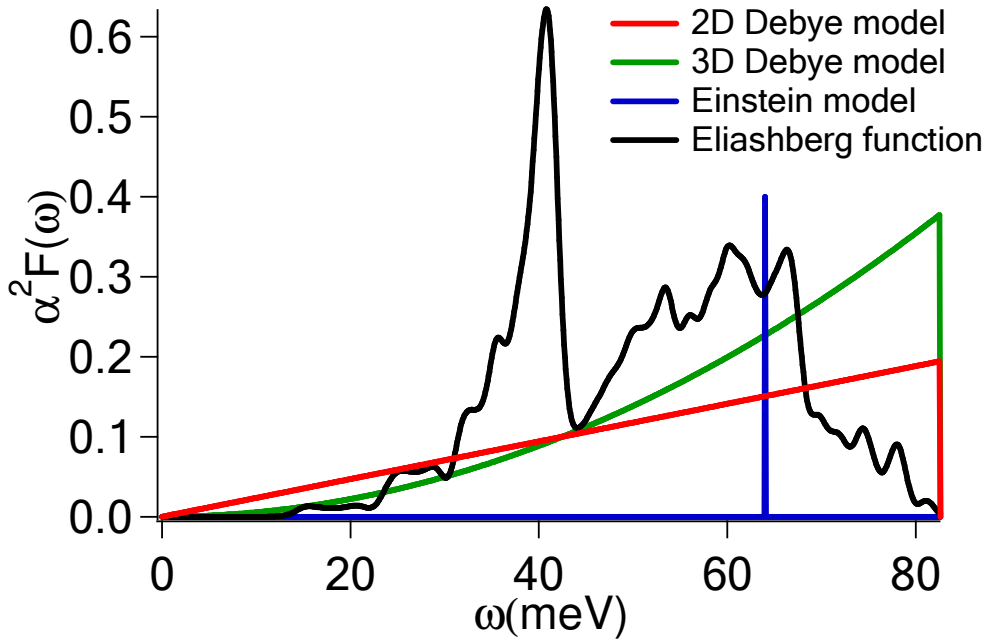

Figure 2.11. *Comparison between Eliashberg function and 2D, 3D Debye and Einstein models.*

might occur is the need for good quality data. For reliable results from MEM, the resolution of the instruments and the noise in the data are the main issues to be solved. More details will be discussed in Chapter III.

Chapter III
Quantitative Extraction of the Mass Enhancement Factor and Eliashberg Function

Introduction

Angle-resolved photoemission spectroscopy (ARPES) was developed for band mapping and then was used for studying the electronic properties of materials. Improvements in energy and momentum resolutions have been crucially important for measuring many-body interactions in complex materials. In such complex materials, one of the most basic questions has not yet been answered: what kinds of bosons are responsible for the large electron-boson coupling (EBC) in high T_c superconductors? In order to know this question, an understanding of the details of the ARPES technique is very important. Unfortunately, despite the extensive use of this technique, understanding the ARPES data is still limited. One approach for understanding the ARPES experimental technique is to test it on systems with large electron phonon coupling (EPC) as the only source of the many-body interactions. The beryllium surface [1–7] serves as an ideal system for testing the analysis of ARPES. EPC on the beryllium surface is large and is the only boson in this system.

The signature of EBC on the ARPES experiments is the “kink” feature near the Fermi energy. EBC renormalizes the bare particle with binding energy within the energy of the boson. This exhibits in the energy-momentum dispersion of the particle. For example, the bottom panel of figure 3.1 shows a general picture of the electron dispersion relation of a free-electron-like material. When zooming in to the dispersion near the Fermi energy (inset), the system with EBC will have a dramatic slope

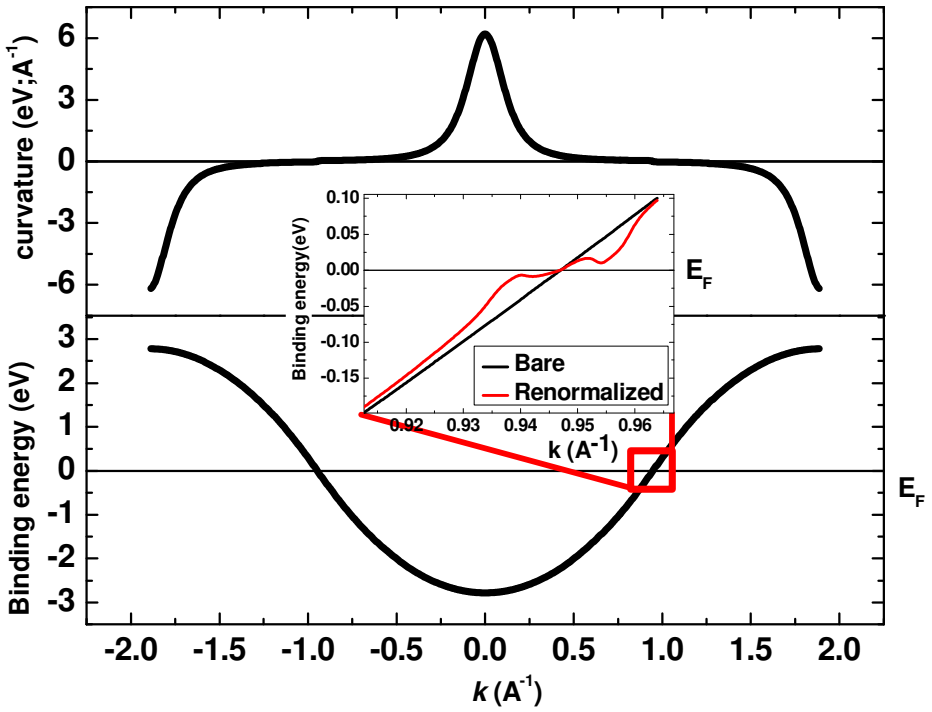

Figure 3.1. *The free-electron-like electron band structure (bottom panel) and the corresponding curvature (top panel). The inset is the zoom-in view of the dispersion near the Fermi energy. The red lines indicate the renormalized dispersion due to EPC.*

change (referred to as the “kink”) near the Fermi energy, as indicated by the red curve. It is well-understood that the kink energy is closely correlated to the energy of the coupled bosons. This close correlation between the energy of the kink and the energy of the bosons is the key to understanding the complex EBC. In other words, a quantitative analysis of the band dispersion is the key to understanding the many-body effects. Here, we present the inherent limitations in the analyses and experimental limitations for extracting the many-body information from ARPES. These limitations come from (1) the energy and momentum resolutions due to the photon source and the electron energy analyzer; (2) the assumption of the bare dispersion, which cannot be measured in the many-body system; and (3) the appearance of noise in the data.

The influences of the energy and momentum resolutions smear the raw data [8]. The smearing may make the fine structures in the kinks invisible and difficult to determine the Fermi momentum, $\vec{k}_F$, or even distort the shape and the area of the Fermi surface [9]. To accurately analyze the ARPES data, an understanding of the effects from the resolution is needed. In the literature, the effects from the energy and momentum resolutions based on the Fermi liquid and marginal Fermi liquid models were discussed by A. Kaminski *et al.* [10]. There is no further discussion about the influence of extracting many-body interaction information from the ARPES data, though it was briefly discussed in the comment [11] and reply [12] related to the paper published by X. J. Zhou *et al.* [13], in which they used the maximum entropy method (MEM), developed by J. Shi *et al.* [1], to extract the Eliashberg function (ELF), the EBC function, from the ARPES raw data. The MEM will be introduced in details in Chapter V. In this chapter, the effects of the energy and momentum resolutions on extracting the dispersion relation, ELF, as well as the mass enhancement factor were studied.

To study the kink feature, an accurate determination of the dispersion is crucial. As mentioned by T. Valla *et al.* [14], the MDCs are more suitable for analyses of the peak positions and widths than the EDCs. By adopting a linear approximation (LA) to the bare dispersion, the MDCs can be approximated as a Lorentz function [14, 15]. For the case where the bare dispersion has a large curvature, the shape of the MDC would be far from the Lorentz function form. This will reduce the ability for an accurate determination of the peak position and width. Furthermore, the relation between the MDC width and the imaginary part of the self energy would be more complicated than the simple relation, which was mentioned in Chapter II (Eq. (2-22)), $\mathrm{Im}\Sigma(\omega,T) = FWHM(\omega,T)\cdot v/2$ [15], that is based on the LA. Though the LA was mentioned in the literature [14, 15], a careful study of this approximation remains untouched. Because the LA approximates bare dispersion with a curved form to a linear form, validity of the LA is limited by the curvature [16] of the bare dispersion. In this work, the limitation of the curvature of the bare dispersion is given.

Noise is always a tricky part of the data analysis for subtle features. For example, as was mentioned in Ref. [1], the integral inversion is very sensitive to the quality of the raw data. This is the reason why the MEM was used to overcome the mathematically unstable problem due to the noise. Unfortunately, the influence of the noise on the fine structure determination has not been investigated in detail. Here, we present how the noise will affect the robustness of the fine structure analysis.

Modeling

A. Formula

To understand all the issues mentioned above, one has to start from the theoretical description of the photoemission process. In the theoretical point of view, the Born-Oppenheimer (BO) approximation was

adopted, in which the photoelectric process is assumed to be adiabatic. The photo-electron emitted from the surface creates a hole state in the remaining system. This state is described by the single-particle spectral function, $A(\omega,\vec{k},T)$, under the BO approximation [17].

$$A(\omega,\vec{k},T)=\frac{\pi^{-1}\left|\mathrm{Im}\,\Sigma(\omega,\vec{k},T)\right|}{\left[\hbar\omega-\varepsilon^{0}(\vec{k})-\mathrm{Re}\,\Sigma(\omega,\vec{k},T)\right]^{2}+\left|\mathrm{Im}\,\Sigma(\omega,\vec{k},T)\right|^{2}} \qquad (3\text{-}1)$$

where $\mathrm{Re}\,\Sigma(\omega,\vec{k},T)$ and $\mathrm{Im}\,\Sigma(\omega,\vec{k},T)$ are the real and the imaginary parts of the self-energies, Σ, of the quasiparticles, respectively, and $\varepsilon^{0}(\vec{k})$ is the bare dispersion relation. From the spectral function, it is natural to see why the MDCs and EDCs are the most commonly used for analyzing ARPES data. For studying many-body interactions, which are near the Fermi energy, MDCs are a more suitable mode than an EDCs mode is [14, 15]. Since EDCs is the data with a constant emission angle, not a constant momentum, the trace of EDCs in energy-momentum space is not at the same $\vec{k}$ value [18]. Moreover, when the peak in the EDCs is close to the Fermi energy, the peak profile will also be severely affected by the Fermi distribution function. Another physical reason for the complexity of EDCs comes from the strong energy dependence of the self-energy near the Fermi energy. In contrast, the MDCs can be much simpler for quantitative analyses near the Fermi energy. First, the $\vec{k}$ range of the kink near the Fermi energy is small; therefore, the self-energies, both $\mathrm{Re}\,\Sigma(\omega,\vec{k},T)$ and $\mathrm{Im}\,\Sigma(\omega,\vec{k},T)$, can be considered as $\vec{k}$ -independent and can be written as $\mathrm{Re}\,\Sigma(\omega,T)$ and $\mathrm{Im}\,\Sigma(\omega,T)$, respectively [18]. Second, for each MDC located at a certain binding energy, the influence from the Fermi distribution function is the same on every $\vec{k}$ point within each MDC. Hereafter, we focus our analysis on the MDC only and compare it with the EDC when necessary.

The only concern about MDCs is the assumption of the bare dispersion relation. Experimentally, the bare dispersion, $\varepsilon^0(\vec{k})$, cannot be measured in a many-body system in which electrons are coupled to the boson modes or strongly correlated to the electrons themselves. The dispersion relation near the Fermi energy will have a kink feature, as shown in the bottom panel of figure 3.1. An assumption for the bare dispersion is needed for further analysis. One approach is to use the bare dispersion from *ab-initio* calculations for the system studied. But for some systems, the calculated bare dispersion is questionable. Another more frequently used approach is to assume the bare dispersion as a linear function within a small energy range. If the bare dispersion is approximated as a linear function (LA), $\varepsilon^0(\vec{k}) = A(\vec{k} - \vec{k}_F)$, near the Fermi energy ($\vec{k}_F$ represents the Fermi momentum), the MDCs can be seen as a simple, symmetric Lorentz function, which can be derived from Eq. (3-1). This is the basic assumption for analyses of the MDCs in the ARPES data.

The main information obtained from the MDCs is the peak positions and peak width. The peak position gives the dispersion relation; the peak width gives the lifetime of the quasiparticles. The peak position is obtained from fitting a Lorentz function to the MDCs. If you consider the original form of the bare dispersion, the MDCs are asymmetric peaks. It is important to understand how the curvature of the bare dispersion affects the peak positions. For determining the width, it is even more complicated. In addition to the Lorentz fitting argument mentioned above, one needs to convert the width of the MDCs to the $\mathrm{Im}\Sigma(\omega,T)$ from an assumption of the bare dispersion again. In the literature, the LA and quadratic approximation were used for converting this equation, which will be discussed in detail later. Validity of the $\mathrm{Im}\Sigma(\omega,T)$ determined from the MDCs needs more careful study. The free-electron-like Be(0001) surface state is an ideal system for studying this problem, because the curvature

can vary from very small to very large by going from the Fermi energy to a higher binding energy. Also, the $\mathrm{Im}\Sigma(\omega,T)$ at the higher binding energy can be determined accurately from the EDCs, which can be used for comparison as a check.

To test the validity of LA and the effects of the noise and energy and momentum resolutions, the model data were produced by multiplication of the spectral function, the Fermi distribution function, and then convoluted with a Gaussian function to simulate the energy resolution and with a window function to simulate the momentum resolution [10]. The window function was described by the upper and lower limit of the integration in momentum space. This model function can be written as the following:

$$I(\omega,\vec{k},T,\Delta E,\Delta k)=\int_{k-\frac{\Delta k}{2}}^{k+\frac{\Delta k}{2}}\int_{-\infty}^{\infty}A(\omega',\vec{k}',T)f(\omega',T)Gaussian(\omega,\omega',\Delta E)d\omega'\,d\vec{k}' \quad (3\text{-}2)$$

where $f(\omega,T)$ is the Fermi distribution function; $Gaussian(\omega,\omega',\Delta E)$ is the Gaussian convolution function; and $A(\omega',\vec{k}',T)$ is the spectral function, as shown in Eq. (3-1). Figure 3.2 shows the flow chart of the procedure for doing the simulations to study the effects from the linear approximation, the instrument resolutions, and the noise. First, we put in the predefined ELFs. Then, the self-energies can be obtained by assuming a certain temperature. With the predefined bare dispersions, one can construct the spectral function, $A(\omega,\vec{k},T)$. The energy and momentum resolutions are simulated by convolution of the spectral function with Gaussian and window functions, respectively. After the noise-free data were generated, the noise is added in to generate the noisy data. Until this step, we defined the procedure as the “model data generation” procedure. Once the model data are generated, the next step is to analyze the data using the Data Analysis Procedure. In this procedure, it follows the regular procedure used to analyze experimental data—(1) MDC fitting; (2)

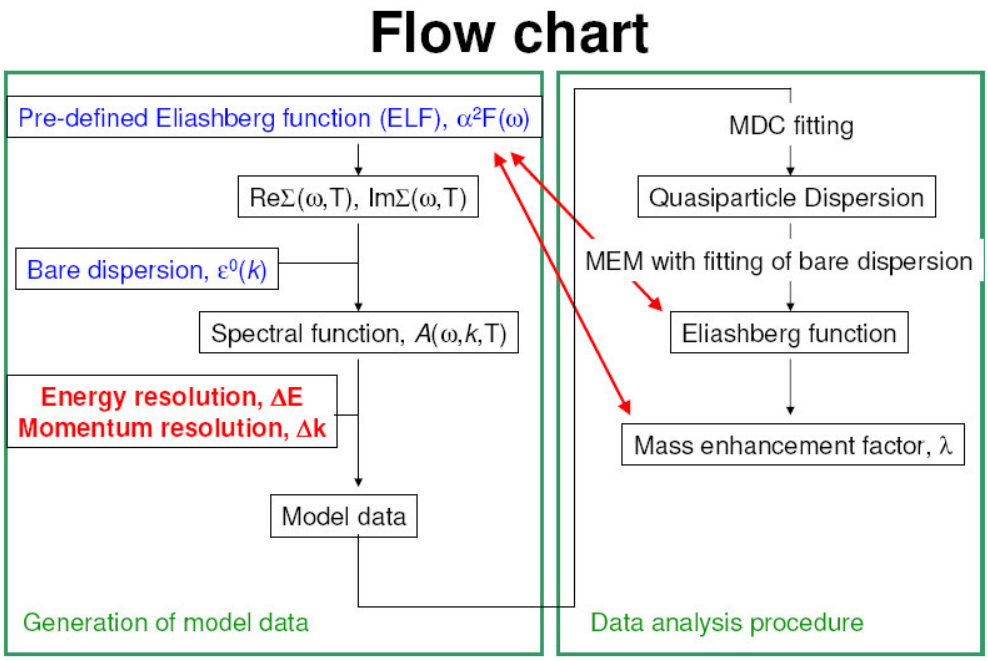

Figure 3.2. *Flow chart for the procedure to perform the simulation for studying the effects of the resolutions of the instruments, noise, and LA.*

dispersion relation; and (3) MEM to extract the Eliashberg function and mass enhancement factor. The comparison between the extracted and predefined ELFs and λ can give us insight of the effects from resolutions, LA and noise. In this simulation, we used two predefined ELFs and the corresponding $\mathrm{Re}\Sigma(\omega, T = 30K)$ and the $\mathrm{Im}\Sigma(\omega, T = 30K)$, as shown in figure 3.3 [19], which were calculated from Eq. (2-10) and Eq. (2-11), respectively. In this simulation, the temperature was set at 30 K, a typical experimental temperature, to calculate the self energies. To simulate the effects from electron-impurity scattering, 200 meV was added to the $\mathrm{Im}\Sigma$. The electron-electron interaction was considered negligible in this model.

The bare dispersion relations were set to be the same as the measured dispersion of the Be(0001) $\overline{\Gamma}$ surface state with the following parameters [2]: $E_b = -2.78eV$; $k_F = 0.947\text{Å}^{-1}$; and *n* = 2 in the equation:

$$\varepsilon^0(k) = -E_b\left(\left(\frac{k}{k_F}\right)^n - 1\right) \tag{3-3}$$

In this case, the effective mass is 1.2 m_e, where m_e is the free electron mass. In addition, for studying the robustness of LA, an additional two different bare dispersions were tested: Case II where the effective mass is 3.4 m_e: $E_b = -2.78eV$, $k_F = 1.579\text{Å}^{-1}$, and *n* = 2; Case III a non-free-electron-like system with varying effective mass: $E_b = -2.78eV$, $k_F = 0.947\text{Å}^{-1}$, and *n* = 3. Case I has parameters representing the Be(0001) surface state, mentioned above. For modeling the noise, two kinds of noise were added to the model data after the resolution convolution: (1) random noise, in which the uniformly distributed random number was used, and (2) Gaussian noise, in which the Gaussian distributed random number was used.

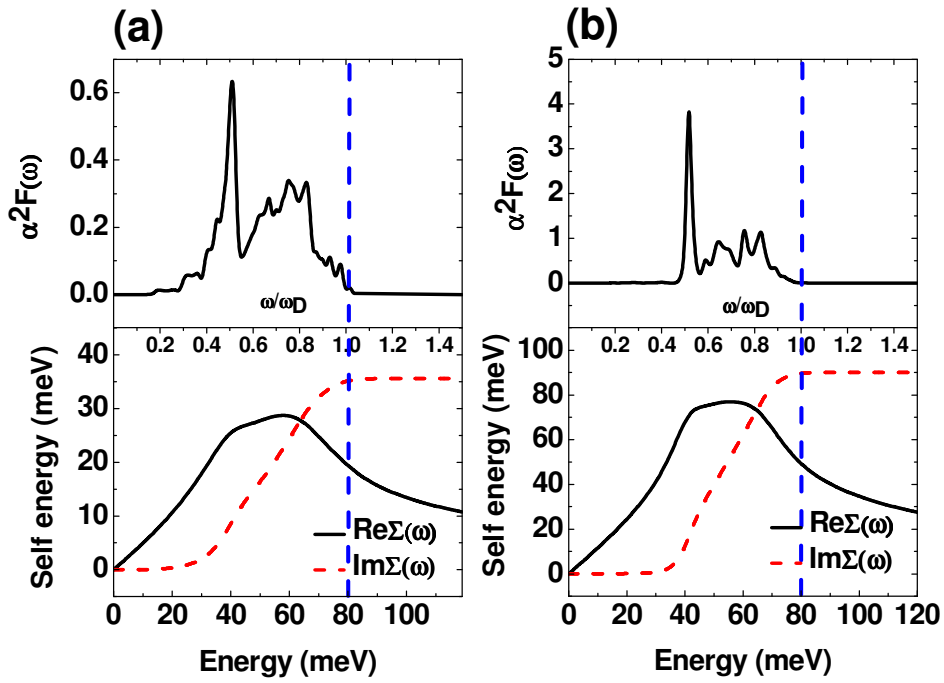

Figure 3.3. *Two different predefined ELFs and the corresponding self-energies, with the temperature set at 30K.*

B. Bare Dispersion Approximations

1. Linear Approximation (LA)

To clarify the validity of the LA, we set the energy and momentum resolution to be perfect: ΔE and Δk to be zero in Eq. (3-2). Thus, Eq. (3-2) reduces to the spectral function [Eq. (3-1)] times the Fermi-Dirac distribution function. Also, noise was not added to the model for simplicity. By using the LA, the bare dispersion in the spectral function was assumed as a linear function in the small *k* range: $\varepsilon^0(k) = v \cdot k + b$. Then, from Eq. (3-1), it is obvious that the MDCs can be fit as a Lorentz function with the peak position revealing the dispersion relation and the width related to the $\mathrm{Im}\Sigma$ by Eq. (2-22).

There are two possible sources for deviations of the LA results. First, the asymmetric line shape of MDCs is due to the non-linear bare dispersion fitted by the Lorentz function. When the bare dispersion is far from linear, or with a large curvature, the experimental MDCs will be asymmetric. As a consequence, the peak position and the width of the MDCs determined by the fitting with a Lorentz function will be affected. This can be seen by plotting the MDCs at a high binding energy. Fortunately, the bare dispersion near the Fermi energy has a small curvature, as shown in the upper panel of figure 3.1. According to our simulations, the shift of the peak position is within the typical experimental error and can be neglected. However, the asymmetric line shape will make the width inaccuracy observable, which will be shown later. Second, converting the relation between the FWHM of MDCs and the $\mathrm{Im}\Sigma$ (Eq. (2-22)) is also an approximation from the LA. The actual conversion relation is more complicated, and the difference can be large for the large curvature portion of the bare dispersion, which will be discussed with another two different approximations later.

2. Semi-Linear Approximation (SLA)

For the equation used for converting the FWHM of MDCs to $\mathrm{Im}\Sigma$, A. A. Kordyuk *et al.* have used a "semi-linear approximation" (SLA) [20]. In a SLA, the line shape of the MDCs are still approximated by the LA, thus Lorentz function is still used for fitting MDCs. But the converting equation for the FWHM of the MDCs and $\mathrm{Im}\Sigma$ is corrected by a quadratic function, as shown in the following [20]:

$$\mathrm{Im}\Sigma(\omega) = -\frac{1}{2}\frac{2E_b}{k_F^2}W(\omega)\sqrt{k_m^2(\omega) - \frac{W^2(\omega)}{4}} \tag{3-4}$$

where $\frac{2E_b}{k_F^2}$ is the second derivative of the bare dispersion, $\frac{\partial^2 \varepsilon^0}{\partial k^2}$, for quadratic bare dispersion; k_m is the peak position of each MDCs; and W is the FWHM of the MDCs. In this approach, the asymmetric line shape is still unsolved. In addition, when deducing Eq. (3-4), the $\mathrm{Im}\Sigma$ was assumed as binding-energy independent. As a consequence, Eq. (3-4) fails when the $\mathrm{Im}\Sigma$ depends strongly on the binding energy.

3. Quadratic Approximation (QA)

To solve the problems of asymmetric line shape and the converting equation from the width of MDCs to the $\mathrm{Im}\Sigma$, we proposed the "special MDCs" (MDCs*) concept by adopting a quadratic approximation (QA), in which the intensity of the ARPES is plotted as a function of k^2, instead of k, with a constant binding energy. The main idea of the MDCs* comes from the following: instead of LA, in QA, the bare dispersion is approximated as $\varepsilon^0(\vec{k}) = -\frac{E_b}{k_F^2}k^2 + E_b$. Then, the spectral function can be rewritten as:

$$A(\vec{k},\omega) \propto \frac{\mathrm{Im}\Sigma(\omega) \Big/ \left(\frac{E_b}{k_F^2}\right)^2}{\left[k^2 - k_F^2 + \frac{\omega - \mathrm{Re}\Sigma(\omega)}{E_b} k_F^2\right]^2 + \left[\frac{\mathrm{Im}\Sigma(\omega)}{E_b} k_F^2\right]^2} \tag{3-5}$$

As a result, the spectral function with constant binding energy and as a function of k^2 can be considered as a Lorentz function. Then, the FWHM of the MDCs* can be related to the $\mathrm{Im}\Sigma$ by:

$$\mathrm{Im}\Sigma(\omega,T) = \left| \frac{FWHM(MDCs*)}{4} \frac{2E_b}{k_F^2} \right| \tag{3-6}$$

where the factor, $\frac{2E_b}{k_F^2}$, as mentioned above, is equivalent to the second derivative of the bare dispersion.

4. Comparison Among LA, SLA, and QA

In order to test the validity of the LA, SLA, and QA, three kinds of bare dispersion relations, as mentioned above, were used. Other factors, such as the pre-defined $\mathrm{Re}\Sigma$ and $\mathrm{Im}\Sigma$, were set to be the same among all cases. Because these approaches approximate the non-linear bare dispersion to linear or quadratic form, validity of these approximations is considered as a function of the curvature of the bare dispersion [16]. In the following, the percent differences of the extracted $\mathrm{Im}\Sigma$ will be plotted as a function of the bare dispersion curvature. By using these three kinds of approximations, the $\mathrm{Im}\Sigma$ could be extracted from the model data. Figure 3.4 (a) - Fig. 3.4 (c) show the percent differences with respect to the pre-defined $\mathrm{Im}\Sigma$ as a function of the bare dispersion curvature from LA, QA, and SLA, respectively; while figure 3.4 (d) compares the extracted $\mathrm{Im}\Sigma$ by these three kinds of approximations from the experimental Be(0001) surface state data as a function of binding energy. In figure 3.4 (a), the LA case, the error of the extracted $\mathrm{Im}\Sigma$ increases while the curvature increases, except for the small hump around the small curvature

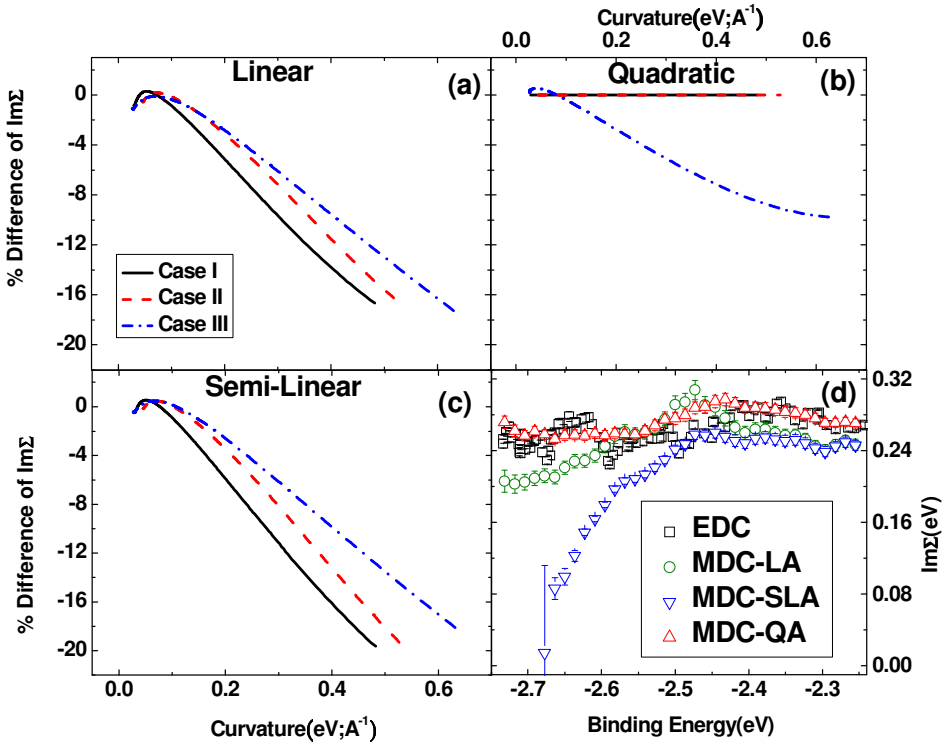

Figure 3.4. *(a) –(c) The percent difference between the extracted* $\mathrm{Im}\Sigma$ *from (a) LA; (b) QA; (c) SLA, and the predefined* $\mathrm{Im}\Sigma$ *as a function of the curvature of the bare dispersion. (d) Extracted* $\mathrm{Im}\Sigma$ *from the real data using different methods as a function of the binding energy.*

(near the Fermi energy). Though these three cases analyzed here have different bare dispersions, the trends of the curves are similar among each other. The differences among them might be caused by the different levels of asymmetric line shapes of the MDCs when they have the same curvature. Among these cases, when the curvature increases to ~0.3 (when the units of the bare dispersion are eV and $\mathring{A}^{-1}$), which correspond to the binding energy of 2.24 eV in the first case of the dispersion, the error of the extracted $\mathrm{Im}\Sigma$ is more than 10%. Another approach mentioned above is the SLA, shown in figure 3.4 (c). Obviously, the results are almost the same as the LA results, or even worse than the results of LA. Although SLA takes care of the problem of the relationship between $\mathrm{Im}\Sigma$ and FWHM of the MDCs, the extracted $\mathrm{Im}\Sigma$ is still very similar to the results of LA. This indicates that the main reason for the deviation of the $\mathrm{Im}\Sigma$ is from fitting the asymmetric line shape of the MDCs with a symmetric Lorentz function, not the relation between $\mathrm{Im}\Sigma$ and the FWHM of the MDCs. On the other hand, for the QA shown in figure 3.4 (b), the extracted value for Case I and Case II are exactly the same as the original values, no matter what the curvature (binding energy) is. On the other hand, in Case III, the extracted $\mathrm{Im}\Sigma$ behaves the same as the results from the LA. The reason is that the cubic form of the bare dispersion could be considered as a 1.5 power of k^2. It is equivalent to the case of using the LA to deal with the bare dispersion as a polynomial function with power 1.5. The MDCs* line shape becomes asymmetric in this case. If one indeed encounters a cubic dispersion, the cubic approximation might be used, instead of QA, to construct the MDC*. The importance of the concept of MDCs* is that it can provide a symmetric line shape for the Lorentz function fitting by adopting an appropriate bare dispersion relation in the spectral function.

To be more convincing, we used all three approximations mentioned above to extract $\mathrm{Im}\Sigma$ from the real data of the Be(0001) $\bar{\Gamma}$

surface state and compared them with the results extracted from the EDCs, which can work well near the bottom of the band, as shown in figure 3.4 (d). Because the curvature of the band is larger than 0.3(eV; $\AA^{-1}$) when the binding energy is larger than about 2.2 eV in the case of the Be(0001) $\bar{\Gamma}$ surface state, data with binding energies larger than 2.2 eV were chosen for comparison. The $\mathrm{Im}\Sigma$ from the EDCs were obtained as half width of the peak by fitting a Lorentz function convoluted with an energy resolution function. Then, $\mathrm{Im}\Sigma$ was calibrated by Eq. (2-18) [21], which is valid for quasi-2D systems and surface states (true 2D systems). It is clear that, as shown in figure 3.4 (d), the results from QA agree very well with the results from EDCs for the data within the chosen energy range (binding energy: 2.2 ~ 2.7 eV); while the LA starts to fail when the binding energy is larger than 2.6 eV, which corresponds to the curvature equal to 1.2 (eV; $\AA^{-1}$); SLA starts to fail when the binding energy is larger than 2.5 eV, which corresponds to the curvature equal to 0.8 (eV; $\AA^{-1}$). The reason for the higher tolerance on the curvature of real data than that of the simulated value [0.3 (eV; $\AA^{-1}$)] is that the real data always have error bars. The error in the real data determines the tolerance of the maximum curvature. For the data with binding energy smaller than 2.2 eV, all three approximations give similar values of $\mathrm{Im}\Sigma$ (not shown here). From this comparison, it is convincing that the LA and SLA can only be valid when the curvature is less than 1.0 $\pm$ 0.2 (eV; $\AA^{-1}$); while the QA is valid for the data from the Fermi energy to near the bottom of the Be(0001) $\bar{\Gamma}$ surface state. By converting the threshold curvature back to the threshold binding energy, the following equation is valid for the bare dispersion which is quadratic:

$$\varepsilon \geq \frac{1}{\sqrt[3]{16}}\left(\frac{k_F^2}{E_b}\right)^{1/3} - \frac{1}{4}\frac{k_F^2}{E_b} - E_b \qquad (3\text{-}7)$$

where ε is the threshold binding energy in eV units; k_F is the Fermi momentum in $\mathring{A}^{-1}$ units; and E_b is the bandwidth in eV units. In most cases, the interesting energy range is near the Fermi energy, which is far from the threshold binding energy; in other words, it is safe to use the LA for those cases. Other important information to be pointed out is that the SLA fails with a smaller curvature than the LA does. This also was confirmed by the simulation results. To recap, it is better to use LA for the small curvature data, instead of SLA, and to use QA for the large curvature data, where LA seems to fail.

C. Influences from Instrumental Resolutions

1. Modeling Resolutions

Here, the parameters of Case I for the bare dispersion were used to simulate the Be(0001) $\bar{\Gamma}$ surface state. To simulate the contribution from the electron-impurity interaction, which always appears in the experimental data, a constant of 200 meV of $\mathrm{Im}\Sigma$ was added. According to the analysis above, the QA for fitting the MDCs are very accurate for both $\mathrm{Re}\Sigma$ and $\mathrm{Im}\Sigma$, so QA was used in the following study. It was also confirmed that the results using the QA agree very well with the results using the LA throughout the following study. Model data with the following resolutions were generated: (1) ΔE = 5 meV; and Δk = 0.001 $\mathring{A}^{-1}$; (2) ΔE = 5 meV and Δk = 0.01 $\mathring{A}^{-1}$; (3) ΔE = 5 meV and Δk = 0.1 $\mathring{A}^{-1}$; (4) ΔE = 30 meV and Δk = 0.001 $\mathring{A}^{-1}$; and (5) ΔE = 60 meV and Δk = 0.001 $\mathring{A}^{-1}$, in which (1) – (3) have the same energy resolution but different momentum resolutions; (1), (4), and (5) have the same momentum resolution but different energy resolutions. After $\mathrm{Im}\Sigma$ was extracted, the value of $\mathrm{Im}\Sigma$ at the Fermi energy was subtracted from the total $\mathrm{Im}\Sigma$, as was usually done in analyzing the experimental data. The amount subtracted is considered as the contribution from the electron-impurity

scattering. The contribution from the electron-electron interaction is neglected here.

2. Resolution Effects Extracting Dispersion

First, to determine the influence of the energy resolution and momentum resolution on the extraction of the dispersion and the width of the data, we extracted the dispersion and width from model numbers (1) through (5). Figure 3.5 (a) shows the results from model data numbers (1) through (3). In this set of data, the energy resolution is fixed at 5 meV; while the momentum resolutions change from 0.001 to 0.1 $\AA^{-1}$. It is clear that the momentum resolution does not affect the resulting dispersion, as long as the momentum resolutions are better than 0.01 $\AA^{-1}$. Fortunately, even for the case of momentum resolutions up to 0.1 $\AA^{-1}$, the whole dispersion was rigidly shifted without distortion. This will not affect the extraction of the $\mathrm{Re}\Sigma$ nor the determination of the bare dispersion. On the other hand, figure 3.5 (b) shows the results from model data numbers (1), (4), and (5), in which the momentum resolution is fixed at 0.001 $\AA^{-1}$ and the energy resolutions change from 5 to 60 meV. In this case, severe distortions are observed near the Fermi energy and the kink. When the energy resolution is increased more, the dispersion distorts more, especially for the dispersion near the Fermi energy. As a consequence, the determination of the Fermi momentum, k_F, becomes non trivial. From figure 3.5 (a) and figure 3.5 (b), we can conclude that the momentum resolution has a limited effect on the extracted dispersion, while the energy resolution will distort the dispersion significantly. In addition, this distortion will result in making further analyses more difficult.

To further understand the distortion from the energy resolution, we generated another two sets of model data. For these two sets, the momentum resolution was set at 0.001 $\AA^{-1}$, and the energy resolution was changed from 0 to 25 meV in 5-meV steps. One set of data was

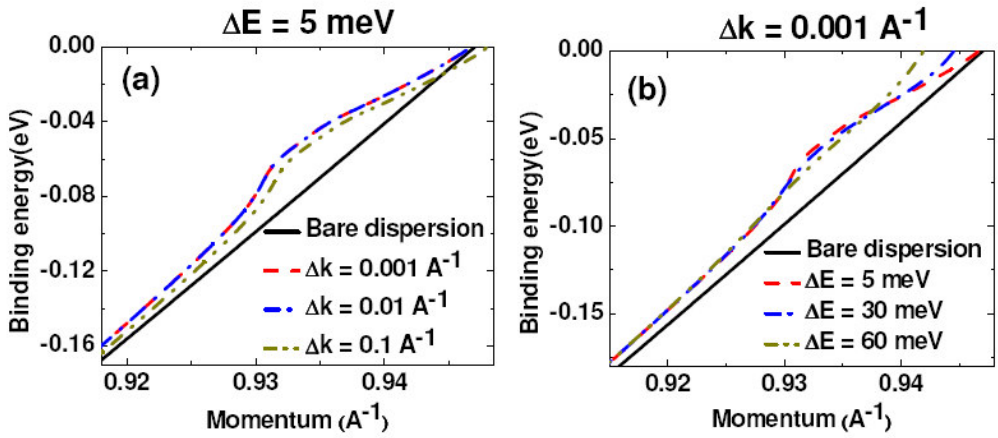

Figure 3.5. *The extracted dispersion for model data having different instrumental resolutions.*

simulated without the Fermi distribution function, and the other set was simulated without the EPC renormalization part. The results are shown in figure 3.6. Figure 3.6 (a) shows the results for model data without the kink but with the Fermi distribution function; while figure 3.6 (b) shows the results for model data without the Fermi distribution function but with the kink. From figure 3.6 (a), one observation is that the distortion is most severe at the Fermi energy and deviates less and less when the binding energy increases. After further checking the deviation, we can conclude that the distortion only extends to the binding energy that is the same as the energy resolution. For example, when the energy resolution is 15 meV, the distortion extends to the data with binding energies less than 15 meV. This is an indication that the distortion is due to the coupling between the Fermi distribution function and the Gaussian convolution function. From figure 3.6 (b), the most severe distortion appears near the kink. The kink is smeared and decreased. To see closely, we subtract the bare dispersion from the resulting dispersion and generate the real part of the self-energy, as is shown in figure 3.7. It is very clear now that the resulting real part of the self-energy decreases when the energy resolution increases. Further, for the 0-meV case, there are still some “features” in the real part of the self-energy, but for the case of 25 meV, these features are smeared out. From here, we can conclude that the energy resolution will suppress the kink and smear out the information in the kink. If you combine both conclusions, the most severe distortion is very close to the Fermi energy because of the Fermi distribution step, and the kink is suppressed and smeared.

The determination of the Fermi momentum is very important for studying the shape and the area of the Fermi surface contour. To understand how the energy resolution can affect the Fermi momentum value from the experiment, we ran a systematic simulation to determine the Fermi momentum. Deviations of the Fermi momentum as a function of

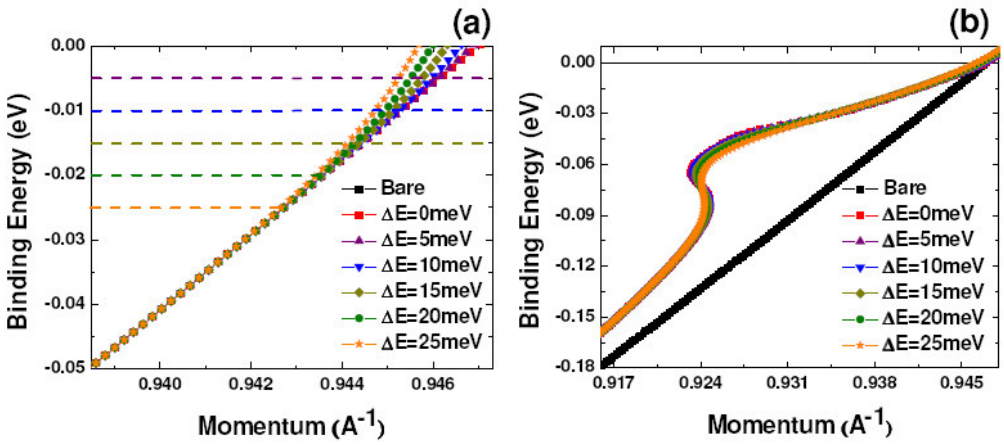

Figure 3.6. *Extracted dispersion for model data without (a) EPC renormalization and (b) Fermi distribution function. The momentum resolution is set at 0.001* $\mathring{A}^{-1}$*; while the energy resolutions change from 0 to 25 meV in 5-meV steps.*

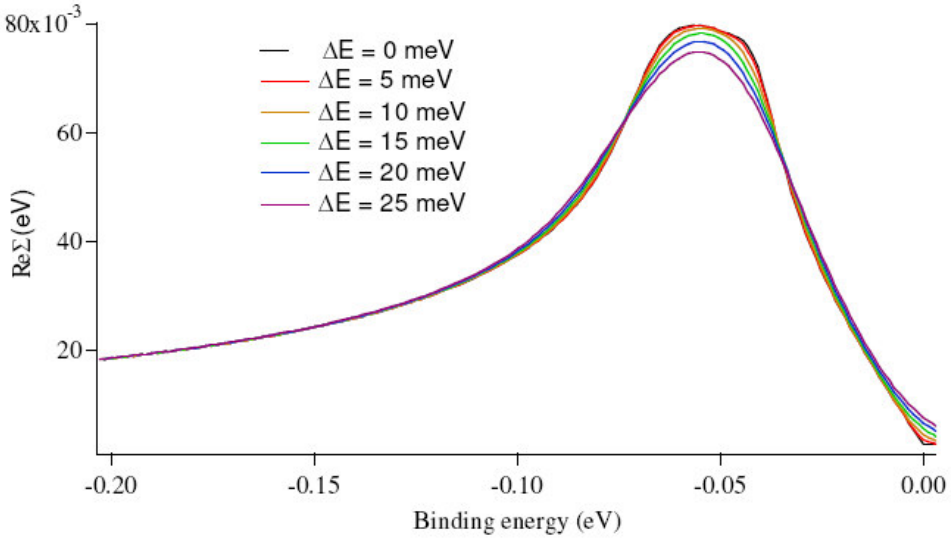

Figure 3.7. *The extracted real part of the self energy from the model data in Fig. 3.6(b).*

the energy resolution and effective mass of the bare dispersion are shown in figure 3.8. The effective mass tested here is ranging from 0.62 free electron mass to 2.5 free electron mass. First observation is that the deviation of the Fermi momentum increases when the energy resolution increases. Second, for the same energy resolution, higher effective mass would have larger deviation. In other word, if the band curvature is larger, the deviation would be larger. It is worth noting that the typical energy resolution for the experiment using synchrotron radiation as the light source is about 15 meV. For this case, the deviation of the Fermi momentum can reach 0.005 $\AA^{-1}$, which might be noticeable when the angular resolution is high enough. When studying the area of the Fermi surface, this deviation can induce a non-negligible error.

3. Resolution Effects on Extracting $\mathrm{Im}\Sigma$

The resolution influences from extracting $\mathrm{Im}\Sigma$ were studied. Figure 3.9 (a) shows the resulting $\mathrm{Im}\Sigma$ from the model data with the same energy resolution (5 meV), but with different momentum resolutions (0.001, 0.01, and 0.1 $\AA^{-1}$;). The extracted values are very close to the predefined values even when the momentum resolution is up to 0.01 $\AA^{-1}$. When the momentum resolution is increased to 0.1 $\AA^{-1}$, the extracted values are quite wrong everywhere. This is because the line shape of the MDCs* is distorted severely from the Lorentz function. It was also confirmed that the line shape of the MDCs from the LA was severely distorted as well. The extracted $\mathrm{Im}\Sigma$ from the LA is also similar to the results from the QA. On the other hand, figure 3.9 (b) shows the results from the model data with the same momentum resolution (0.001 $\AA^{-1}$), but with different energy resolutions (5, 30, and 60 meV). When the energy resolution is ~5 meV, the error between the extracted values and the predefined values are less than 1 % for all binding energies studied here. In the case where the energy resolution was 30 meV, the extracted $\mathrm{Im}\Sigma$ of the high binding

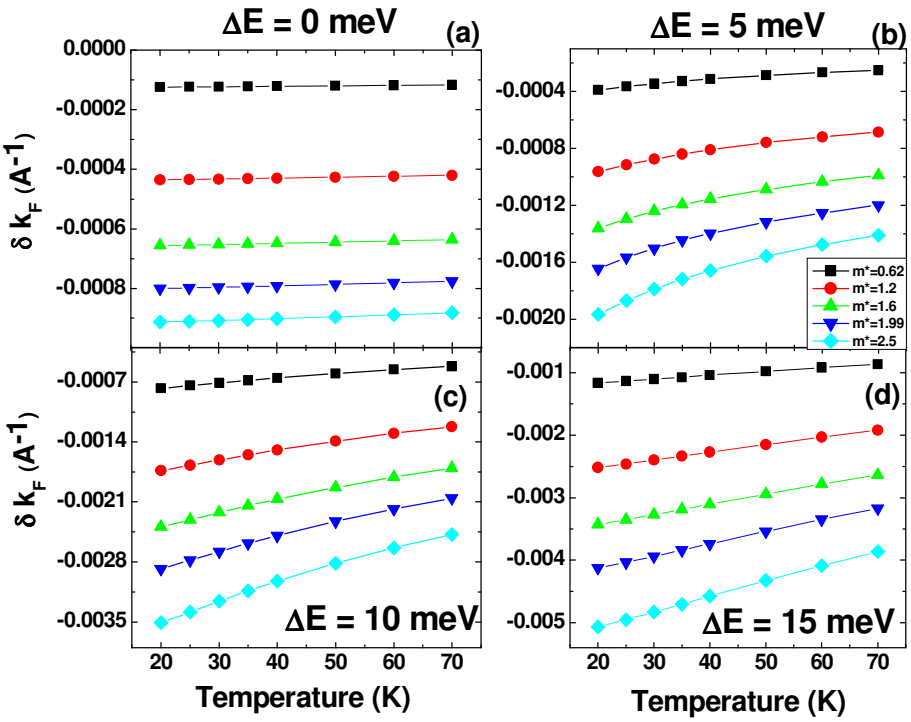

Figure 3.8. *Deviations of the Fermi momentum as the function of energy resolution and the effective mass of the bare dispersion.*

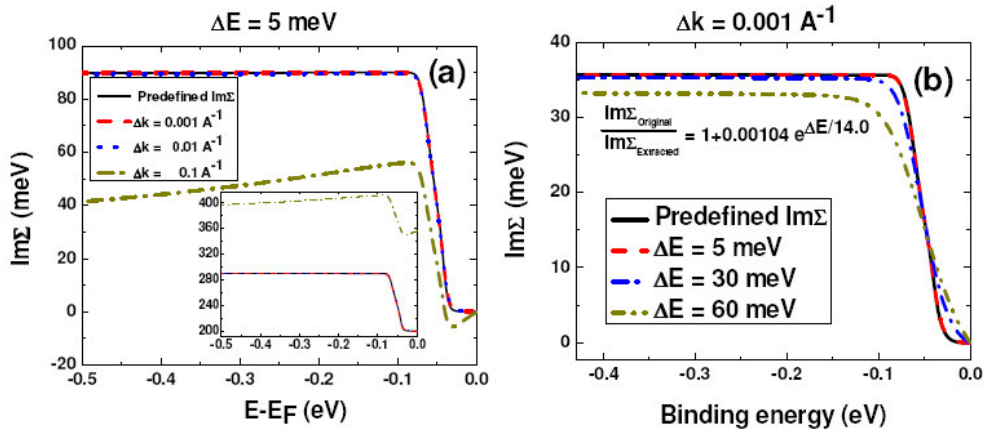

Figure 3.9. *Extracted* $\mathrm{Im}\Sigma$ *from the model data with (a) fixed energy resolution and different momentum resolutions and (b) fixed momentum resolution and different energy resolutions.*

energy decreases but with a similar trend—saturating when the binding energy is higher than the kink energy scale (~80 meV). However, $\mathrm{Im}\Sigma$ near the Fermi energy deviates from the predefined values significantly. It originates from the smearing effects of the energy resolution. The smearing effects also occur in the extracted $\mathrm{Re}\Sigma$, which was shown previously. When the energy resolution was 60 meV, the extracted $\mathrm{Im}\Sigma$ with a high binding energy decreased even more, while the $\mathrm{Im}\Sigma$ near the Fermi energy distorts more severely than that of the 30-meV energy resolution case. Because the value of the saturated $\mathrm{Im}\Sigma$ is needed in the MEM fiiting, which will be discussed later, the correction of the saturated $\mathrm{Im}\Sigma$ value should be considered. The decrease of the saturated extracted $\mathrm{Im}\Sigma$ at a high binding energy due to the energy resolution was studied in finer energy resolution intervals (not shown here). The correction equation of the saturated $\mathrm{Im}\Sigma$ as a function of the energy resolution is inserted in figure 3.9 (b), where the ΔE is in meV units. According to this simulation, the momentum resolution has less influence on the extracted $\mathrm{Im}\Sigma$ than the energy resolution does and can be neglected when the momentum resolution is as good as the 0.01 $\mathring{A}^{-1}$ order. In fact, extraction of the $\mathrm{Im}\Sigma$ requires information from the bare dispersion, such as the Fermi momentum, k_F, and the band width, E_b, as shown in Eq. (3-3). The predefined values, k_F = 0.947 $\mathring{A}^{-1}$ and E_b = -2.78 eV, were used here to deduce the $\mathrm{Im}\Sigma$ in order to simplify the question to simply focus on the resolution effects on the extraction of $\mathrm{Im}\Sigma$. The bare dispersion relation used in the experimental data, affected by the energy and momentum resolutions, will be considered later.

4. Resolution Influence on Extracting $\mathrm{Re}\Sigma$, ELF, and λ

Here, resolution influences for extracting $\mathrm{Re}\Sigma$ were studied. It is well-known that the typical energy and momentum resolutions affect the

raw data of ARPES significantly, especially for the data near the Fermi energy. In the literature, there is only one report where this problem was studied carefully [10]. However, resolution effects on the extraction of the bare dispersion, the fine structure in the $\mathrm{Re}\Sigma$ from ARPES data, and the ELF as well as the mass enhancement factor, λ, were not found in the literature. In this study, the effects of the energy and momentum resolutions on the above-mentioned issues were studied.

The maximum entropy method (MEM), developed by J. Shi *et al.* [1], was used to extract the $\mathrm{Re}\Sigma$, ELF, and mass enhancement factors, λ. Concerning using MEM on LSCO, T. Valla wrote a comment that questioned the energy resolution effects using MEM [11]. He asserted that the energy resolution in the experiment will make the fine structure unobservable experimentally. Although X. J. Zhou *et al.* wrote a reply on this issue [12], the energy resolution effects on MEM still needed to be carefully studied.

In MEM, the bare dispersion was deduced by varying *a* and *b* in the function, $\varepsilon^0(k) = a(k-k_F)^2 + b(k-k_F)$, to get the best fit of the $\mathrm{Re}\Sigma$ and the dispersion [1]. The value of the Fermi momentum, k_F, was set to the experimental value and deduced from the MDC at the Fermi energy. As discussed above, the energy resolution will distort the data near the Fermi energy severely, as well as the value of the Fermi momentum. Therefore, the extracted ELF using MEM with experimental data should be questioned solely because of the uncertainty of the Fermi momentum. With an understanding from our simulation, we proposed a procedure to improve MEM.

With knowledge of the sources of the distortion studied above, an improvement procedure can be proposed when using MEM. Because the main information of the EPC is from the kink and the most distorted part of the data is near the Fermi energy, we proposed that the data with a binding energy less than the value of the energy resolution should be

discarded before performing MEM. In order to be sure that important information is not discarded during this process, it is suggested that the energy resolution should be at least better than 1/3 of the binding energy when the maximum of the kink appeared. For example, in the case of the Be(0001) $\overline{\Gamma}$ surface state, the maximum of the kink appears at binding energies around 50–60 meV, so the energy resolution should be better than 17–20 meV. However, because the data near the Fermi energy were discarded, any resulting peak in the extracted ELF with energy less than the threshold energy is questionable. The only way to obtain information with a low binding energy is to improve the energy resolution experimentally. It is necessary to mention that the value of k_F used in MEM should be changed to a fitting parameter, instead of the value obtained from the MDC at E_F. However, when one more fitting parameter is added, the results of the fitting are less determinate. To solve this problem, fitting of the $\mathrm{Im}\Sigma$ should be considered, in addition to the fitting of the $\mathrm{Re}\Sigma$ and the dispersion of the data in the original MEM procedure. When the fitting is converged with $\mathrm{Re}\Sigma$, $\mathrm{Im}\Sigma$, and the dispersion, the ELF and the value of λ are more determinate and more trustworthy.

By adopting MEM with the discarding process mentioned above, the ELF can be extracted, as shown in figure 3.10. Figure 3.10 (a) and figure 3.10 (b) show the extracted ELF along the $\overline{\Gamma}-\overline{K}$ and $\overline{\Gamma}-\overline{M}$ directions (black solid lines), respectively, with different energy resolutions up to 25 meV. In addition to the extracted ELF, the predefined ELF and smeared ELF (red dashed lines) were also plotted. Surprisingly, the extracted ELF, for both directions, can be described very well by the smeared ELFs, which are calculated directly from the convolution of the predefined ELF with corresponding energy resolutions. The smeared ELFs (red dashed lines) are almost overlapping with the extracted ELFs (black solid lines). For comparison, results using MEM without the discarding process (original procedure) were also used to extract the ELF

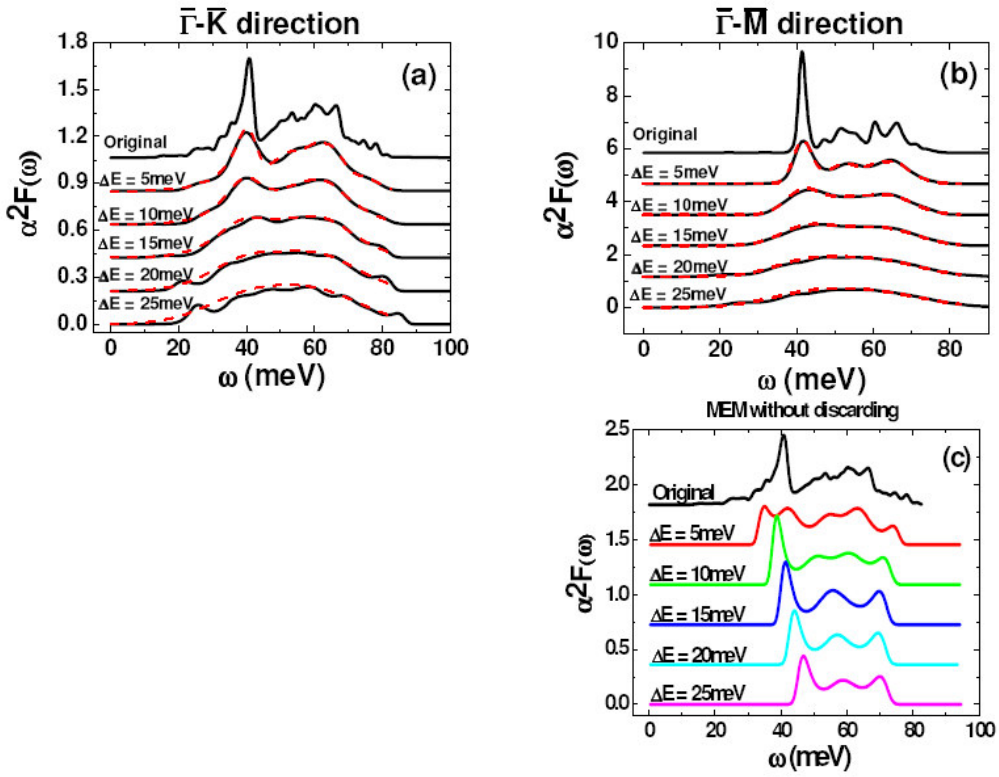

Figure 3.10. *(a), (b) Extracted ELFs with a new procedure from two different sets of model data with different predefined ELFs. (c) Extracted ELFs from the old procedure for comparison.*

along the $\overline{\Gamma}-\overline{K}$ direction, as plotted in figure 3.10 (c). It is clear that the extracted ELFs are quiet different from the predefined ELF. Because the data near the Fermi energy are severely distorted, determination of the bare dispersion, as well as the Fermi momentum, is ambiguous. This is the main reason for the incorrect ELF results from the original procedure. In the literature, determination of the exact Fermi momentum from the experimental data was discussed [22, 23]. However, even though the Fermi momentum can be found experimentally, the distorted part of the data still can generate artificial features in the extracted ELF by MEM. On the other hand, in our case, the Fermi momentum was set to be a fitting parameter, and all of our resulting Fermi momentums were found to be very close (<5 %) to the predefined values, even when the energy resolution was as bad as 25 meV.

Physically, the mass enhancement factor, λ, is used to express the strength of EPC. The mass enhancement factor can be related to the ELF, $\alpha^2 F(\omega)$, from Eq. (2-8). Figure 3.11 shows the resulting mass enhancement factors, λ, with different energy resolutions along the $\overline{\Gamma}-\overline{K}$ and $\overline{\Gamma}-\overline{M}$ directions, calculated directly from the extracted ELF in figure 3.11. The horizontal dashed lines indicate the mass enhancement factors calculated from the predefined ELF. In both directions, when using MEM without discarding the distorted data, the mass enhancement factors decreased rapidly while the energy resolution increased (stars). This confirms the results of the wrong ELF as shown above [figure 3.11 (c)]. On the other hand, if the distorted data were discarded, the mass enhancement factors can remain within a 10% error for both the $\overline{\Gamma}-\overline{K}$ and $\overline{\Gamma}-\overline{M}$ directions when the energy resolution is increased up to 25 meV. In fact, this error is less than the usual experimental error bar in the literature. The mass enhancement factor calculated from the extracted ELF can be reproduced even when the energy resolution reaches the 25-

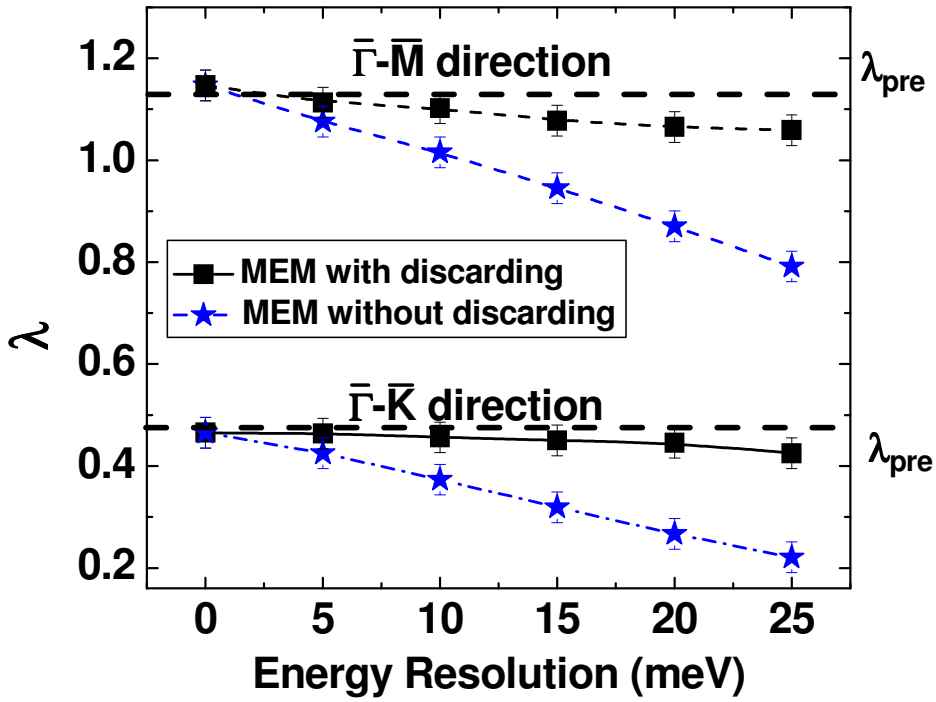

Figure 3.11, *Extracted mass enhancement factors from different model data by new procedure (solid squares) and old procedure (solid stars). The dashed lines are the predefined* λ *.*

meV level for the Be(0001) $\overline{\Gamma}$ surface state. In principle, when the smeared ELF is obtained from the noise-free data, it is possible to do the de-convolution to obtain the predefined ELF. The problem is, there are no noise-free data. The noise effect also needed to be studied.

D. Noise

To simulate the influence from the noise, two kinds of noise were added to the model data: (1) uniformly distributed noise and (2) Gaussian distributed noise. The Case I bare dispersion mentioned above was chosen; the ELF, $\mathrm{Re}\Sigma$, and $\mathrm{Im}\Sigma$ along the $\overline{\Gamma}-\overline{M}$ direction were also chosen. The energy and momentum resolutions were set at 15 meV and 0.001 $\mathring{A}^{-1}$, respectively. For each noise level, there were five tests. In other words, following the MEM procedure, five ELFs were extracted from each noise level. To quantify the effect, correlation coefficients R_1 and R_2 were calculated from each pair of ELFs for each noise level by the following definitions:

$$R_n = \frac{\int \left| I_1 - cI_2 \right|^n d\omega}{\int I_1^n d\omega} \qquad n \in 1, 2 \tag{3-8}$$

where $c = \dfrac{\int I_1 d\omega}{\int I_2 d\omega}$ and I_1, and I_2 represent the pair of ELFs chosen for calculating the correlation coefficient. The resulting correlation coefficient R_1 and R_2 were plotted as a function of signal-to-noise ratio (SNR) of $\mathrm{Re}\Sigma$ in logarithmic decibel scale, which is defined as:

$$SNR(dB) = 10 \cdot \log_{10}\left(\frac{P_{signal}}{P_{noise}}\right) = 20 \cdot \log_{10}\left(\frac{A_{signal}}{A_{noise}}\right). \tag{3-9}$$

P_{signal} and P_{noise} are the average power of signal and noise, respectively, and A_{signal} and A_{noise} are the root-mean-square amplitude of signal and noise, respectively. Surprisingly, the extracted ELFs were not repeatable

until the SNR(dB) reached ~45. Figure 3.12 (a) shows the extracted ELFs as well as the $\mathrm{Re}\Sigma$ (inset) of the data with SNR(dB) equal to 39 and 45, respectively. It is clear, from the upper panel of figure 3.12 (a), that the ELFs are not repeatable even when the SNR(dB) is as good as 39, which is considered to be very high quality data. For data with lower SNR(dB), the ELFs are also not repeatable (not shown here). In comparison with the noise-free data, the ELFs extracted from the noise-free data were also plotted (black solid dots) in the lower panel of figure 3.12 (a). The ELFs extracted from the noisy data (SNR(dB) = 45) agree quiet well with the noise-free ones. Fortunately, even though the ELFs are not repeatable at low SNR(dB) data, the mass enhancement factors calculated from them are quiet robust. The resulting correlation coefficients, R_1 and R_2, and mass enhancement factors are shown in figure 3.12 (b). First, it is clear that the correlation coefficients as well as the error bars of the correlation coefficients decrease (more correlation) as a function of the SNR(dB). This corresponds to the unrepeatable ELFs for the low SNR(dB). On the other hand, the mass enhancement factors are quiet robust against the noise. It can be seen that the mass enhancement factors are within 10% error even for the SNR(dB) as low as 6. Another point that needs to be mentioned is that the mass enhancement factors increase as the SNR(dB) decreases. In other words, the mass enhancement factors extracted from the noisy data are larger than the predefined values. In short, the ELFs extracted from data with SNR(dB) smaller than ~45 by using MEM are questionable. Experimentally, repeating the measurements of the ELFs seems to be the best strategy to exclude the noise effect. On the other hand, the mass enhancement factors from the noisy data using MEM can be trusted even for the data with SNR(dB) as low as 6. The bottom line is, as long as the $\mathrm{Re}\Sigma$, $\mathrm{Im}\Sigma$, and the dispersion relation can be fit well, the mass enhancement factors deduced from MEM are robust.

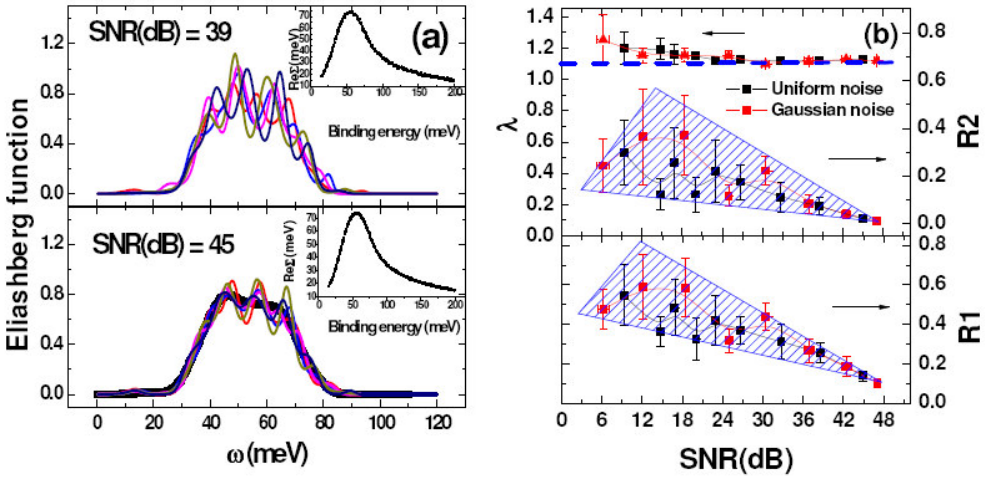

Figure 3.12. *(a) Repeatability tests for the extracted ELFs from MEM from the noisy data. The insets are the corresponding real part of the self-energy. (b) Correlation numbers from different noise levels and the mass enhancement factors extracted from the noisy data.*

In practicality, the above-mentioned procedure was tested experimentally by changing the energy resolutions intentionally during measurements using ARPES on the Be(0001) surface state. The measurements were conducted along the $\overline{\Gamma}-\overline{M}$ direction, with overall energy resolutions of 17, 18, and 27 meV by adjusting the synchrotron photon resolution only. For convenience purposes, hereafter, the data with energy resolutions of 17, 18, and 27 meV are denoted as data (I), (II), and (III), respectively. The dispersions deduced from the experiments by fitting MDCs* are shown in figure 3.13. It was also confirmed that the results from fitting the MDCs with a Lorentz function using the LA are the same. From figure 3.13, it is clear that the data near the Fermi energy are distorted, as the simulation predicted. After following the procedure mentioned above, the mass enhancement factors were deduced. It was found that the mass enhancement factors were all 0.4 $\pm$ 0.1 for data (I), (II), and (III). The SNR(dB) of data (I), (II), and (III), determined from the $\mathrm{Re}\Sigma$, are 11.3, 4.4, and 20.3 respectively. The ELFs are not repeatable (not shown here) as predicted from the simulation. The value of the mass enhancement factor deduced here is quiet small when compared with the values from the literature. The explanation is, our data were taken when the surface was contaminated slightly and/or was somewhat slightly rough. This was confirmed from the existence of a non-dispersive defect peak with binding energy around 1 eV in the spectrum. However, the validity of the procedure was well proven by the robustness of the values of the mass enhancement factors.

Summary

Validity of the LA, effects from the energy and momentum resolutions, and the effects from noise in analyzing ARPES were discussed. First, it was found that, when the curvature of the bare dispersion is too large, the LA used in the MDC analysis should be

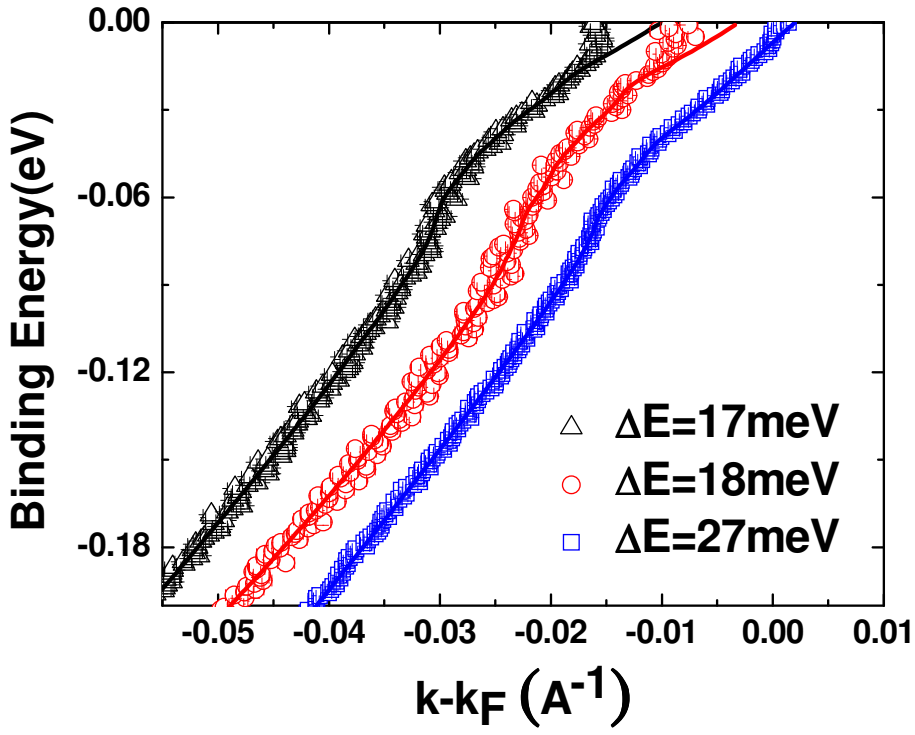

Figure 3.13. *Experimental data from the Be(0001) $\overline{\Gamma}$ surface state, measured with different energy resolutions.*

considered as flawed. The special MDCs (MDCs*) concept successfully solved the problem. On the other hand, the SLA worked worse than both the LA and QA in the case of the Be(0001) surface state. The phenomenal equation for the valid binding energy for LA is shown in Eq. (3-7).

Second, it is found that the momentum resolution has a minor influence on extracting the bare dispersion, but has a major influence on extracting the $\mathrm{Im}\Sigma$. The correction equation of the saturated $\mathrm{Im}\Sigma$ is shown in figure 3.9 (b). In contrast, the energy resolution distorts the bare dispersion severely, especially for the data near the Fermi edge and kink, but not for the extracted $\mathrm{Im}\Sigma$. The distortion of the dispersion near the Fermi energy due to the energy resolution can only reach a binding energy as high as the number of the energy resolution. The suggested experimental energy resolution for the many-body system study should be better than 1/3 of the kink energy. In further analyses, following the MEM proposed by J. Shi *et al.*, an improved procedure using MEM was proposed. The mass enhancement factor deduced from the improved procedure could have very small error.

Third, the inevitable noise in the real data was found to make the extracted ELFs questionable when the SNR(dB) of the $\mathrm{Re}\Sigma$ is smaller than ~45. Repeatable ELFs from several measurements are needed to exclude the noise effects on extracted ELFs. It was also found that the mass enhancement factors deduced from the noisy data using MEM can be very robust, less than 10% error, even for the SNR(dB) as low as 6.

Chapter IV
Anisotropic Electron-Phonon Coupling on a Two-Dimensional Isotropic Fermi Contour: $\bar{\Gamma}$ Surface State of Be(0001)

Introduction

As the condensed matter community turns its attention to complex and correlated electron materials, it is extremely important to understand the details of the coupling between the active degrees of freedom such as charge, lattice, orbital, and spin [1]. The exotic properties and useful functionality of some new materials result from the coexistence of competing and nearly degenerate states, which can be manipulated by either external or internal perturbations. One particularly important ingredient of this is the coupling of electronic states to lattice vibrations or, more generally, any other bosonic excitation. Using a combination of ARPES [2] and theory [3], a clearer picture of the electron-boson coupling is starting to emerge; for instance, for the high-T_c superconductors [2, 4, 5], the colossal magnetoresistive manganites [6], superconducting MgB_2 [3], and sheets of graphene [7]. However, for the high-T_c superconductors in particular, a detailed understanding of the coupling is still outstanding in spite of its paramount importance. It is still unclear, for instance, if the coupling is primarily to phonons or other bosonic modes or even if the coupling is isotropic or anisotropic over the (very anisotropic) Fermi contour [3, 4, 7–9]. Indeed, such details are very hard to establish because of the simultaneous presence of different bosonic modes, band folding effects for electron-doped cuprates [9], and other complications. Here, we address a key question for the general understanding of electron-boson coupling: Can the coupling be anisotropic even when the

electronic states are isotropic? We use a Be(0001) surface state to tackle this problem. In contrast to the high-T_c superconductors, this has the important advantage that the relevant bosonic modes are known to be phonons only.

Using beryllium surfaces as a test system has a number of other advantages. The first is the electronic simplicity of Be, which has in the past permitted an accurate description of the electronic [10, 11], structural [11], thermal [12], and dynamic [13, 14] properties by density functional theory (DFT). Another advantage is the strong bonding in beryllium and the small atomic mass, which lead to high phonon energies (up to ~85 meV [13]). Consequently, the effects of the EPC can be observed over a wide energy range, reducing requirements on the experimental energy resolution. Closely related to this is the high Debye temperature of beryllium which means that it is a good approximation to interpret the data as if they were taken at T = 0 K, even if the actual experiment was not performed at a very low temperatures. Finally, the (0001) surface of beryllium supports a simple, free-electron-like surface state which is centered at the zone center $\overline{\Gamma}$ and has a Fermi contour that is circular (isotropic) within ~1% [15, 16] with a Fermi wave vector length of ~0.947 $\mathring{A}^{-1}$.

Given these favorable conditions, it is unsurprising that the EPC of this surface state has already been subject to several investigations, both experimental [17–21] and theoretical [22]. So far, the state of affairs with respect to the strength of the EPC is somewhat inconclusive. Early ARPES measurements of the EPC near the Fermi level indicated that the state exhibits anomalously large EPC [17–21]. DFT calculations of the EPC of the Be(0001) surface also suggested strong coupling and explained it in terms of coupling to the Rayleigh surface phonon mode [22]. However, subsequent reports have significantly widened the range of experimental λ values (defined as $\lambda = m_{eff}/m_0 - 1$). The reported

values differ by almost a factor of 2, spanning the unsatisfactorily large range from 0.7 to 1.18 [17–21]. Here, we resolve this inconsistency in the published results for the mass enhancement.

There are at least three possible explanations for the inconsistency in the published values of λ: (1) λ is anisotropic in $\vec{k}$ space (the reported λs were measured at inequivalent points on the circular Fermi contour); (2) there are deviations in λ caused by the method used to extract λ from the data (the reported λs were extracted using different methods); and (3) the quality of the data may affect the extracted value of λ. In the following, It is shown that the EPC associated with the $\overline{\Gamma}$ surface state on Be(0001) is, in fact, anisotropic. It is also illustrated how the resulting value of λ can be influenced by the method used to extract it, and it is finally argued that oxygen contamination is a likely reason for one of the observed low λ values.

Experiment

ARPES experiments were performed at the SGM-3 beamline of the synchrotron radiation source ASTRID in Aarhus, Denmark [23]. The total energy resolution was set at ~15–20 meV; the angular resolution of the analyzer was 0.2°; and the photon energy was 16 eV. The sample was cooled to approximately 70 K with a closed-cycle He cryostat, and the surface was cleaned by several cycles of Ne-ion bombardment at an elevated temperature (450℃), followed by annealing at 550℃. The base pressure was in the low 10^{-10}-mbar range. Initially, the cleanliness of the surface was checked by Auger electron spectroscopy. Later, when the level of oxygen contamination (the main contaminant) had fallen below the detection limit of this technique, the Be 1s core-level peak and the valence band were checked for charcteristic oxygen-induced spectral features. A very small amount of oxygen could always be detected in the valence

band, but it was confirmed that it did not influence the results presented here. At significantly higher levels of oxygen contamination, a diminished EPC strength in the valence band was observed. The orientation of the sample was determined by low-energy electron diffraction (LEED) and Fermi surface mapping at 60 eV photon energy.

Data Analysis

The upper part of figure 4.1 (a) shows the photoemission intensity at the Fermi energy together with a sketch of the surface Brillouin zone and the expected Fermi contours (black dashed half-circles and ellipses). There are two surface states crossing the Fermi energy. One is centered around $\overline{\Gamma}$ and gives rise to a circular Fermi contour with a radius of about 0.94 $\mathring{A}^{-1}$ (the $\overline{\Gamma}$ state in the following). The other is centered around $\overline{M}$ and gives rise to an elliptic Fermi contour. High-resolution data for the $\overline{\Gamma}$ state were taken at a photon energy of 16 eV for different points on the circular Fermi contour. The present experimental arrangement does not allow for rotation of the sample around the surface normal such that it was not possible to measure radial cuts through every point on the Fermi surface. Instead, data were taken along the 14 cuts shown in the lower part of figure 4.1 (a). The cuts become more non-radial as the angle away from the $\overline{\Gamma} \rightarrow \overline{M}$ direction increases. In the following, we determine the dispersion and the EPC strength based on these cuts, ignoring their non-radial nature. Using simulated spectral functions, it has been confirmed that this leads only to very minor changes in the resulting λ values. Figure 4.2 shows the simulation results. A 2D Debye model was used to generate model data, and it predefined λ and ω_D to be varying. Because the non-radial cut only generates the non-radial bare dispersion plus non-radial $\mathrm{Re}\Sigma$, the EPC strength will not be affected by these factors. The only influence is the slight uncertainty on the angle determination, which is

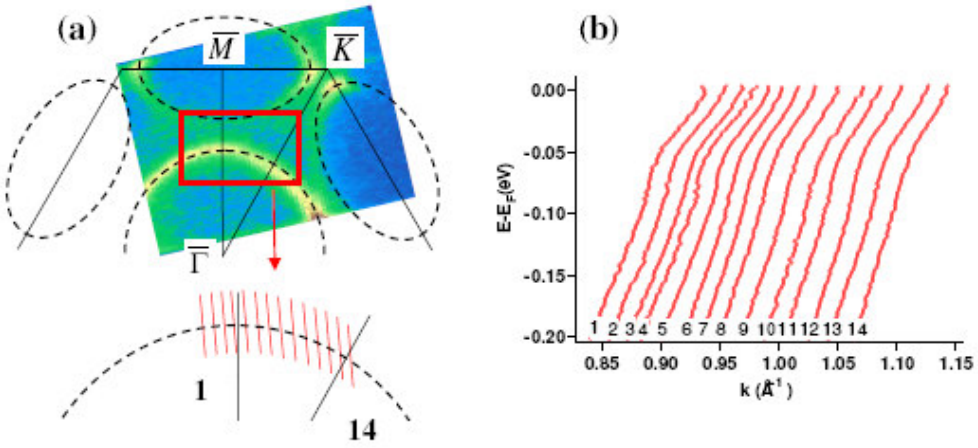

Figure 4.1. *(a) (Top panel): The Fermi surface mapping plotted with corresponding first SBZ. (Bottom panel): The 14 measurements and (b) the measured dispersions.*

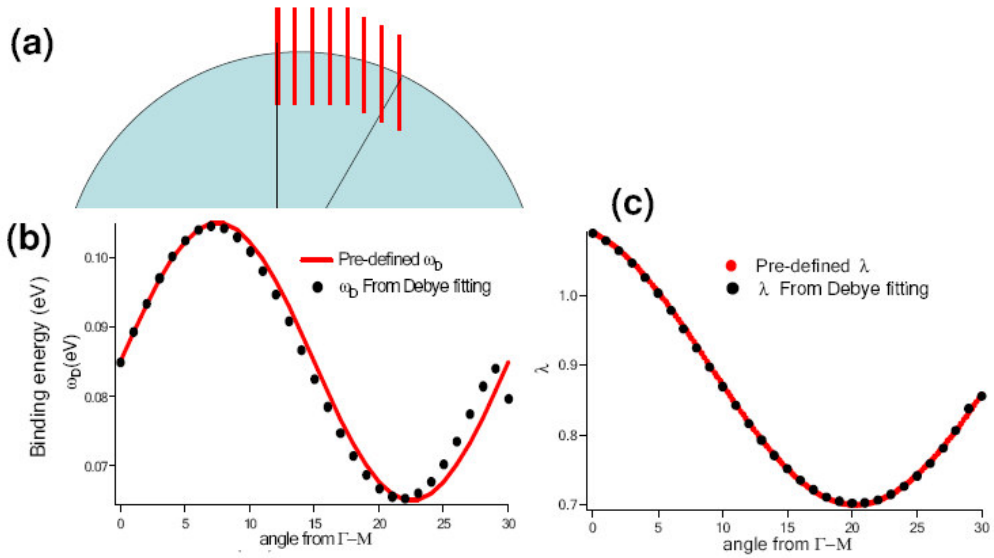

Figure 4.2. *Simulation test for the effects from the non-radial measurements.*

included in the error bar in figure 4.5. This error bar has a monotonic increase behavior when the off-radial cut angle increases.

Dispersion curves along the different cuts were determined by fitting the peak positions of the MDCs with a Lorentz function. The result is shown in figure 4.1 (b). Each curve displays a “kink”-like behavior that is the signature of the EPC renormalization of the bare particle dispersion [2–7, 10, 17–22, 24–26]. A qualitative examination of figure 4.1 (b) indicates that the kink positions in all the dispersion curves occur at about the same energy, ~60 meV, agreeing with the results in the literature [17–21].

For a more detailed analysis, the complex self-energy, Σ associated with the EPC has to be extracted from the experimental data. The real part of the self-energy, $\mathrm{Re}\Sigma$, is given by the re-normalization of the band, i.e., by the deviation of the actual dispersion from the so-called bare particle dispersion, which would be observed in the absence of EPC [26]. It is assumed that the bare dispersion has a simple quadratic shape. The imaginary part of the self-energy, $\mathrm{Im}\Sigma$, can be obtained from the Lorentz linewidth of the MDCs. Furthermore, $\mathrm{Re}\Sigma$ and $\mathrm{Im}\Sigma$ are related by a Kramers-Kronig transformation. This relation is used here in order to find the bare dispersion—the bare dispersion is obtained from a fit to the data at high binding energies and at the Fermi level (i.e., in regions where $\mathrm{Re}\Sigma$ is small), with the boundary condition that the resulting $\mathrm{Re}\Sigma$ must be consistent with $\mathrm{Im}\Sigma$ [27, 28]. The final $\mathrm{Re}\Sigma$s for the 14 cuts are shown in figure 4.3. Substantial differences are seen between these curves; some are broader than the others, and different fine structures appear to be present despite the high noise level. For example, figure 4.4 shows the plot of $\mathrm{Re}\Sigma$ of measurements #5 and #7. It is obvious #7 is much wider than #5. This already indicates that the details of the EPC are not isotropic around the circular Fermi contour.

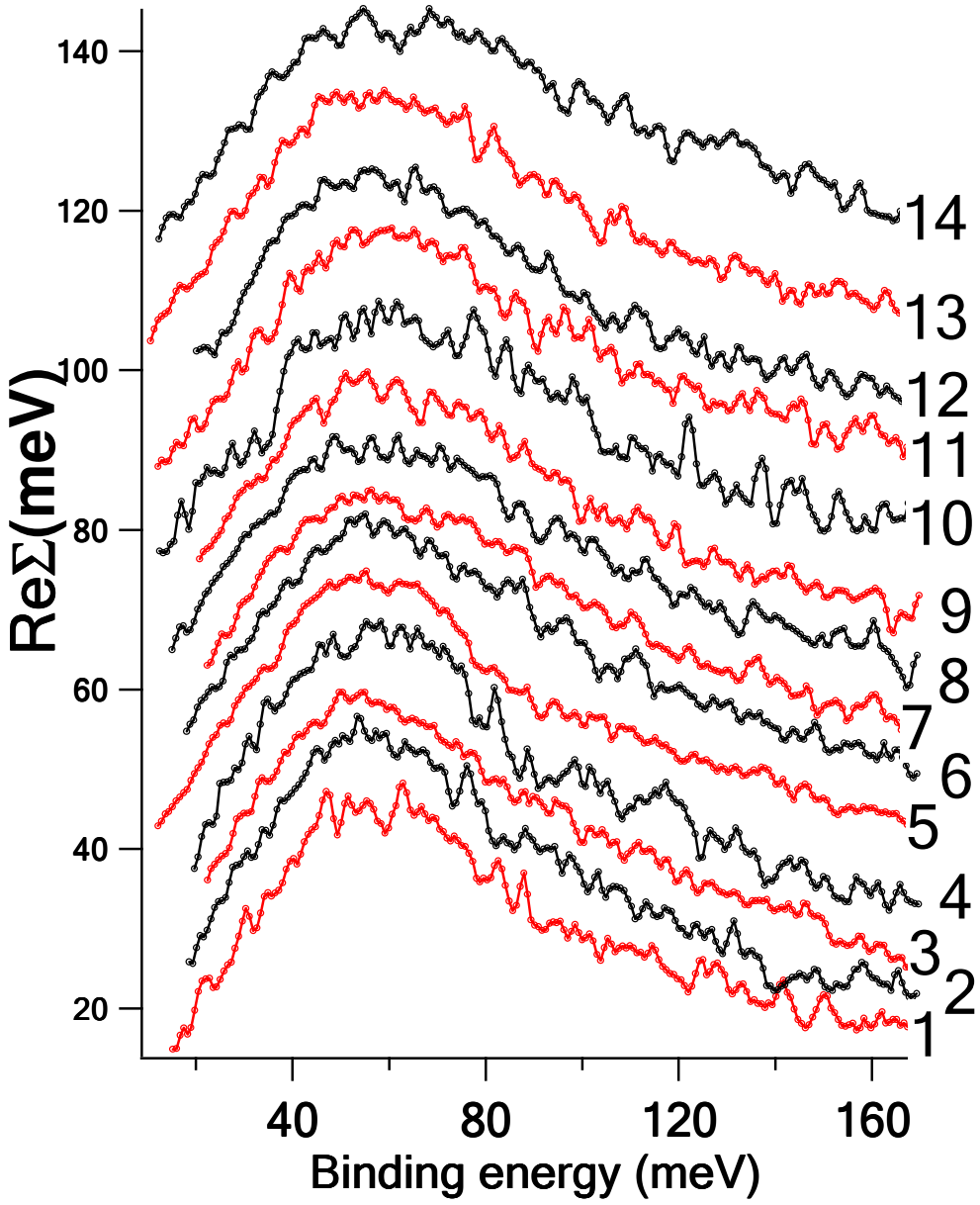

Figure 4.3. *Extracted* $\mathrm{Re}\,\Sigma$ *for the 14 measurements from figure 4.1 (b).*

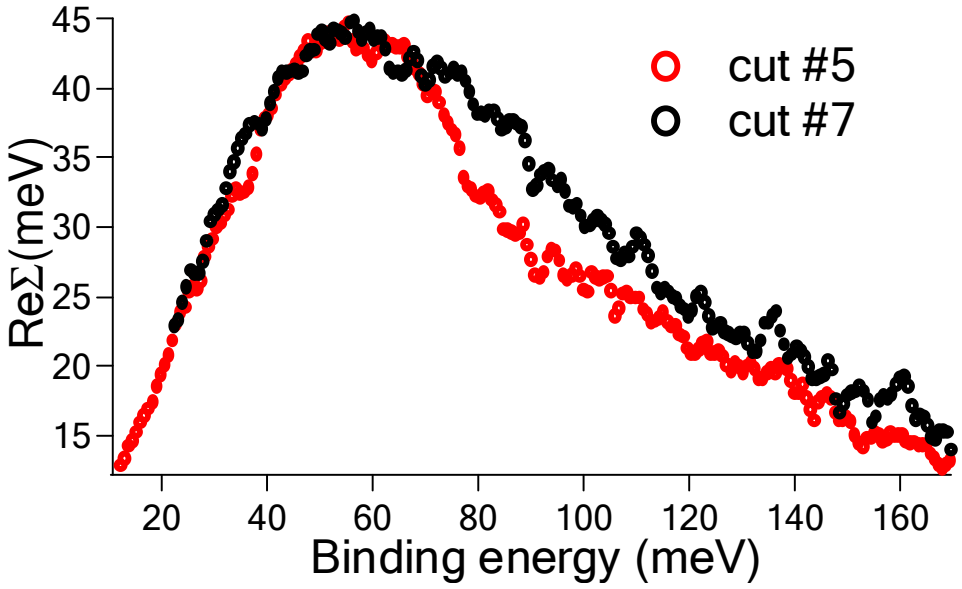

Figure 4.4. *Plot of* $\mathrm{Re}\Sigma$ *of measurements #5 and #7 mentioned in figure 4.1.*

The next step of the analysis is to extract the mass enhancement factor from the self-energy. As a consistency check and in order to evaluate the influence of the chosen approach on the result, three different methods were used:

(1) The most straightforward procedure is to determine λ from the slope of $\mathrm{Re}\Sigma$ at the Fermi energy. This slope method is based on the basic relationship between the mass enhancement factor and $\mathrm{Re}\Sigma$—Eq. (2-12). However, because this method suffers from the requirements of taking the derivative at zero energy and zero temperature, great care needs to be used when applying it. First, the measured dispersion near the Fermi energy can be distorted due to the finite energy resolution, and this may affect the resulting $\mathrm{Re}\Sigma$ and λ [26]. Second, the finite temperature will reduce the slope of $\mathrm{Re}\Sigma$ near the Fermi energy [22], leading to a systematic underestimate of λ. In the present case of Be(0001), neither restriction poses a severe problem because of the relatively high resolution and low temperature, compared to the Debye temperature of ~1000 K. Hence, the slope method provides a simple and valuable test here.

(2) The most fundamental function for the description of the EPC is the Eliashberg coupling function, $\alpha^2F(\omega)$, which is related to the phonon density of states and the coupling strength [25, 26, 29]. All other quantities of interest, including Σ and λ, can be derived from $\alpha^2F(\omega)$. A common approach to determine λ is to assume a simple model for $\alpha^2F(\omega)$, calculate $\mathrm{Re}\Sigma$, and compare it to the experimental result. In such a procedure, λ has the role of a fitting parameter. More precisely, one calculates $\mathrm{Re}\Sigma$ by Eq. (2-10). For $\alpha^2F(\omega)$, one commonly uses a two- or three-dimensional Einstein or Debye model. Since Be(0001) $\overline{\Gamma}$ surface is a 2D system, here, a

two-dimensional Debye model, for which $\alpha^2 F(\omega) = \lambda \frac{\omega}{2\omega_D}$, where ω_D is the Debye frequency of the phonon mode that couples to the electrons, is used. The shortcomings of this approach are the fact that the model for $\alpha^2 F(\omega)$ is largely arbitrary and closely related and that essential model parameters such as the Debye or Einstein temperatures are unknown. In the following, this method of obtaining λ is referred to as the Debye method.

(3) The Eliashberg function can also be extracted directly from the measured $\mathrm{Re}\,\Sigma$ by an integral inversion using the maximum entropy method (MEM) [25]. Once the Eliashberg function is extracted, the mass enhancement factor can be deduced from Eq. (2-8) [25, 26, 29].

Results and Discussion

Figure 4.5 shows the resulting mass enhancement factors extracted from the data presented in figure 4.3 using the MEM (solid squares), slope method (solid triangles), and Debye method (crosses). The dashed line is a guide to the eye for the MEM results. The results of all three models qualitatively agree with an anisotropic EPC scenario. It is clear that the mass enhancement is anisotropic in *k*-space and even the absolute differences between the three methods are mostly small. The mass enhancement factor has a global maximum in the $\overline{\Gamma} \rightarrow \overline{M}$ direction (~1.1 from MEM) and a local maximum in the $\overline{\Gamma} \rightarrow \overline{K}$ direction (~0.9 from MEM). The minimum of the mass enhancement factor appears ~10° away from the $\overline{\Gamma} \rightarrow \overline{K}$ direction (~0.6 from MEM). The values extracted using the Debye model are, on average, ~0.1 larger than the values obtained from MEM. The values using the slope method are similar to the values from MEM.

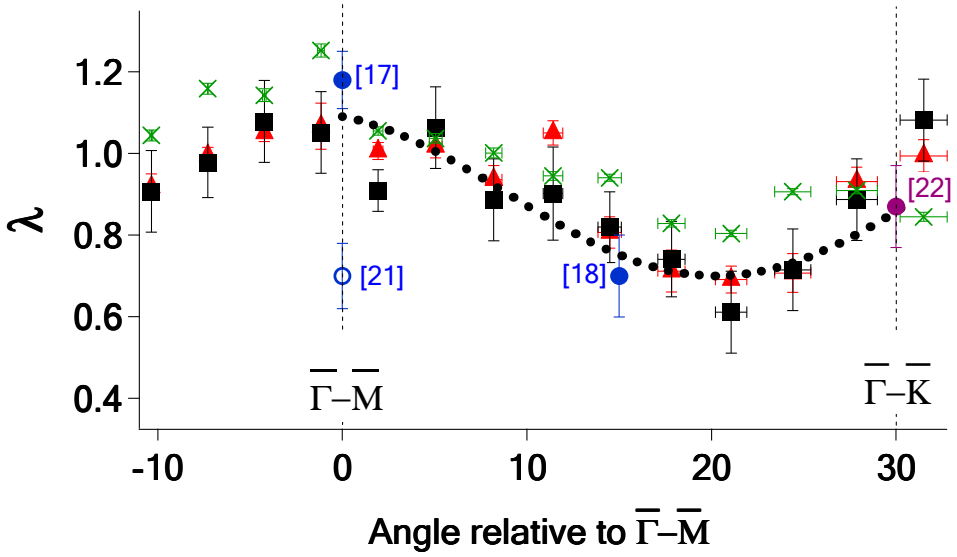

Figure 4.5. *Extracted mass enhancement factors from MEM (solid squares); from the slope method (solid triangles); and 2D Debye model fitting (crosses). Numbers are the reference numbers for the values from the literature, which are indicated as circles (solid circles indicate good agreement, and hollow ones indicate disagreement.*

The most important result of figure 4.5 is that the EPC is indeed anisotropic. While a different choice of extraction method can have a considerable influence on the resulting λ in a given direction, the application of any method on the entire data set gives qualitatively the same anisotropy. Note, however, that the aforementioned restrictions for the slope method and the approach using a Debye model still apply, and it is believed that the MEM result is the most reliable, in general.

A fundamental drawback when using a simple Debye or Einstein model for $\alpha^2F(\omega)$ is that it cannot capture the complexity of $\alpha^2F(\omega)$, leading to uncertainties in the determination of λ. This is illustrated in figure 4.6, which shows the experimental $\mathrm{Re}\Sigma$ and models for the 14^{th} cut, where a noticeable difference exists between the λ deduced from the slope method, the MEM approach, and the Debye model (see figure 4.5). The experimental $\mathrm{Re}\Sigma$ contains at least two major peaks, one in the 40–50 meV range and the other at ~70 meV, but $\mathrm{Re}\Sigma$ in a Debye model has only a single maximum. An optimized fit of the whole curve with a single Debye frequency requires a Debye frequency higher than the dominant low-energy mode in the data. The unavoidable consequence is a reduction of the slope of the fitted $\mathrm{Re}\Sigma$ at the Fermi energy and thus of the λ value evaluated from this method.

The MEM procedure, on the other hand, is constructed such that it can fit the whole $\mathrm{Re}\Sigma$ curve, as seen in figure 4.6. In particular, it always results in a good fit for the important low-energy region, even in the case of a complicated structure in $\alpha^2F(\omega)$ at higher energies. In the present case, one might get the impression that the MEM approach is just a more sophisticated version of the slope method, but this is incorrect—the MEM approach to determining λ is not restricted to low temperatures (compared with the Debye temperature) because it determines the (temperature-independent) Eliashberg function rather than the

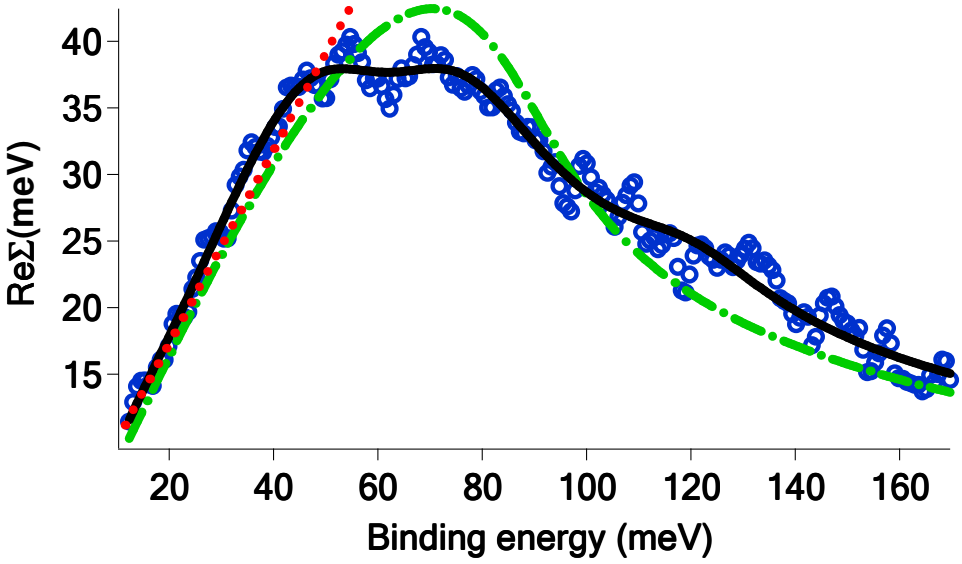

Figure 4.6. *Fittings from the MEM, slope, and 2D Debye model. Open circles are from data cut #14. The solid line is from MEM; the dashed-dot line is for the 2D Debye method, and the dot line is for the slope method.*

(temperature-dependent) self-energy. Indeed, λ is extracted using Eq. (2-8) which is independent of the temperature. Ideally, one would like to determine the fine structure in the Eliashberg function in order to infer which particular phonon modes are involved in the EPC on a specific point of the Fermi contour. Unfortunately, the signal to noise ratio in our experiment is too low for a reliable determination of such fine structure. The mass enhancement, on the other hand, is very robust against the noise [27].

Finally, we compare our results with the published EPC strengths for different points on the Fermi surface. The previously reported values of λ are included in figure 4.5 as circles. The number inside the circle refers to the number of the paper in the reference list here. Note that Ref. [22] is a theoretical value which is included for completeness. Overall, earlier experimental findings agree reasonably well with our results. A notable exception is the data point from Ref. [21] which reports a λ which is too low to be reconciled with our results. Our own tests done in the present work as well as a re-analysis of the data of Ref. [21] suggest that this small value of λ is caused by oxygen contamination. Figure 4.7 (a) shows the normal emission spectrum for samples with and without oxygen. Figure 4.7 (b) shows the corresponding $\mathrm{Re}\Sigma$. In figure 4.7 (a), the Fermi energy locates at around 27.5 eV, where a clear Fermi step is seen. The sharp peak with binding energy about 2.8 eV originates from the surface state; while a broad peak with binding energy around 10 eV are from the projected bulk band. The oxygen peak locates around 6-8 eV. Due to the high cross section of the oxygen peak compared to the surface state peak, a small oxygen contamination can induce a huge peak. The small hump appeared in figure 4.7 (a) indicates a tiny amount of oxygen appeared on the surface. It is clear that the tiny oxygen contamination indeed would reduce the EPC on the surface. The data point from Ref. [17] reporting a value of λ = 1.18 in the $\overline{\Gamma} \rightarrow \overline{M}$ direction agrees very well

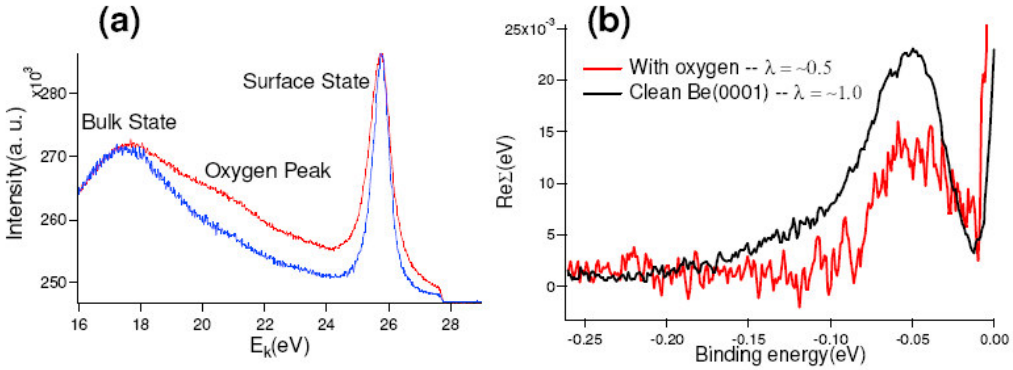

Figure 4.7. *(a) Normal emission spectra for samples with and without oxygen. (b) Corresponding* $\mathrm{Re}\,\Sigma$.

with our results. The same group remarked in a later paper [20] that no significant differences could be observed between the $\overline{\Gamma} \to \overline{M}$ and the $\overline{\Gamma} \to \overline{K}$ directions, such that it can be concluded that λ should be similar in that direction, again in good agreement with our results. Indeed, given the λ maxima of similar height along $\overline{\Gamma} \to \overline{M}$ and $\overline{\Gamma} \to \overline{K}$, no indications of anisotropy can be expected in a study confined to these two directions. The theoretical value of Ref. [22] is consistent with the strong coupling reported by the experimental papers, but published information about a possible anisotropy is lacking thus far. On the whole, our data agree well with previous results, but it has not been possible so far to detect the anisotropy because a larger data set is needed and it has to be combined with a consistent approach to data analysis.

Inconsistence of Theoretical Results

There are groups working on the theoretical part of this question. Unfortunately, no any published paper concluded the anisotropy EPC on Be(0001) surface state. A. Eiguren et al. reported an LDA slab calculation on Be(0001) surface [22]. In Ref. [22], the Eliasherg functions were carried out at Fermi energy and bottom of the band, without concerning the k dependent. Thereafter, this research group put efforts on the calculation of the k-dependent EPC. Figure 3.3 top panels of (a) and (b) are calculated by them. The mass enhancement factors along $\overline{\Gamma} - \overline{M}$ and $\overline{\Gamma} - \overline{K}$ are 1.1 and 0.48, respectively, which is inconsistent to what we observed experimentally. Our observation drove them to check their calculations, but no successful results are obtained at present time. It is also pointed out from Ref. [30], the LDA failed to reproduce the phonon dispersion of graphene, which is attributed to the failure capture of the EPC in the calculation [30]. In order to calculate the EPC on Be(0001) surface, the improvement on LDA might be essential.

Summary

What is the explanation for an anisotropic EPC in Be when the $\overline{\Gamma}$ surface state looks like a 2D free electron band? The answer has to be in the anisotropic nature of the surface phonon dispersion [13] or in the strong momentum dependence in the matrix element which is in essence the same physics [31]. In order to gain a more detailed understanding of the anisotropy, similar data as here with considerably better statistics would be needed. This would permit extraction of the momentum-dependent Eliashberg function with a reliable fine structure, such that the varying coupling strength could be related to the corresponding phonon modes and/or the variation in the matrix elements. A comparison to the calculated momentum-dependent Eliashberg functions would be extremely valuable here. In conclusion, our work shows that electron-boson coupling can be anisotropic even in a simple system with an isotropic Fermi surface. This result can be useful for the understanding of much more complex systems such as the high-T_c cuprates.

Chapter V
Extracting the Eliashberg Function

Eliashberg Function

From the theoretical point of view, the Hamiltonian of the EPC can be written by Eq. (2-1) with the bare and interacting part of the Hamiltonian, Eq. (2-2) and Eq. (2-3), respectively. With the Hamiltonian, the transition probability from the initial state with *N* electrons in the system to the final state can be expressed as Eq. (2-4). In many applications, it is more interesting to know the scattering rate from a state at $\vec{k}$ with energy $E_{\vec{k}}$ to all other final states with energy $E_{\vec{k}} \pm \hbar\omega$, summing all possible states. The definition of the coupling function considering the scattering with respect to the energy, which is called the Eliashberg function (ELF), is shown in Eq. (2-5). This function gives the EPC between an initial state on the Fermi surface S_F and all other states $\vec{k}'$ on S_F which differ in energy from the initial state by $\hbar\omega$. Often, the average of Eq. (2-5) over all $\vec{k}$ on S_F is called the Eliashberg coupling function and is defined as Eq. (2-6). Hence, with the Eliashberg coupling function, the McMillan-Hopfield parameter, η [Eq. (2-7)], the mass enhancement factor, λ (Eq. (2-8)), and the average phonon frequency, $\omega_{\log}$ [Eq. (2-9)], can be obtained.

Furthermore, the real and the imaginary parts of the self-energy of the quasiparticles can also be obtained from the Eliashberg function. Instead of describing the complex equation of the many-body interacting equation, the concept of “quasiparticle” is used to describe the complex system. The quasiparticle is a group of single particles coupled with the system. The quasiparticle idea originates from Lev Landau’s Fermi liquid theory, which was originally invented for studying liquid helium-3. In other

words, the quasiparticle idea was invented for studying many-body systems, where particle interactions cannot be neglected. The self-energy is the contribution to the particle's energy due to the interaction between the single particles and the system. The contribution to the particle's energy would also enhance the effective mass of the particle itself. More precisely, the self-energy is the renormalized part of the quasiparticle's energy due to the interaction. The renormalized energy results in a change of the effective mass of the quasiparticle. The quasiparticles are also called "dressed" particles with the reason being that because of the interaction, the quasiparticles look dressed and thus have a higher mass (effective mass). In contrast, the particles without interaction are called "bare" particles.

To quantitatively understand the many-body interaction, ELF is the key. As mentioned in Chapter II, theoretically, any quantity related to EPC can be deduced from the ELF. Though the ELF was constructed from the scenario of EPC, it can extend to the more general case—the EBC. For the systems with strong-coupling BCS-type superconductors, such as Pb, Hg, or Nb_3Ge, the prediction is deviated from BCS theory [1]. The reason is the original BCS theory only can handle weak coupling cases. For the strong coupling superconductors, the theoretical approach is based on the Eliashberg equations [2], which is an extension of the BCS theory. For example, it is proved in ARPES data that the kink of the dispersion of Pb(110) surface can be described very well through Eliashberg equations [3]. Figure 5.1 shows the (a) real and the (b) imaginary parts of the self energies as function of binding energy; and (c) the imaginary part of the self energy as function of temperature. The dots are the experimental data; while the lines are calculated from the Eliashberg equations. In this case, the Pb(110) is a strong coupling system with the mass enhancement factor, λ, to be 1.55.

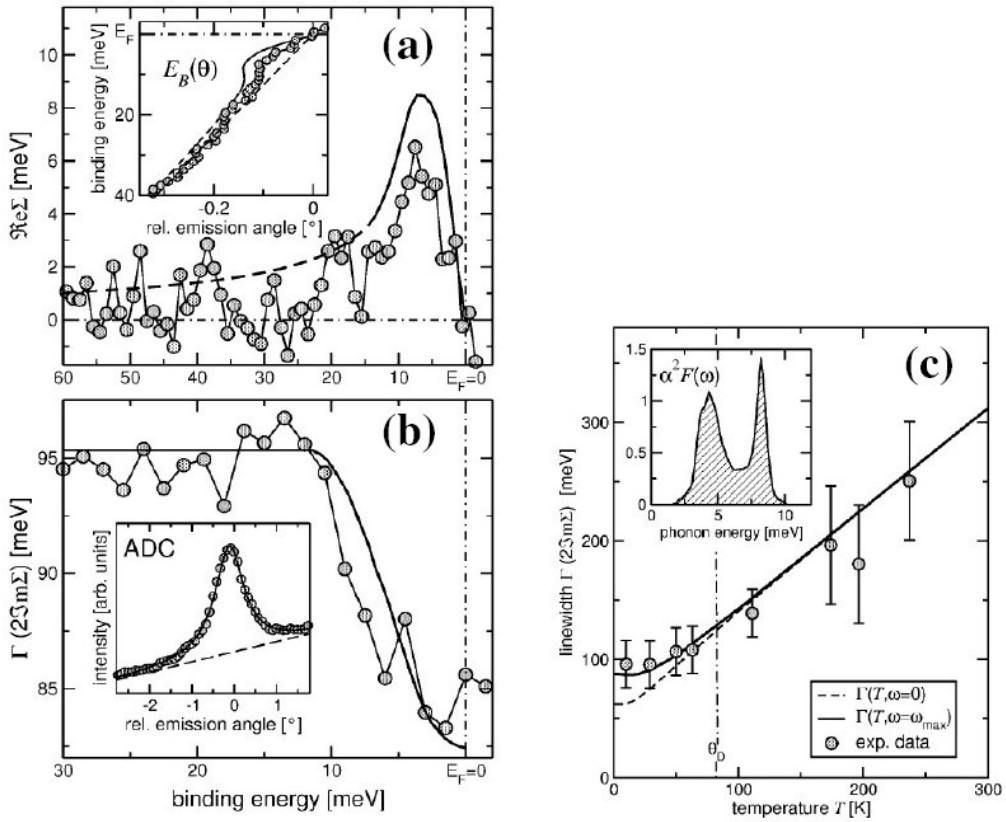

Figure 5.1. *(a)The real part of the self energy from the ARPES experiment of Pb(110) surface; (b) The imaginary part of the self energy from the ARPES experiment of Pb(110) surface; (c) The temperature dependent lifetime width. (Ref. [3]).*

Extraction of the Eliashberg Function

Experimentally, it is possible to extract the ELF. The idea originates from the relationship between the ELF and the self-energy, both the real part [Eq. (2-10)] and the imaginary part [Eq. (2-11)]. As discussed in Chapter II, the real part and the imaginary part of the self-energies can be extracted from experiments using angle-resolved photoemission spectroscopy (ARPES). The real part of the self-energy can be extracted from the energy difference between the extracted dispersion with a kink and the bare dispersion, which is usually a simple polynomial form. The imaginary part of the self-energy can be obtained by converting the widths of the MDCs through Eq. (2-22). It is obvious from Eq. (2-10) and Eq. (2-11) that the real and imaginary parts of the self-energies can be calculated by integration from the ELF. Hence, in principle, ELF can be extracted by performing the integral inversion from either the real part or the imaginary part of the self energies. However, it is well-known that the real part of the self-energy always has a smaller error bar than the imaginary part has. Therefore, it is more likely that the real part of the self-energy could be used to extract the ELF.

J. Shi *et al.* have shown that extraction of the ELF can be achieved by performing the integral inversion of the real part of the self-energy, obtained from the ARPES experiments [4]. However, the extraction is non-trivial. According to J. Shi's paper [4], the integral inversion is very sensitive to the noise. The noise will result in a numerically unstable situation. To overcome this problem, J. Shi *et al.* adopted a method called the maximum entropy method (MEM) [4]. In MEM, a constraint function is used. The constraint function is used to restrict the resulting ELF to be physically reasonable. The details of the constraint function will be discussed later.

Conventionally, to complete the integral inversion, the most straightforward way is to use the least-squares method, which minimizes

$$\chi^2 = \sum_{i=1}^{N_D} \frac{[D_i - f(\varepsilon_i)]^2}{\sigma_i^2} \tag{5-1}$$

where D_i are the data points; $f(\varepsilon_i)$ is the fitting function; σ_i are the error bars of the data points; and N_D is the number of the data points. However, this method fails when it is used to do the integral inversion for the ELF from $\mathrm{Re}\Sigma$ [Eq. (2-10)]. The reason is that the direct inversion would tend to exponentially amplify the high-frequency noise appearing in the raw data. In other words, the noise in the data would result in unphysical fluctuations and negative values in the extracted ELF. To avoid this numerically unstable problem, J. Shi *et al.* proposed to minimize the following functional, instead of the least-squares functional, as indicated in Eq. (5-1):

$$L = \frac{\chi^2}{2} - aS \tag{5-2}$$

where χ^2 is defined as Eq. (5-1); *a* is a multiplier which controls how close the fitting should follow the data while not violating the physical constraint; and *S* is the generalized Shannon-Jaynes entropy, which is defined as:

$$S = \int_0^\infty d\omega \left[\alpha^2 F(\omega) - m(\omega) - \alpha^2 F(\omega) \ln \frac{\alpha^2 F(\omega)}{m(\omega)} \right] \tag{5-3}$$

This entropy term imposes physical constraints on the fitting and is maximized when $\alpha^2 F(\omega) = m(\omega)$. The constraint function, $m(\omega)$, has some physical restrictions for the ELF, such as (1) it is an all-positive function, and (2) it vanishes at $\omega \to \infty$ and above a maximal phonon frequency. With this method, it is possible to be extract the ELF.

To extract the ELF, the following procedure is used. First, with the ARPES energy-momentum measurements, one can obtain the energy-momentum dispersion after the MDCs analysis. For example, figure 5.2 (a) shows a series of MDCs with different binding energies along with a

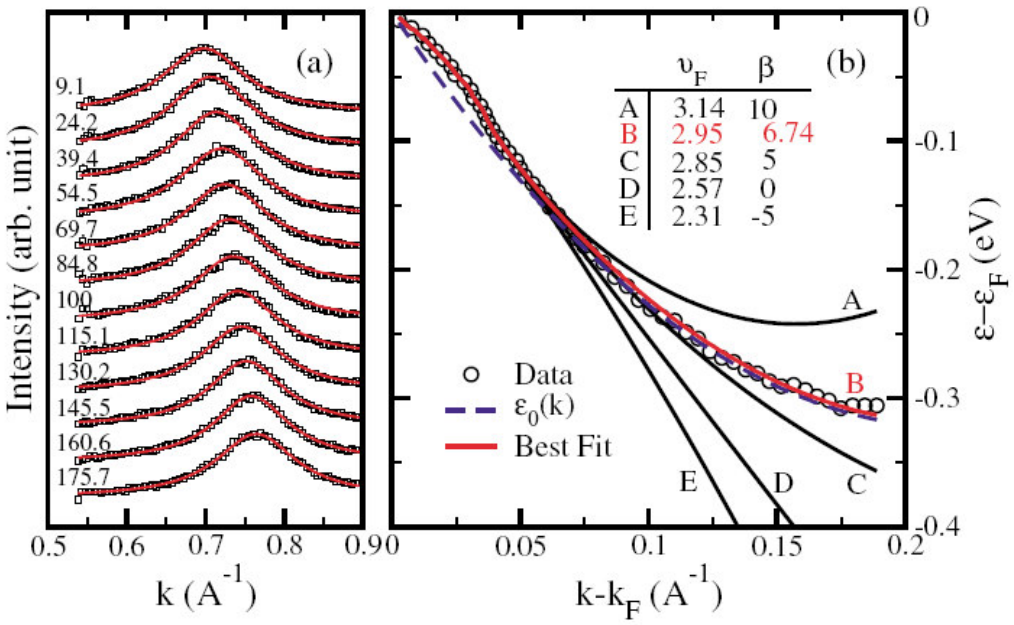

Figure 5.2. *(a) MDCs with different binding energies as well as the fitting to the curves. (b) Energy-momentum dispersion relation constructed by the resulting peak positions of the MDCs. The data here are measured on Be(10$\bar{1}$0) surface state. (Ref. [4]).*

Lorentz function fitting for the surface state on Be(10$\bar{1}$0) [4]. The resulting peak positions obtained from the fitting of the MDCs can construct the energy-momentum dispersion relation, as shown in figure 5.2 (b) [4]. After subtracting the bare dispersion from the experimental dispersion, the $\mathrm{Re}\Sigma$ can be obtained. However, because it is impossible to measure the bare dispersion, the conventional way is to assume a straight line or a quadratic line to approximate the bare dispersion. In the MEM code, the quadratic form is used. Thus, $\mathrm{Re}\Sigma$ of the Be(10$\bar{1}$0) surface state is obtained and shown in figure 5.3. Then, the integral inversion is used to extract the ELF. The extracted ELF of the Be(10$\bar{1}$0) surface state is also shown in figure 5.3 [4].

Unfortunately, as mentioned in Chapter III, the extraction is affected by many limitations. For example, the energy resolution of the instrument will distort the $\mathrm{Re}\Sigma$ near the Fermi energy and near the kink. This will make the integral inversion unreal due to the distorted $\mathrm{Re}\Sigma$. To solve this problem, a procedure to discard the distorted data is proposed. Further, the energy resolution would also smear the fine structure of the $\mathrm{Re}\Sigma$. This will also smear the extracted ELF. In Chapter II, we have already proven that the extracted ELF agrees very well with the smeared ELF. To overcome this problem, the only way is to improve the energy resolution when doing experiments. More importantly, the noise is found to have a surprising influence on the extracted results. As mentioned above, the integral inversion is very sensitive to the noise. Even when the MEM is applied to avoid the numerically unstable problem, the peaks that appeared in the extracted ELF are still following the appearance of the noise in the $\mathrm{Re}\Sigma$. In other words, wherever a tiny jump appeared in $\mathrm{Re}\Sigma$ due to the noise, there would also be a peak in the extracted ELF. To overcome this problem experimentally, it is essential that quasi-noise-free data with very good energy resolution be collected. With good energy resolution, the distortion would be minimized. With the low noise level, the

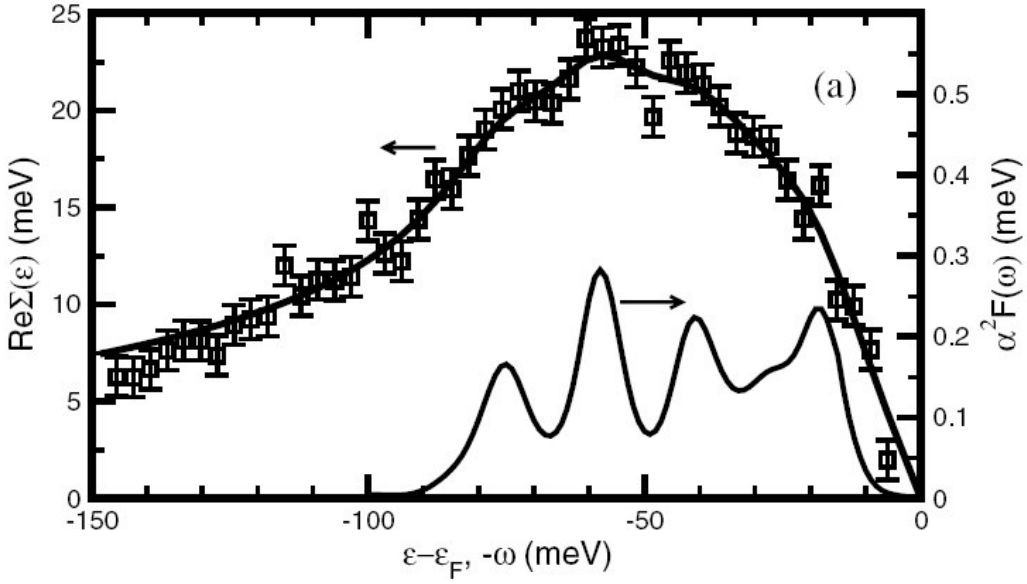

Figure 5.3. $\mathrm{Re}\Sigma$ *obtained from the dispersion in figure 5.2 and the corresponding extracted ELF of Be(10*$\bar{1}$*0) surface state. . (Ref. [4]).*

fine structure in $\mathrm{Re}\Sigma$ would dominate the peaks that appeared in the extracted ELF. In short, a very high quality data is required for extracting the ELF.

Experiment

The experiments were conducted at Beam Line 10.0.1 at the Advanced Light Source (ALS) at the Berkeley Lawrence National Laboratory (BLNL). The facility operates with a nominal energy of 1.9 GeV in the storage ring. The size of the electron beam in the storage ring is about 0.20 $\times$ 0.02 mm.

The base pressure of the preparation chamber was in the low 10^{-10} Torr range. Be(0001) single-crystal surfaces were cleaned by cycles of sputtering at an elevated temperature (450 $^{\circ}C$) for 30 min followed by a 15-min annealing at 500 $^{\circ}C$. In the sputtering procedure, Ar gas was used and kept at 8×10^{-6} Torr with a 1.5-keV beam energy. The sputtering beam was incident 45 degrees off normal to the surface. When annealing, the pressure was at low 10^{-9} Torr to high 10^{-10} Torr range. ARPES measurements were performed in the main chamber with a base pressure at a low 10^{-11} Torr range, in which the sample can kept clean up to more than one day, and were measured by a Scienta R4000. The photon energy was set to be the first harmonic at 32 eV with an U10 undulator. The orientation of the sample was determined by LEED and by the features in Fermi surface mapping. The angular resolution was better than 0.01 degree. The sample was cooled by liquid helium to ~8 K during the measurements. The energy resolution was kept at around 15 meV.

Extracting the Eliashberg Function from the Be(0001) $\overline{\Gamma}$ Surface State

Figure 5.4 shows two repeated measurements of high-quality ARPES energy-angle mappings of the Be(0001) $\overline{\Gamma}$ surface state along the $\overline{\Gamma}-\overline{M}$ direction. After MDC analyses, the energy-momentum dispersion relations are obtained, as shown in figure 5.5. The dispersions are shifted horizontally for easy comparison. The energy resolutions for these two scans are about 15 meV. As we learned in Chapter III, the energy resolution would distort the $\mathrm{Re}\Sigma$ near the Fermi energy. It can be seen that near the Fermi energy, the dispersion is distorted. After the bare dispersion is subtracted, $\mathrm{Re}\Sigma$ is extracted, as shown in figure 5.6 (a). The $\mathrm{Re}\Sigma$ are shifted vertically for easier observation. From figure 5.6 (a), the first observation is that Scan #1 has a higher noise level than Scan #2 has. Second, it can also be observed that the fine structures in both $\mathrm{Re}\Sigma$ are coincident to each other, except that the noise appeared in Scan #1. For comparison, we also did measurement along $\overline{\Gamma}-\overline{K}$ direction. The extracted $\mathrm{Re}\Sigma$ along both directions are plotted in figure 5.6 (b). It is observed that the noise level along $\overline{\Gamma}-\overline{K}$ is a little bit high, which prohibits us to extract reliable Eliashberg function. Another observation is the $\mathrm{Re}\Sigma$ along $\overline{\Gamma}-\overline{K}$ is broader than the $\mathrm{Re}\Sigma$ along $\overline{\Gamma}-\overline{M}$ direction. This is consistent with our previous observation in Chapter IV. Because Scan #2 has better quality, we did further analyses on Scan #2. Figure 5.7 shows the $\mathrm{Re}\Sigma$ along with the width of the MDCs as a function of the binding energy. The widths of the MDCs are directly correlated to the $\mathrm{Im}\Sigma$ through Eq. (2-22). The width increases abruptly when the binding increases and saturates with a constant value when the binding energy exceeds the maximum phonon energy. In the case of Be(0001), the maximum phonon energy is around 80 meV.

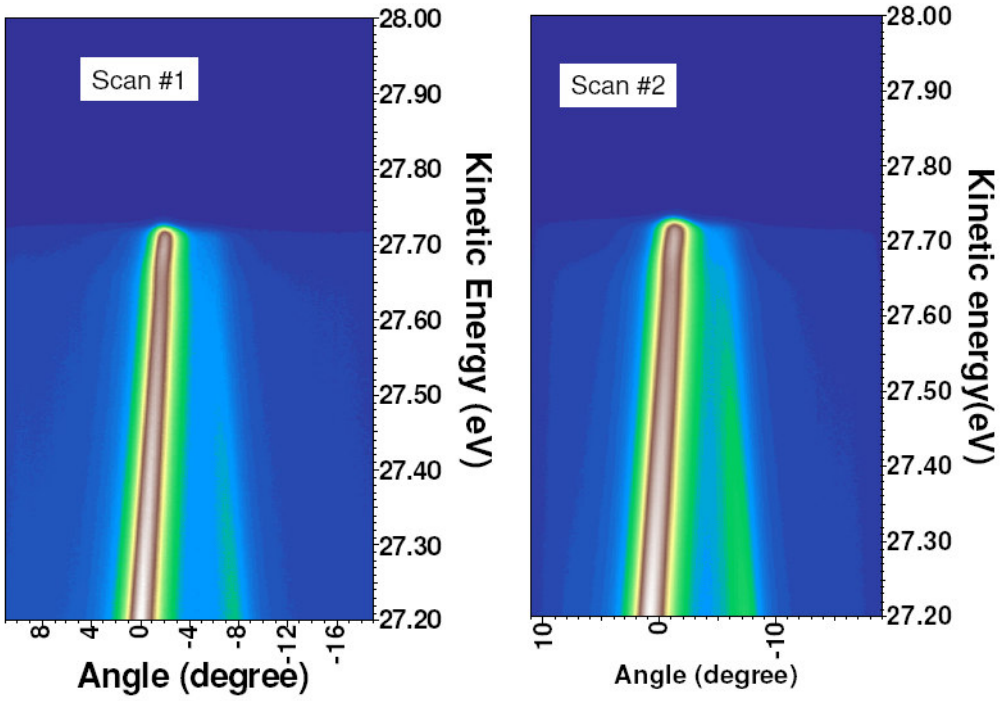

Figure 5.4. *Two repeated measurements of high-quality ARPES energy-angle mappings of the Be(0001)* $\overline{\Gamma}$ *surface state along the* $\overline{\Gamma} - \overline{M}$ *direction.*

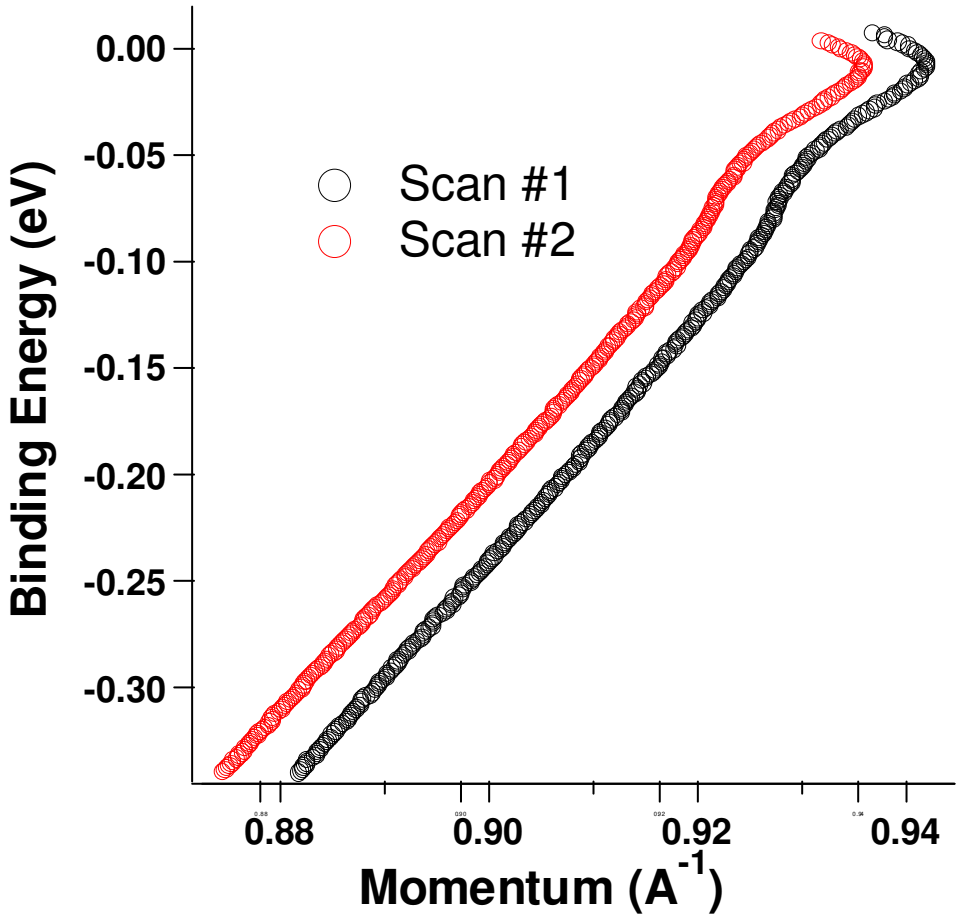

Figure 5.5. *Energy-momentum dispersions obtained by MDC fitting of the data shown in figure 5.4.*

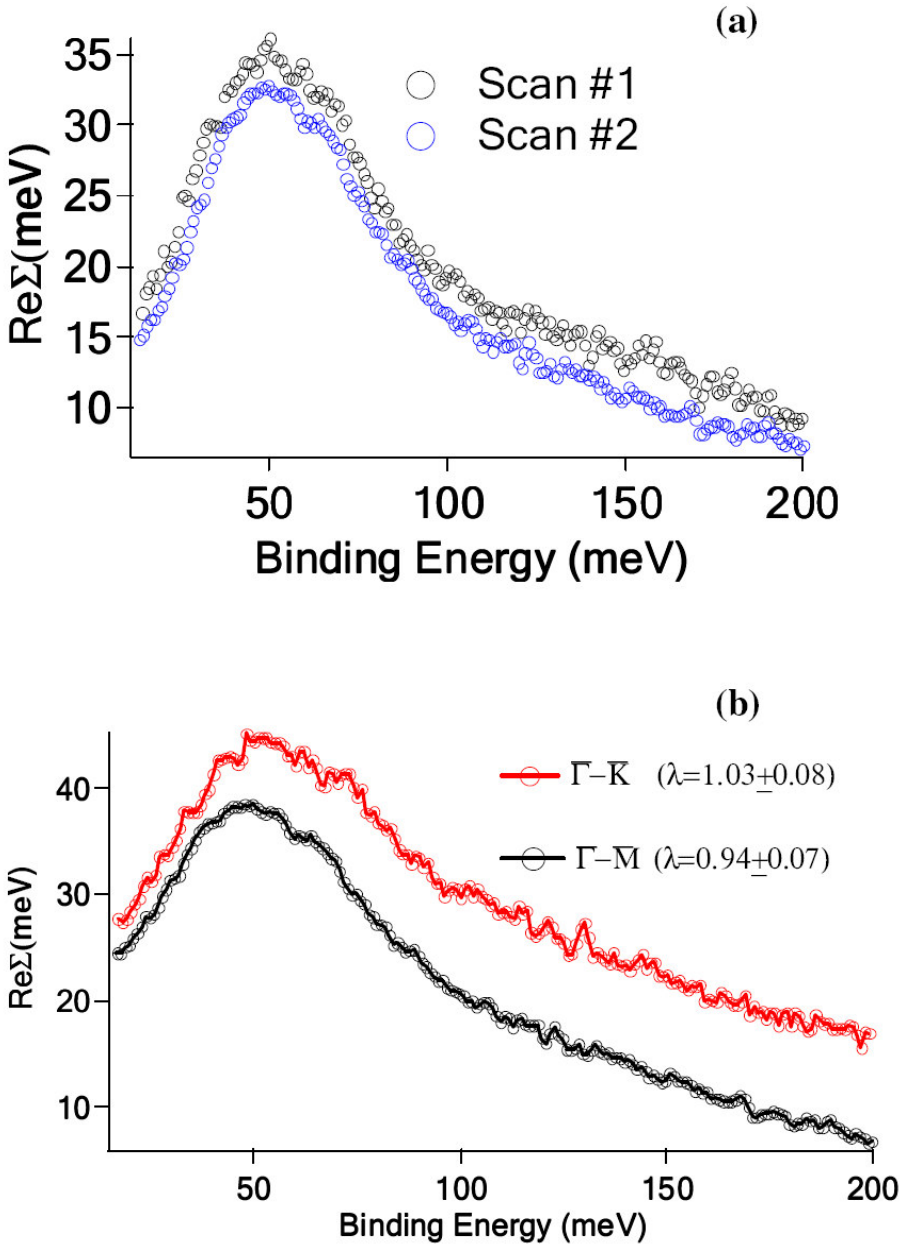

Figure 5.6. *(a) Extracted* $\mathrm{Re}\Sigma$ *from the dispersions in figure 5.5; (b) Comparison between the extracted* $\mathrm{Re}\Sigma$ *of* $\overline{\Gamma}-\overline{M}$ *(lower) and* $\overline{\Gamma}-\overline{K}$ *(upper) directions.*

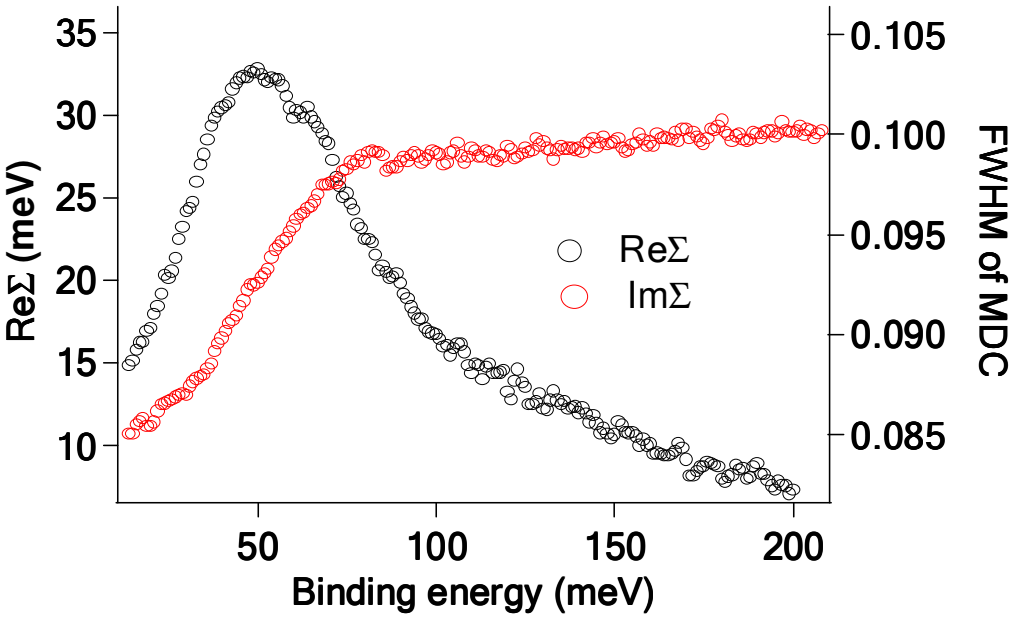

Figure 5.7. *Widths of the MDCs and* $\mathrm{Re}\Sigma$ *, along* $\overline{\Gamma}-\overline{M}$ *direction, extracted from Scan #2 in figure 5.6.*

After applying MEM, the ELF can be extracted, as shown in figure 5.8. For comparison, $\mathrm{Re}\Sigma$ and the widths of MDCs are also plotted in figure 5.8. There are 10 observable peaks in the extracted ELF with the binding energies at: (1) 23.5, (2) 29.5, (3) 37.5, (4) 44.5, (5) 49.0, (6) 55.5, (7) 64.5, (8) 68.5, (9) 75.5, and (10) 81.0 meV. From figure 5.8, one can observe that most of these peaks are coincident with the fine structures both in $\mathrm{Re}\Sigma$ and in the widths of the MDCs. This indicates that the extracted ELF should have correct peak information. Because the ELF is a coupling function describing how the electrons couple to the phonons, the phonon density of states (DOS) should play a major role in the coupling function. To further confirm the correctness of the extracted ELF, the bulk and surface phonon DOS are used for comparison. The bulk phonon DOS are shown in figure 1.1 [5, 6]. When plotted together with the extracted ELF in figure 5.9, we can see that peaks #6–#9 are associated with the bulk phonon. For the lower energy peaks, a comparison was made with the surface phonon dispersion, which is shown in figure 1.11 [7]. We re-plotted it in figure 5.10 with three line indications where peaks #3–#5 appeared in the extracted ELF. From figure 5.10, peaks #3–#5 seem to be correlated to the flat region of the surface phonon dispersion. The flat region in the dispersion will result in a high DOS. In other words, at this certain energy, there should be a peak in the DOS. From this viewpoint, it is logical to assign peaks #3–#5 to the related surface phonon. Those not-assigned peaks are more likely due to the noise in the data. For peak #1 and peak #2, the corresponding fine structures in $\mathrm{Re}\Sigma$ have relatively small widths, compared to the energy resolution—~15 meV. As indicated in Chapter II, the energy resolution would smear the fine structure in $\mathrm{Re}\Sigma$. Thus, the fine structure observed in $\mathrm{Re}\Sigma$ should not have a smaller width than the energy resolution. Therefore, peak #1 and peak #2 are more likely to be due to the noise in the data. For peak #10, it seems to be just a shoulder of peak #9.

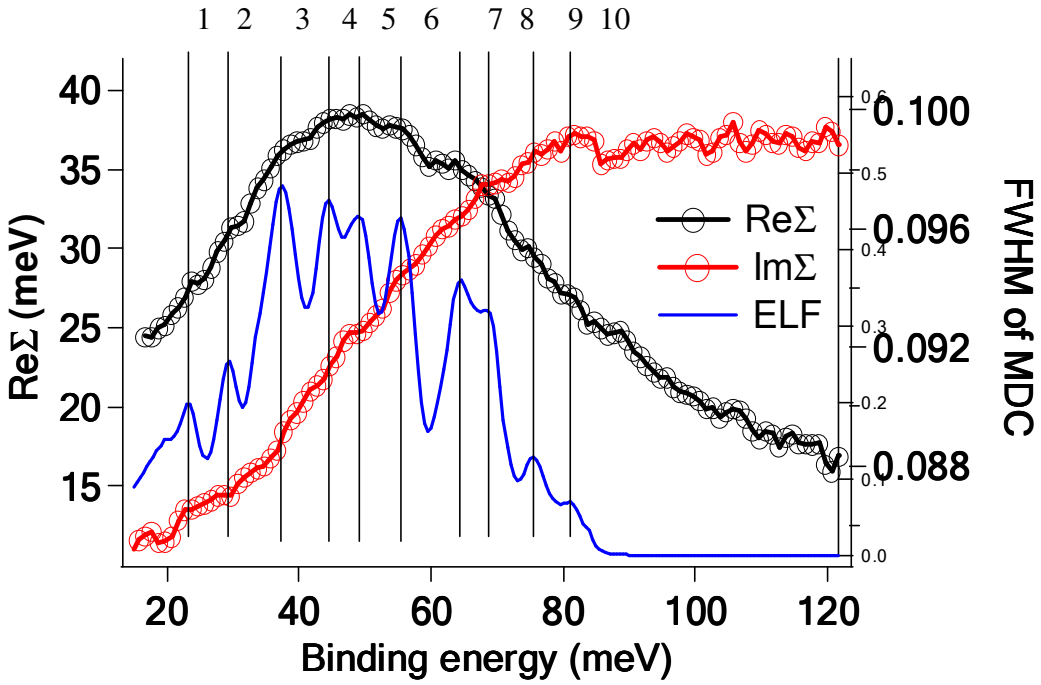

Figure 5.8. *Extracted ELF, widths of the MDCs, and* $\mathrm{Re}\,\Sigma$*, along* $\overline{\Gamma}-\overline{M}$ *direction, extracted from Scan #2 in figure 5.6.*

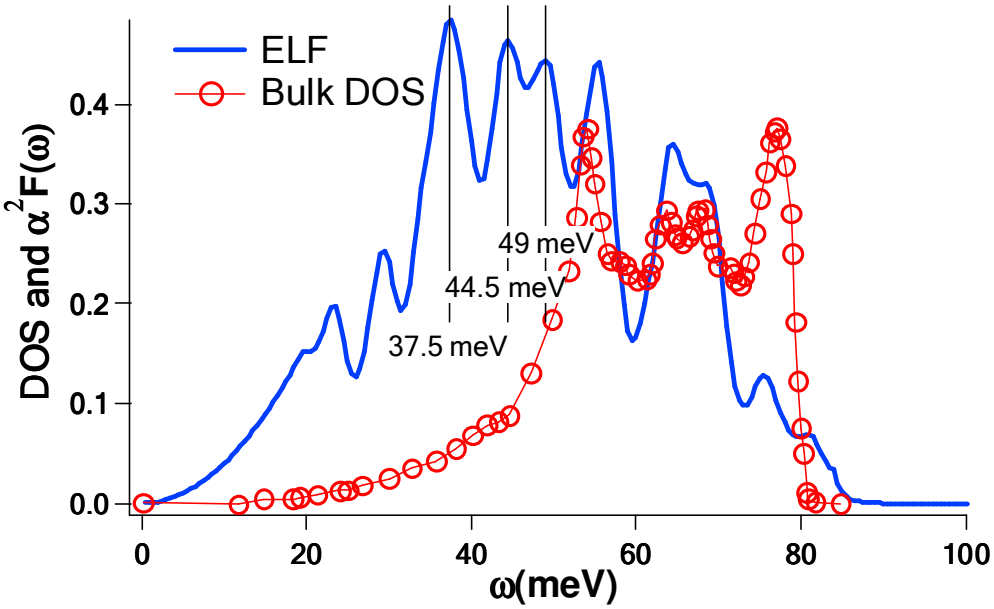

Figure 5.9. *Extracted Eliashberg function and beryllium bulk phonon density of states [5, 6].*

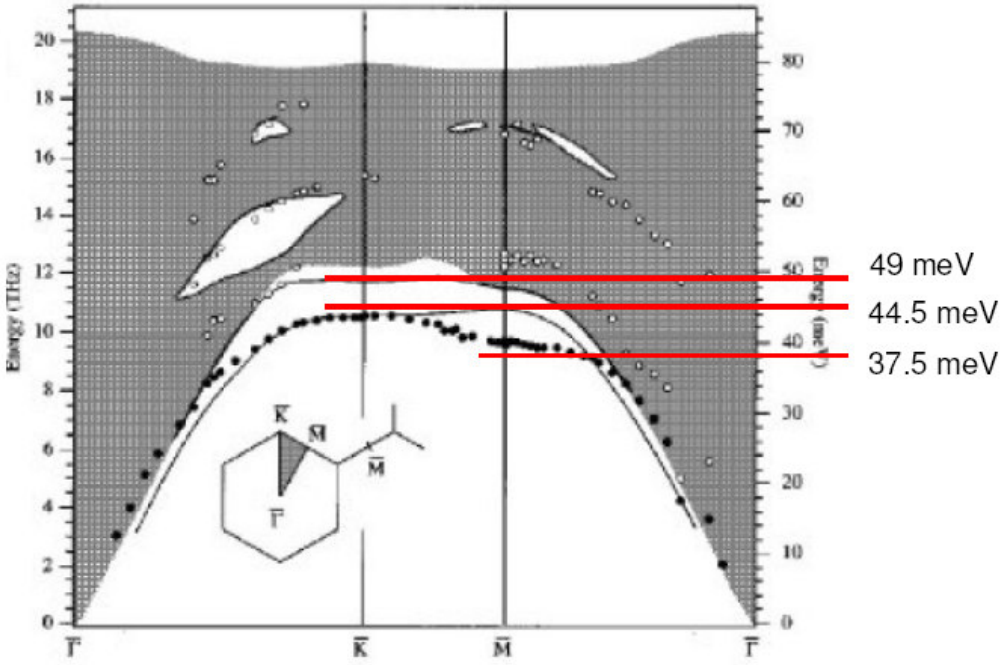

Figure 5.10. *Surface phonon dispersion measured by electron energy loss spectroscopy [7]. Horizontal lines indicate the peaks position of the extracted Eliashberg function shown in figure 5.9.*

Once the ELF is extracted, we can use it to calculate the mass enhancement factor from Eq. (2-8). From the argument above, we know that the contribution from the bulk phonon is mainly located at higher energies; while the contribution from the surface phonon is mainly located at lower energies. Instead of just calculating the value of mass enhancement factor, we calculated the accumulated value of the mass enhancement factor as a function of the energy:

$$\lambda(\omega) = 2\int_0^{\omega} \frac{\alpha^2 F(\omega')}{\omega'} d\omega' \qquad (5\text{-}4)$$

The result is plotted in figure 5.11 along with the ELF. First, because the bulk phonon has a limited contribution for energies lower than about 52 meV, we can conclude from figure 5.11 that the contribution from the surface phonon to the mass enhancement factor is about 0.72 out of the total value of 0.94. Compared with the total value of the mass enhancement factor, 0.94, it is about 77%. Furthermore, the difference between the total value (0.94) and the contribution from peaks lower than 52 meV (0.72) is about 0.22. This value is very close to the bulk mass enhancement factor – 0.24. In other words, in the Be(0001) $\overline{\Gamma}$ surface state along the $\overline{\Gamma} - \overline{M}$ direction, the surface phonon boost the mass enhancement factor dramatically. This dramatic influence from the surface phonon is responsible for the strong EPC on the Be(0001) surface and thus changing a weak coupling metal (Be) into a strong coupling surface.

As we mentioned in Chapter IV, the theoretical effort has not succeeded yet. Figure 5.12 shows the theoretical results from Chulkov's group and our experimental result. It is obvious that the agreement is very poor. The peaks in the Eliashberg function are not consistent and the resulting mass enhancement factor has twice difference. Figure 5.13 shows the resulting angle-dependent mass enhancement factors on Be(0001) surface from theoretical calculation. It is clear that the angle-

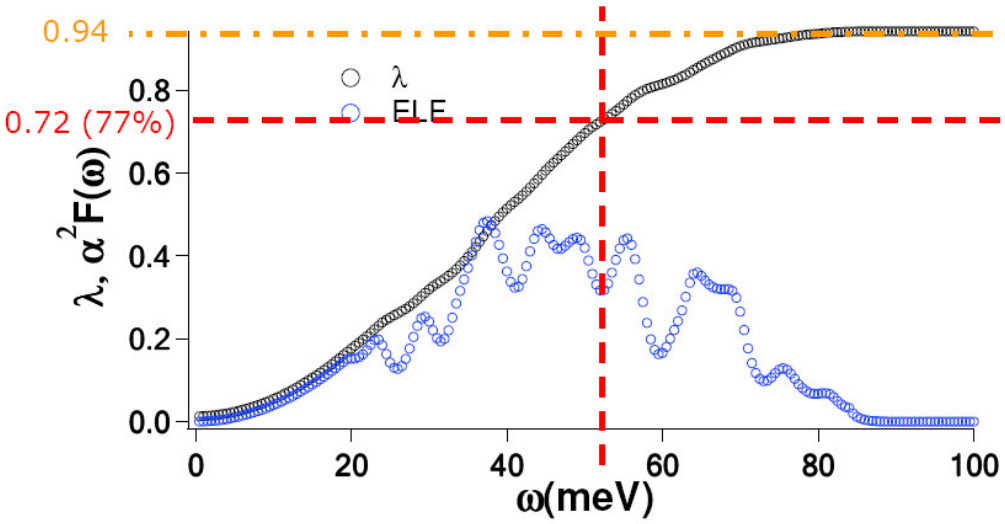

Figure 5.11. *Accumulated mass enhancement factor and extracted Eliashberg function as a function of energy.*

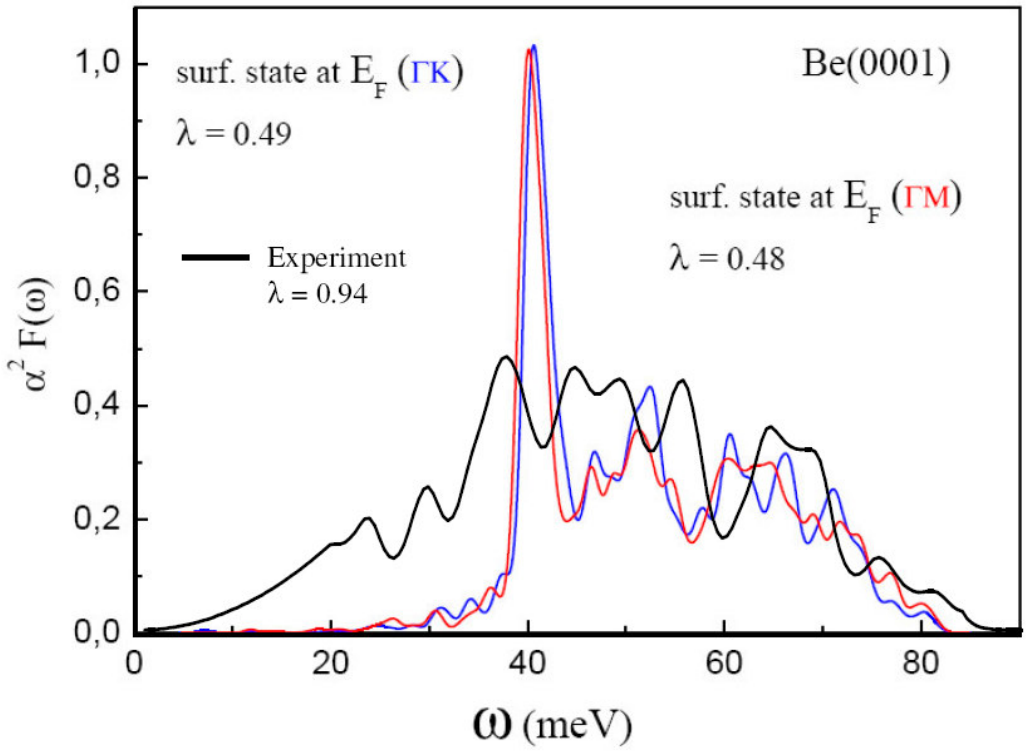

Figure 5.12. *Comparison between our experiment and Chulkov's theoretical results.*

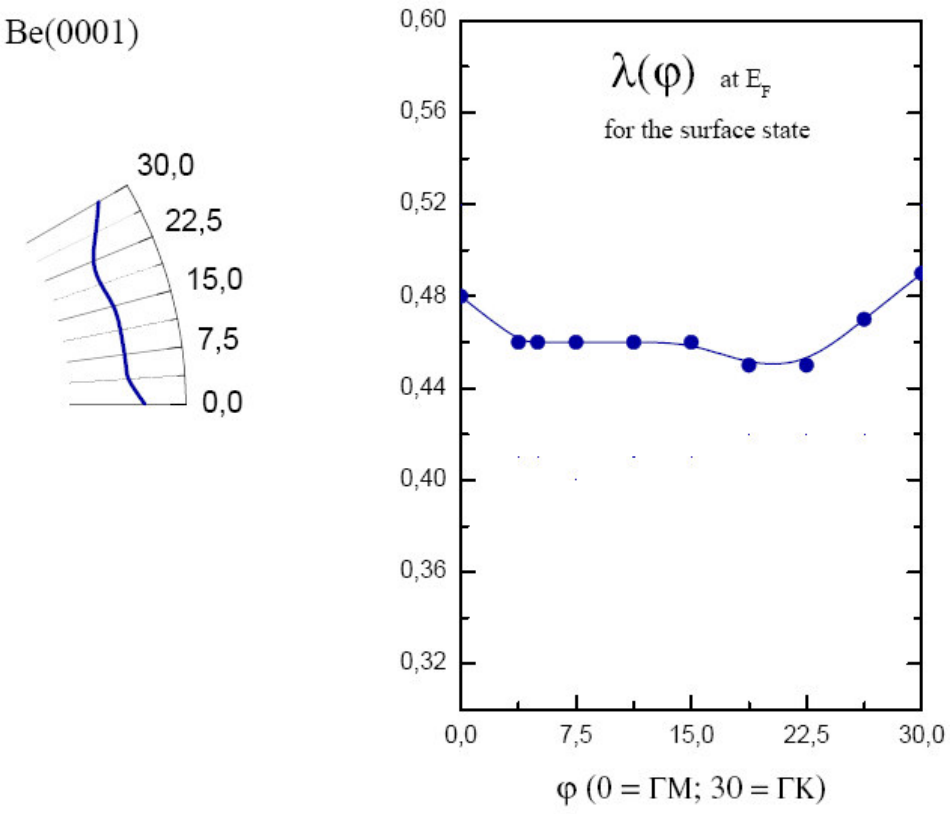

Figure 5.13. *Theoretical results of the angle-dependent mass enhancement factors from Chulkov's research group.*

dependent mass enhancement factors are not consistent to the anisotropic scenario, as we observed experimentally. This might be another important case, besides the graphene case [8], where the LDA calculation fails to capture the EPC correctly. Furthermore, the calculation of the ELF on surface is much harder than the bulk case. Most calculations are performed under a slab geometry to create surface in the model. In order to calculate the surface ELF, a more delicate way of calculation might be needed.

Summary

In summary, we demonstrated the extraction of the Eliashberg function from high-quality data. With an understanding of the effects from the energy resolution and the noise on the extraction procedure, we carefully extracted the Eliashberg function from the experimental ARPES data of Be(0001) along the $\overline{\Gamma}-\overline{M}$ direction. The peaks in the extracted Eliashberg function agree very well with the bulk and surface phonon DOS. High-energy peaks (higher than 52 meV) mainly originated from the bulk phonon; while the low-energy peaks (lower than 52 meV) mainly originated from the surface phonon. The contribution of the surface phonon to the mass enhancement factor is about 77%, equaling the value of 0.72, out of the total number of 0.94; while the contribution from the bulk phonon to the mass enhancement factor is 0.22, which is compatible to the value of the bulk mass enhancement factor, 0.24.

Chapter VI
Conclusion, Discussion, and Future Prospective

Conclusion

From the study of the EPC on the Be(0001) $\overline{\Gamma}$ surface state, we conclude that:

(1) For the case of the isotropic, free-electron-like, 2D electronic band (Be(0001) $\overline{\Gamma}$ surface state), the electron-phonon coupling still can be anisotropic. The mass enhancement factors are ranging from 0.6 to 1.1. There are two local maxima in the $\overline{\Gamma} \to \overline{M}$ direction (~1.1) and in the $\overline{\Gamma} \to \overline{K}$ direction (~0.9). The minimum of the mass enhancement factor appears $\sim 10^{\circ}$ away from the $\overline{\Gamma} \to \overline{K}$ direction (~0.6).

(2) It is proved that the Eliashberg function can be quantitatively extracted from high quality angle-resolved photoemission (ARPES) data.

(3) The Eliashberg function of Be(0001) $\overline{\Gamma}$ surface state along $\overline{\Gamma} - \overline{M}$ is extracted experimentally. The peaks in the extracted Eliashberg function agree very well with the bulk and surface phonon density of states. The contribution to the electron-phonon coupling from bulk phonon is mainly in the energy range higher than 52 meV; while the contribution from surface phonon is mainly with the energy lower than 52 meV. The contribution from the surface phonon to the mass enhancement factor is about 77%, which is about 0.72 out of the total value of 0.94.

(4) Theoretical calculation can not catch the anisotropic EPC scenario as well as the Eliashberg function. More efforts are needed in theoretical part.

(5) The energy resolution of the instrument in doing ARPES experiments will (a) distort the extracted dispersion within the range of the energy resolution; (b) suppress the kink; (c) smear the kink fine-structure; and (d) decrease the extracted $\mathrm{Im}\Sigma$.

(6) The momentum resolution of the instrument in doing ARPES experiments has little influence.

(7) MEM is very sensitive to the noise appearing in the data. The peaks in the extracted Eliashberg function from MEM will appear wherever the noise appears. This will result in unrepeatable extracted ELFs and prohibit the reliable extraction of ELFs.

(8) With our proposed procedure, the mass enhancement factor, λ, is very robust against energy resolution and noise. However, the different methods (slope method and phonon model method) used to extract λ would have inherent differences.

(9) The linear approximation for the bare dispersion has a wide range of validation, with the exception that the curvature of the bare dispersion is too large. In contrast, our proposed quadratic approximation works for the bare dispersion close to the quadratic form.

(10) Oxygen contamination has an observable influence on the EPC on the surface. Oxygen contamination would reduce the EPC.

(11) The non-radial measurements have little effect in determining the mass enhancement factors.

Discussion

(1) The anisotropic EPC observed on the Be(0001) surface is clearly not from the nature of the electronic band structure. The possible

sources of this anisotropic EPC are (a) the anisotropic nature of the phonon band and (b) the anisotropic coupling matrix. To understand the coupling details, the Eliashberg function is needed to be extracted experimentally.

(2) We proved that in order to extract Eliashberg function experimentally, noise in the data should be very small. Experimentally, we demonstrated that it is possible to obtain high quality data for the purpose of extracting Eliashberg function.

(3) From the extracted Eliashberg function of Be(0001) $\overline{\Gamma}$ surface state along $\overline{\Gamma}-\overline{M}$ direction, the contribution to the Eliashberg function from the bulk phonon is plausible. However, a theoretical understanding is needed for further determination of the surface phonon contributions. Even the contributions from different modes can be possibly explained theoretically.

(4) Because the energy resolution has a huge influence on the ARPES experiments, one has to be careful when analyzing data. The best strategy to minimize the energy resolution effects is to get high-resolution data when doing experiments. Without high-resolution data, the results about the electron-phonon coupling can be quantitatively doubtful. However, while the finite energy resolution data is unavoidable, our proposed procedure to analyze ARPES data is recommended to be used. The details of the procedure can be found in chapter III.

(5) The momentum resolution seems to be trivial; however, if the momentum resolution is too large—about 0.1 $\mathring{A}^{-1}$, then the effects on the extracted $\mathrm{Im}\Sigma$ would be significant.

(6) In order to get information about the coupling matrix from obtaining the ELFs using MEM, one has to have very low noise data. To achieve this, the measuring time should be increased. However, in the case of beryllium, the surface can only survive in

a low 10^{-10} Torr environment for about 4–6 hours. To increase the lifetime of the clean surface, the best strategy is to create a UHV environment in the low 10^{-11} torr range. This would increase the lifetime to one order more—a few days. With this, one can get high-quality data with low noise. We also proved this with a set of high quality data – low noise and high energy resolution.

(7) When talking about λ, it is important to remember that different methods would give systematic errors inherent in the methods themselves. To avoid this, it is better to use different methods to double check the results; however, it must be emphasized that MEM is the most trusted method to extract the EPC information.

(8) The linear approximation for bare dispersion seems to work very well in most cases, but one has to keep in mind that once the large curvature bare band is encountered, validation of the linear approximation is questionable.

(9) Non-radial measurements are commonly used in many ARPES experiments. Here, we address that even for detailed measurements of the kink, non-radial measurements have limited influences.

Future Perspective

With the knowledge that has been learned from this thesis, it is natural to ask: what next? The most obvious answer is: we need high-quality data in order to extract the coupling function—the Eliashberg function, $\alpha^2 F(\omega)$. This could be a function of the momentum - $\alpha^2 F(\omega, \vec{k})$. With this, the EPC details can be fully revealed. Though we already extracted the Eliashberg function along $\overline{\Gamma} - \overline{M}$ direction successfully, a systematically extraction is required in order to find out the momentum-

dependent Eliashberg function. Thus, the coupling matrix could be extracted.

The theory side of the story is another very important issue to be solved. As we demonstrated that the regular LDA calculation can not capture the EPC on Be(0001) surface, it is a challenge to improve the theoretical model. The difficult part of this calculation might originate from the calculation on the surface state. General approach for surface calculation is to create a slab-geometry, thus two surface can be identified – top most and bottom most of the geometry. The question is how thick slab is thick enough?

Other than the $\overline{\Gamma}$ surface state, Be(0001) also has the other surface state. There are no reports on the other surface state of Be(0001) concerning EPC strength. It might be important to map all the coupling strengths on the Be(0001) surface by studying the $\overline{M}$ surface state as well. The difficulty for this experiment would be the weak nature of this state.

To take this one step further, one needs to think about the other side of the EPC—the phonon. To gain more information, if one can obtain the coupling strength from measurements of phonons, one could use this information to compare both sides of the coupling. With this established, the procedure could be extended to other systems with different bosons.

To modify the surface is another approach for understanding the EPC. One can use hydrogen to passivate the surface of the beryllium. With this surface version doping method, one can expect to have one more electron doping per hydrogen, as well as another hydrogen vibration mode, which increases the phonon mode in the use of EPC. The enhanced EPC would be expected.

References

References for Chapter I

1. N. W. Ashcroft, and N. D. Mermin, *Solid State Physics* (Brooks/Cole, Thomson Learning, 1976).
2. R. Stedman, Z. Amilius, R. Pauli, and O. Sundin, "Phonon Spectrum of Beryllium at 80 K," *J. Phys. F: Metal Phys.* **6**, 157 (1976).
3. I. Yu. Sklyadneva, E. V. Chulkov, W.-D. Schöne, V. M. Silkin, R. Keyling, and P. M. Echenique, "Role of Electron-Phonon Interactions versus Electron-Electron Interactions in the Broadening Mechanism of the Electron and Hole Linewidths in Bulk Be," *Phys. Rev. B* **71**, 174302 (2005).
4. T. Cuk, D. H. Lu, X. J. Zhou, Z.-X. Shen, T. P. Devereaux, and N. Naaosa, "A Review of Electron-Phonon Coupling Seen in the High-T_c Superconductors by Angle-Resolved Photoemission Studies (ARPES)," *Phys. Status Solidi (b)* **242**, 11 (2005).
5. T. P. Devereaux, T. Cuk, Z. X. Shen, and N. Nagaosa, "Anisotropic Electron-Phonon Interaction in the Cuprates," *Phys. Rev. Lett.* **93**, 117004 (2004).
6. X. J. Zhou, Junren Shi, T. Yoshida, T. Cuk, W. L. Yang, V. Brouet, J. Nakamura, N. Mannella, S. Komiya, Y. Ando, F. Zhou, W. X. Ti, J. W. Xiong, Z. X. Zhao, T. Sasagawa, T. Kakeshita, H. Eisaki, S. Uchida, A. Fujimori, Zhenyu Zhang, E. W. Plummer, R. B. Laughlin, Z. Hussain, and Z.-X. Shen, "Multiple Bosonic Mode Coupling in Electron Self-Energy of $(La_{2-x}Sr_x)CuO_4$," *Phys. Rev. Lett.* **95**, 117001 (2005).
7. N. Mannella, W. L. Yang, X. J. Zhou, H. Zheng, J. F. Mitchell, J. Zaanen, T. P. Devereaux, N. Nagaosa, Z. Hussain, and Z.-X. Shen, "Nodal Quasiparticle in Pseudogapped Colossal Magnetoresistive Manganites," *Nature* **438**, 474 (2005).

8. P. Zhang, S. G. Louie, and M. L. Cohen, “Nonlocal Screening, Electron-Phonon Coupling, and Phonon Renormalization in Metals,” *Phys. Rev. Lett.* **94**, 225502 (2005).
9. T. Valla, J. Camacho, Z.-H. Pan, A. V. Fedorov, A. C. Walters, Ca. A. Howard, and M. Ellerby, “Anisotropic Electron-Phonon Coupling and Dynamical Nesting on the Graphene Sheets in Superconducting CaC_6 Using Angle-Resolved Photoemission Spectroscopy,” *Phys. Rev. Lett.* **102**, 107007(2009).
10. Robert Laughlin, *A Different Universe, Reinventing Physics from the Bottom Down* (Basic Books, 2005)
11. The April 21st Issue of *Science*, **288** (2000), was dedicated to Correlated Electron Systems.
12. T. Ohta, A. Bostwick, T. Seyller, K. Horn, and E. Rotenberg, “Controlling the Electronic Structure of Bilayer Graphene,” *Science* **313**, 951 (2006).
13. V. B. Zabolotnyy, D. S. Inosov, D. V. Evtushinsky, A. Koitzsch, A. A. Kordyuk, G. L. Sun, J. T. Park, D. Haug, V. Hinkov, A. V. Boris, C. T. Lin, M. Knupfer, A. N. Yaresko, B. Büchner, A. Varykhalov, R. Follath, and S. V. Borisenko, “(π,π) Electronic Order in Iron Arsenide Superconductors,” *Nature* **457**, 569 (2009).
14. S.-J. Tang, J. Shi, B. Wu, P. T. Sprunger, W. L. Yang, V. Brouet, X. J. Zhou, Z. Hussain, Z.-X. Shen, Z. Zhang, and E. W. Plummer, “A Spectroscopic View of Electron-Phonon Coupling at Metal Surfaces,” *Phys. Status Solidi (b)* **241**, 2345 (2004).
15. M. Hengsberger, D. Purdie, P. Segovia, and Y. Baer, ”Photoemission Study of a Strongly Coupled Electron-Phonon System,” *Phys. Rev. Lett.* **83**, 592 (1999).
16. M. Hengsberger, R. Fresard, D. Purdie, P. Segovia, and Y. Baer, ”Electron-Phonon Coupling in Photoemission Spectra,” *Phys. Rev. B* **60**, 10796 (1999).

17. S. LaShell, E. Jensen, and T. Balasubramanian, “Nonquasiparticle Structure in the Photoemission Spectra from the Be(0001) Surface and Determination of the Electron Self Energy,” *Phys. Rev. B* **61**, 2371 (2000).
18. T. Balasubramanian, E. Jensen, X. L. We, and S. L. Hulbert, “Large Value of the Electron-Phonon Coupling Parameter (λ=1.15) and the Possibility of Surface Superconductivity at the Be(0001) Surface,” *Phys. Rev. B* **57**, R6866 (1998).
19. S.-J. Tang, Ismail, P. T. Sprunger, and E. W. Plummer, “Electron-Phonon Coupling and Temperature-Dependent Shift of Surface States on Be(10$\bar{1}$0),” *Phys. Rev. B* **65**, 235428 (2002).
20. J. Shi, S.-J. Tang, B. Wu, P. T. Sprunger, W. L. Yang, V. Brouet, X. J. Zhou, Z. Hussain, Z.-X. Shen, Z. Zhang, and E. W. Plummer, “Direct Extraction of the Eliashberg Function for Electron-Phonon Coupling: A Case Study of Be(10$\bar{1}$0),” *Phys. Rev. Lett.* **92**, 186401 (2004).
21. T. Balasubramanian, L. I. Johansson, P.-A. Glans, C. Virojanadara, V. M. Silkin, E. V. Chulkov, and P. M. Echenique, “Surface Electronic Band Structure and $\bar{A}$ Surface State Lifetimes at the Be(10$\bar{1}$0) Surface: Experiment and Theory,” *Phys. Rev. B* **64**, 205401 (2001).
22. T. Balasubramanian, P.-A. Glans, and L. I. Johansson, “Electron-Phonon Mass-Enhancement Parameter and the Fermi-Line eccentricity at the Be(10$\bar{1}$0) Surface from Angle-Resolved Photoemission,” *Phys. Rev. B* **61**, 12709 (2000).
23. J. Graf, G.-H. Gweon, K. McElroy, S. Y. Zhou, C. Jozwiak, E. Rotenberg, A. Bill, T. Sasagawa, G. Eisaki, S. Uchida, H. Takagi, D.-H. Lee, and A. Lanzara, “Universal High-Energy Anomoly in the Angle-Resolved Photoemission Spectra of High Temperature Superconductors: Possible Evidence of Spinon and Holon Branches,” *Phys. Rev. Lett.* **98**, 067004 (2007).

24. T. Valla, T. E. Kidd, W.-G. Yin, G. D. Gu, P. D. Johnson, Z.-H. Pan, and A. V. Fedorov, "High-Energy Kink Observed in the Electron Dispersion of High-Temperature Cuprate Superconductors," *Phys. Rev. Lett.* **98**, 167003 (2007).
25. B. P. Xie, K. Yang, D. W. Shen, J. F. Zhao, H. W. Ou, J. Wei, S. Y. Gu, M. Arita, S. Qiao, H. Namatame, M. Taniguchi, N. Kaneko, H. Eisaki, K. D. Tsuei, C. M. Cheng, I. Vobornik, J. Fujii, G. Rossi, Z. Q. Yang, and D. L. Feng, "High-Energy Scale Revival and Giant Kink in the Dispersion of a Cuprate Superconductor," *Phys. Rev. Lett.* **98**, 147001 (2007).
26. R. Heid, K.-P. Bohnen, R. Zeyher, and D. Manske, "Momentum Dependence of the Electron-Phonon Coupling and Self-Energy Effects in Superconducting $YBa_2Cu_3O_7$ Within the Local Density Approximation," *Phys. Rev. Lett.* **100**, 137001 (2008).
27. M. R. Norman, H. Ding, M. Randeria, J. C. Campuzano, T. Yokoya, T. Takeuchi, T. Takahashi, T. Mochiku, K. Kadowaki, P. Guptasarma, and D. G. Hinks, "Destruction of the Fermi Surface in Underdoped High-T_c Superconductors," *Nature* **392**, 157 (1998).
28. J. Bardeen, L. N. Cooper, and J. R. Schrieffer, "Theory of Superconductivity," *Phys. Rev.* **108**, 1175 (1957).
29. J. Bardeen, L. N. Cooper, and J. R. Schrieffer, "Microscopic Theory of Superconductivity," *Phys. Rev.* **106**, 162 (1957).
30. L. N. Cooper, "Bound Electron Pairs in a Degenerate Fermi Gas," *Phys. Rev.* **104**, 1189 (1956).
31. E. Jensen, R. A. Bartynski, T. Gustafsson, E. W. Plummer, M. Y. Chou, M. L. Cohen, and G. B. Hoflund, "Angle-Resolved Photoemission Study of the Electronic Structure of Beryllium: Bulk Band Dispersions and Many-Electron Effects," *Phys. Rev. B* **30**, 5500 (1984).

32. J. B. Hannon, E. J. Mele, and E. W. Plummer, “Phonon Dispersion at the Be(0001) Surface,” *Phys. Rev. B* **53**, 2090 (1996).
33. G. Grimvall, *The Electron-Phonon Interaction in Metals, Selected Topics in Solid State Physics*, ed. by E. Wohlfarth (North-Holland, New York, 1981).
34. G. D. Mahan, *Many-Particle Physics, Physics of Solids and Liquids* (Kluwer Academic/Plenum Publishers, New York, 2000).
35. R. L. Falge Jr., ”Superconductivity of Hexagonal Beryllium,” *Phys. Lett.* **24A**, 579 (1967).
36. N. E. Alekseevskii, and V. I. Tsebro, “Superconductivity of Cold Deposited Beryllium Films,” *J. Low Temp. Phys.* **4**, 679 (1971).
37. H. L. Davis, J. B. Hannon, K. B. Ray, and E. W. Plummer, “Anomalous Interplanar Expansion at the (0001) Surface of Be,” *Phys. Rev. Lett.* **68**, 2632 (1992).
38. K. Pohl, J.-H. Cho, K. Terakura, M. Scheffler, and E. W. Plummer, “Anomalously Large Thermal Expansion at the (0001) Surface of Beryllium Without Observable Interlayer Anharmonicity,” *Phys. Rev. Lett.* **80**, 2853 (1998).
39. Ismail, P. Hofmann, A. P. Baddorf, and E. W. Plummer, “Thermal Expansion at a Metal Surface: A Study of Mg(0001) and Be(10$\bar{1}$0),” *Phys. Rev. B* **66**, 245414 (2002).
40. J. B. Hannon, E. W. Plummer, R. M. Wentzcovitch, and P. K. Lam, “The (1×3) Missing-Row Surface Structure of Be(11$\bar{2}$0),” *Surf. Sci.* **269/270**, 7 (1992).
41. Ph. Hofmann, and E. W. Plummer, “Lattice Vibrations at the Be(10$\bar{1}$0) Surface,” *Surf. Sci.* **377–379**, 330 (1997).
42. Ph. Hofmann, R. Stumpf, V. M. Silkin, E. V. Chulkov, and E. W. Plummer, “The Electronic Structure of Be(10$\bar{1}$0),” *Surf. Sci.* **355**, L278 (1996).

43. R. A. Bartynski, E. Jensen, T. Gustafsson, and E. W. Plummer, “Angle-Resolved Photoemission Investigation of the Electronic Structure of Be: Surface States,” *Phys. Rev. B* **32**, 1921 (1985).
44. A. Eiguren, S. de Gironcoli, E. V. Chulkov, P. M. Echenique, and E. Tosatti, “Electron-Phonon Interaction at the Be(0001) Surface,” *Phys. Rev. Lett.* **91**, 166803 (2003).
45. E. V. Chulkov, V. M. Silkin, and E. N. Shirykalov, “Surface Electronic Structure of Be(0001) and Mg(0001),” *Surf. Sci.* **188**, 287(1987).
46. J. B. Hannon, and E. W. Plummer, “Shear Horizontal Vibrations at the (0001) Surface of Beryllium,” *J. Elect. Spectros. Rel. Phenom.* **64/65**, 683 (1993).
47. E. W. Plummer, and J. B. Hannon, “The Surfaces of Beryllium,” *Prog. Surf. Sci.* **46**, 149 (1994).
48. L. I. Johansson and B. E. Sernelius, “Electron Mean Free Path in Be Metal,” *Phys. Rev. B* **50**, 16817(1994).
49. J. C. Boettger and S. B. Trickey, “Electronic Surface States in Beryllium,” *Phys. Rev. B* **34**, 3604 (1986).
50. L. I. Johansson, H. I. P. Johansson, J. N. Andersen, E. Lundgren, and R. Nyholm, ”Three Surface-Shifted Core Levels on Be(0001),” *Phys. Rev. Lett.* **71**, 2453 (1993).
51. U. O. Karlsson, S. A. Flodström, R. Engelhardt, W. Gädeke, and E. E. Koch, “Intrinsic Surface State on Be(0001),” *Solid State Commun.* **49**, 711 (1984).
52. V. M. Silkin, T. Balasubramanian, E. V. Chulkov, A. Rubio, and P. M. Echenique, “Surface State Hole Decay Mechanisms: The Be(0001) Surface,” *Phys. Rev. B* **64**, 085334(2001).
53. P.-A. Glans, L. I. Johansson, T. Balasubramanian, and R. J. Blake, *Phys. Rev. B* **70**, 033408 (2004).

54. P. T. Sprunger, L. Petersen, E. W. Plummer, E. Lægsgaard, and F. Besenbacher, ”Giant Friedel Oscillations on the Beryllium(0001) Surface,” *Science* **275**, 1764 (1997).
55. Ph. Hofmann, B. G. Briner, M. Doering, H.-P. Rust, E. W. Plummer, and A. M. Bradshaw, “Anisotropic Two-Dimensional Friedel Oscillations,” *Phys. Rev. Lett.* **79**, 265 (1997).
56. B. G. Lazarev, E. E. Semenenko, and A. I. Sudowtsov, “Modification of Beryllium and Iron in Films Condensed onto Cold Substrates,” *Soviet Phys. JETP* **13**, 75 (1961).
57. K. Takei, M. Okamoto, K. Nakanura, and Y. Maeda, “Synthesis of Superconducting Beryllium Thin Film by Ion Beam Sputtering,” *Jpn. J. Appl. Phys., Part 1* **26**, 386 (1987).

References for Chapter II

1. J. Bardeen, L. N. Cooper, and J. R. Schrieffer, “Theory of Superconductivity,” *Phys. Rev.* **108**, 1175 (1957).
2. J. Bardeen, L. N. Cooper, and J. R. Schrieffer, “Microscopic Theory of Superconductivity,” *Phys. Rev.* **106**, 162 (1957).
3. L. N. Cooper, “Bound Electron Pairs in a Degenerate Fermi Gas,” *Phys. Rev.* **104**, 1189 (1956).
4. H. Fröhlich, “Theory of the Superconducting State. I. The Ground State at the Absolute Zero of Temperature,” *Phys. Rev.* **79**, 845 (1950).
5. G. Grimvall, *The Electron-Phonon Interaction in Metals, Selected Topics in Solid State Physics*, ed. by E. Wohlfarth (North-Holland, New York, 1981).
6. S.-J. Tang, J. Shi, B. Wu, P. T. Sprunger, W. L. Yang, V. Brouet, X. J. Zhou, Z. Hussain, Z.-X. Shen, Z. Zhang, and E. W. Plummer, “A Spectroscopic View of Electron-Phonon Coupling at Metal Surfaces,” *Phys. Status Solidi (b)* **241**, 2345 (2004).
7. N. W. Ashcroft, and N. D. Mermin, *Solid State Physics* (Brooks/Cole, Thomson Learning, 1976).
8. F. Reinert, and S. Hüfner, “Photoemission Spectroscopy - From Early Days to Recent Applications,” *New J. Phys.* **7**, 97 (2005).
9. A. Damascelli, “Probing the Electronic Structure of Complex Systems by ARPES,” *Phys. Scrip.* **T109**, 61 (2004).
10. M. P. Seah, and W. A. Dench, *Interface Anal.* **1**, 2 (1979).
11. N. V. Smith, P. Thiry, and Y. Petroff, “Photoemission Linewidths and Quasiparticle Lifetimes,” *Phys. Rev. B* **47**, 15476 (1993).
12. M. Hengsberger, D. Purdie, P. Segovia, and Y. Baer, ”Photoemission Study of a Strongly Coupled Electron-Phonon System,” *Phys. Rev. Lett.* **83**, 592 (1999).

13. S. LaShell, E. Jensen, and T. Balasubramanian, “Nonquasiparticle Structure in the Photoemission Spectra from the Be(0001) Surface and Determination of the Electron Self Energy,” *Phys. Rev. B* **61**, 2371 (2000).
14. A. Eiguren, S. de Gironcoli, E. V. Chulkov, P. M. Echenique, and E. Tosatti, “Electron-Phonon Interaction at the Be(0001) Surface,” *Phys. Rev. Lett.* **91**, 166803 (2003).
15. T. Balasubramanian, and E. Jensen, “Large Value of the Electron-Phonon Coupling Parameter (λ=1.15) and the Possibility of Surface Superconductivity at the Be(0001) Surface,” *Phys. Rev. B* **57**, R6866 (1998).
16. S.-J. Tang, Ismail, P. T. Sprunger, and E. W. Plummer, “Electron-Phonon Coupling and Temperature-Dependent Shift of Surface States on Be(10$\bar{1}$0),” *Phys. Rev. B* **65**, 235428 (2002).
17. T. Balasubramanian, L. I. Johansson, P.-A. Glans, C. Virojanadara, V. M. Silkin, E. V. Chulkov, and P. M. Echenique, “Surface Electronic Band Structure and $\bar{A}$ Surface State Lifetimes at the Be(10$\bar{1}$0) Surface: Experiment and Theory,” *Phys. Rev. B* **64**, 205401 (2001).
18. T. Balasubramanian, P.-A. Glans, and L. I. Johansson, “Electron-Phonon Mass-Enhancement Parameter and the Fermi-Line eccentricity at the Be(10$\bar{1}$0) Surface from Angle-Resolved Photoemission,” *Phys. Rev. B* **61**, 12709 (2000).
19. M. Hengsberger, R. Fresard, D. Purdie, P. Segovia, and Y. Baer, ”Electron-Phonon Coupling in Photoemission Spectra,” *Phys. Rev. B* **60**, 10796 (1999).
20. J. Shi, S.-J. Tang, B. Wu, P. T. Sprunger, W. L. Yang, V. Brouet, X. J. Zhou, Z. Hussain, Z.-X. Shen, Z. Zhang, and E. W. Plummer, “Direct Extraction of the Eliashberg Function for Electron-Phonon Coupling: A Case Study of Be(10$\bar{1}$0),” *Phys. Rev. Lett.* **92**, 186401 (2004).

21. R. A. Bartynski, E. Jensen, T. Gustafsson, and E. W. Plummer, “Angle-Resolved Photoemission Investigation of the Electronic Structure of Be: Surface States,” *Phys. Rev. B* **32**, 1921 (1985).

References for Chapter III

1. J. Shi, S.-J. Tang, B. Wu, P. T. Sprunger, W. L. Yang, V. Brouet, X. J. Zhou, Z. Hussain, Z.-X. Shen, Z. Zhang, and E. W. Plummer, "Direct Extraction of the Eliashberg Function for Electron-Phonon Coupling: A Case Study of Be($10\bar{1}0$)," *Phys. Rev. Lett.* **92**, 186401 (2004).
2. S.-J. Tang, J. Shi, B. Wu, P. T. Sprunger, W. L. Yang, V. Brouet, X. J. Zhou, Z. Hussain, Z.-X. Shen, Z. Zhang, and E. W. Plummer, "A Spectroscopic View of Electron-Phonon Coupling at Metal Surfaces," *Phys. Status Solidi (b)* **241**, 2345 (2004).
3. M. Hengsberger, D. Purdie, P. Segovia, M. Garnier, and Y. Baer, "Photoemission Study of a Strongly Coupled Electron-Phonon System," *Phys. Rev. Lett.* **83**, 592 (1999).
4. M. Hengsberger, R. Frésard, D. Purdie, P. Segovia, and Y. Baer, "Electron-Phonon Coupling in Photoemission Spectra," *Phys. Rev. B* **60**, 10796 (1999).
5. S. LaShell, E. Jensen, and T. Balasubramanian, "Nonquasiparticle Structure in the Photoemission Spectra from the Be(0001) Surface and Determination of the Electron Self Energy," *Phys. Rev. B* **61**, 2371 (2000).
6. A. Eiguren, S. De Gironcoli, E. V. Chulkov, P. M. Echenique, and E. Tosatti, "Electron-Phonon Interaction at the Be(0001) Surface," *Phys. Rev. Lett.* **91**, 166803 (2003).
7. E. V. Chulkov, V. M. Silkin, and E. N. Shirykalov, "Surface Electronic Structure of Be(0001) and Mg(0001)," *Surf. Sci.* **188**, 287 (1987).
8. J. E. Gayone, C. Kirkegaard, J. W. Wells, S. V. Hoffmann, Z. Li, and P. Hofmann, *Appl. Phys. A* **80**, 943 (2005).
9. F. Baumberger, N. J. C. Ingle, W. Meevasana, K.M. Shen, D. H. Lu, R. S. Perry, A. P. Mackenzie, Z. Hussain, D. J Singh, and Z.-X.

Shen, “Fermi Surface and Quasiparticle Excitations of Sr_2RhO_4,” *Phys. Rev. Lett.* **96**, 246402 (2006).

10. A. Kaminski and Helen M. Fretwell, “On the Extraction of the Self-Energy from Angle-Resolved Photoemission Spectroscopy,” *New J. Phys.* **6**, 98 (2004).
11. T. Valla, “Comment on “Multiple Bosonic Mode Coupling in the Electron Self-Energy of $(La_{2-x}Sr_x)CuO_4$”,” *Phys. Rev. Lett.* **96**, 119701 (2006).
12. X. J. Zhou, J. Shi, W. L. Yang, S. Komiya, Y. Ando, E. W. Plummer, Z. Hussain, and Z.-X. Shen, *Phys. Rev. Lett.* **96**, 119702 (2006).
13. X. J. Zhou, J. Shi, T. Yoshida, T. Cuk, W. L. Yang, V. Brouet, J. Nakamura, N. Mannella, S. Komiya, Y. Ando, F. Zhou, W. X. Ti, J. W. Xiong, Z. X. Zhao, T. Sasagawa, T. Kakeshita, H. Eisaki, S. Uchida, A. Fujimori, Z. Zhang, E. W. Plummer, R. B. Laughlin, Z. Hussain, and Z.-X. Shen, “Multiple Bosonic Mode Coupling in the Electron Self-Energy of $(La_{2-x}Sr_x)CuO_4$,” *Phys. Rev. Lett.* **95**, 117001 (2005).
14. T. Valla, A. V. Fedorov, P. D. Johnson, B. O. Wells, S. L. Hulbert, Q. Li, G. D. Gu, and N. Koshizuka, “Evidence for Quantum Critical Behavior in the Optimally Doped Cuprate $Bi_2Sr_2CaCu_2O_8$,” *Science* **285**, 2110 (1999).
15. A. Kaminski, M. Randeria, J. C. Campuzano, M. R. Norman, H. Fretwell, J. Mesot, T. Sato, T. Takahashi, and K. Kadowaki, “Renormalization of Spectral Line Shape and Dispersion below T_c in $Bi_2Sr_2CaCu_2O_{8+\delta}$,” *Phys. Rev. Lett.* **86**, 1070 (2001).
16. The definition of the curvature is $\kappa = |y''(x)| / \left[1+(y'(x))^2\right]^{3/2}$; here, *y* represents the binding energy in eV units and *x* represents the momentum in $Å^{-1}$ units.

17. J. E. Inglesfield and E. W. Plummer in *Angle-Resolved Photoemission*, ed. By S. D. Kevan (Elsevier, Amsterdam, 1992).
18. C. Kirkegaard, T. K. Kim, and P. Hofmann, "Self-Energy Determination and Electron-Phonon Coupling on Bi(110)" *New. J. Phys.* **7**, 99 (2005).
19. Private communication with E. V. Chulkov.
20. A. A. Kordyuk, S. V. Borisenko, A. Koitzsch, J. Fink, M. Knupfer, and H. Berger, "Bare Electron Dispersion from Experiment: Self-Consistent Self-Energy Analysis of Photoemission Data," *Phys. Rev. B* **71**, 214513 (2005).
21. N. V. Smith, P. Thiry, and Y. Petroff, "Photoemission Linewidths and Quasiparticle Lifetimes," *Phys. Rev. B* **47**, 15476 (1993).
22. L. Kipp, K. Robnagel, C. Solterbeck, T. Strasser, W. Schattke, and M. Skibowski, "How to Determine Fermi Vectors by Angle-Resolved Photoemission," *Phys. Rev. Lett.* **83**, 5551 (1999).
23. M. Randeria, H. Ding, J.-C. Campuzano, A. Bellman, G. Jennings, T. Yokoya, T. Takahashi, H. Katayama-Yoshida, T. Mochiku, and K. Kadowaki, "Momentum Distribution Sum Rule for Angle-Resolved Photoemission," *Phys. Rev. Lett.* **74**, 4951 (1995).

References for Chapter IV

1. The April 21st Issue of *Science*, **288** (2000), was dedicated to Correlated Electron Systems.
2. T. Cuk, D. H. Lu, X. J. Zhou, Z.-X. Shen, T. P. Devereaux, and N. Naaosa, "A Review of Electron-Phonon Coupling Seen in the High-T_c Superconductors by Angle-Resolved Photoemission studies (ARPES)," *Phys. Status Solidi (b)* **242**, 11 (2005).
3. P. Zhang, S. G. Louie, and M. L. Cohen, "Nonlocal Screening, Electron-Phonon Coupling, and Phonon Renormalization in Metals," *Phys. Rev. Lett.* **94**, 225502 (2005).
4. T. P. Devereaux, T. Chuk, Z. X. Shen, and N. Nagaosa, "Anisotropic Electron-Phonon Interaction in the Cuprates," *Phys. Rev. Lett.* **93**, 117004 (2004).
5. J. Zhou, Junren Shi, T. Yoshida, T. Cuk, W. L. Yang, V. Brouet, J. Nakamura, N. Mannella, S. Koviya, Y. Ando, F. Zhou, W. X. Ti, J. W. Xiong, Z. X. Zhao, T. Sasagawa, T. Kakeshita, H. Eisaki, S. Uchida, A. Fugimori, Zhenyu Zhang, E. W. Plummer, R. B. Laughlin, Z. Hussain, and Z.-X. Shen, "Multiple Bosonic Mode Coupling in Electron Self-Energy of $(La_{2-x}Sr_x)CuO_4$," *Phys. Rev. Lett.* **95**, 117001 (2005).
6. N. Mannella, W. L. Yang, X. J. Zhou, H. Zheng, J. F. Mitchell, J. Zaanen, T. P. Devereaux, N. Nagaosa, Z. Hussain, and Z.-X. Shen, "Nodal Quasiparticle in Pseudogapped Colossal Magnetoresistive Manganites," *Nature* **438**, 474 (2005).
7. T. Valla, J. Camacho, Z.-H. Pan, A. V. Fedorov, A. C. Walters, Ca. A. Howard, and M. Ellerby, "Anisotropic Electron-Phonon Coupling and Dynamical Nesting on the Graphene Sheets in CaC_6," to be published.
8. R. Heid, K.-P. Bohnen, R. Zeyher, and D. Manske, "Momentum Dependence of the Electron-Phonon Coupling and Self-Energy

Effects in Superconducting $YBa_2Cu_3O_7$ within the Local Density Approximation," *Phys. Rev. Lett.* **100**, 137001 (2008).

9. S. R. Park, D. J. Song, C. S. Leem, C. Kim, C. Kim, B. J. Kim, and H. Eisaki, "Angle-Resolved Photoemission Spectroscopy of Electron-Doped Cuprate Superconductors: Isotropic Electron-Phonon Coupling," *Phys. Rev. Lett.* **101**, 117006 (2008).
10. E. V. Chulkov, V. M. Silkin, and E. N. Shirykalov, "Surface Electronic Structure of Be(0001) and Mg(0001)," *Surf. Sci.* **188**, 287 (1987).
11. P. J. Feibelman, "First-Principles Calculation of the Geometric and Electronic Structure of the Be(0001) Surface," *Phys. Rev. B* **46**, 2532 (1992).
12. M. Lazzeri and S. de Gironcoli, "*Ab-Initio* Study of Be(0001) Surface Thermal Expansion," *Phys. Rev. Lett.* **81**, 2096 (1998).
13. J. B. Hannon, E. J. Mele, and E. W. Plummer, "Phonon Dispersion at the Be(0001) Surface," *Phys. Rev. B* **53**, 2090 (1996).
14. M. Lazzeri and S. de Gironcoli, "*Ab-Initio* Dynamical Properties of the Be(0001) Surface," *Surf. Sci.* ***4*02–404**, 715 (1998).
15. R. A. Bartynski, E. Jensen, T. Gustafsson, and E. W. Plummer, "Angle-Resolved Photoemission Investigation of the Electronic Structure of Be: Surface States," *Phys. Rev. B* **32**, 1921 (1985).
16. G. M. Watson, P. A. Bruhwiler, E. W. Plummer, H. J. Sagner, and K.-H. Frank, "Two-Dimensional Band Structure of Li Layer: Li/Be(0001)," *Phys. Rev. Lett.* **65**, 468 (1990).
17. M. Hengsberger, D. Purdie, P. Segovia, M. Garnier, and Y. Baer, "Photoemission Study of a Strongly Coupled Electron-Phonon System" *Phys. Rev. Lett.* **83**, 592 (1999).
18. S. LaShell, E. Jensen, and T. Balasubramanian, "Nonquasiparticle Structure in the Photoemission Spectra from the Be(0001) Surface and Determination of the Electron Self Energy," *Phys. Rev. B* **61**, 2371 (2000).

19. T. Balasubramanian, E. Jensen, X. L. Wu, and S. L. Hulbert, “Large Value of the Electron-Phonon Coupling Parameter (λ = 1.15) and the Possibility of Surface Superconductivity at the Be(0001) Surface,” *Phys. Rev. B* **57**, R6866 (1988).
20. M. Hengsberger, R. Frésard, D. Purdie, P. Segovia, and Y. Baer, “Electron-Phonon Coupling in Photoemission Spectra,” *Phys. Rev. B* **60**, 10796 (1999).
21. S.-J. Tang, Junren Shi, Biao Wu, P. T. Sprunger, W. L. Yang, V. Brouet, X. J. Zhou, Z. Hussain, Z.-X. Shen, Zhenyu Zhang, and E. W. Plummer, “A Spectroscopic View of Electron-Phonon Coupling at Metal Surfaces,” *Phys. Status Solidi (b)* **241**, 2345 (2004).
22. A. Eiguren, S. de Gironcoli, E. V. Chulkov, P. M. Echenique, and E. Tosatti, “Electron-Phonon Interaction at the Be(0001) Surface,” *Phys. Rev. Lett.* **91**, 166803 (2003).
23. S. V. Hoffmann, Ch. Sondergaard, Ch. Schultz, Z. Li, and Ph. Hofmann, “An Undulator-Based Spherical Grating Monochromator Beamline for Angle-Resolved Photoemission Spectroscopy,” *Nuclear Instrum. Methods in Physics Research, Sect. A* **523**, 441 (2004).
24. G. D. Mahan, *Many-Particle Physics, Third Edition*, Springer, Berlin, Germany, 2007.
25. Junren Shi, S.-J. Tang, Biao Wu, P. T. Sprunger, W. L. Yang, V. Brouet, X. J. Zhou, Z. Hussain, Z.-X. Shen, Zhenyu Zhang, and E. W. Plummer, “Direct Extraction of the Eliashberg Function for Electron-Phonon Coupling: A Case Study of $Be(10\bar{1}0)$,” *Phys. Rev. Lett.* **92**, 186401 (2004).
26. C. Kirkegaard, T. K. Kim, and Ph. Hofmann, “Self-Energy Determination and Electron-Phonon Coupling on Bi(110),” *New J. Phys.* **7**, 99(2005).
27. T.Y. Chien et. al., to be submitted to *Physical Review B*.

28. A. A. Kordyuk, S. V. Borisenko, A. Koitzsch, J. Fink, M. Knupfer, and H. Berger, "Bare Electron Dispersion from Experiment: Self-Consistent Self-Energy Analysis of Photoemission Data," *Phys. Rev. B* **71**, 214513 (2005).
29. G. Grimvall, "*The Electron-Phonon Interaction in Metals*" (North-Holland, New York, 1981).
30. M. Lazzeri, C. Attaccalite, L. Wirtz, and F. Mauri, "Impact of the Electron-Electron Correlation on Phonon Dispersion: Failure of LDA and GGA DFT Functionals in Graphene and Graphite," *Phys. Rev. B* **78**, 081406(R) (2008).
31. N. Bulut and D. J. Scalapino, "$d_{x^2-y^2}$ Symmetry and the Pairing Mechanism," *Phys. Rev. B* **54**, 14971 (1996).

References for Chapter V

1. J. P. Carbotte, “Properties of Boson-Exchange Superconductors,” *Rev. Mod. Phys.* **62**, 1027(1990).
2. G. M. Eliashberg, “Interactions Between Electrons and Lattice Vibrations in a Superconductor,” *Soviet Phys. JETP* **11**, 696 (1960).
3. F. Reinert, B. Eltner, G. Nicolay, E. Ehm, S. Schmidt, and S. Hüfner, “Electron-Phonon Coupling and its Evidence in the Photoemission Spectra of Lead,” *Phys. Rev. Lett.* **91**, 186406(2003).
4. J. Shi, S.-J. Tang, B. Wu, P. T. Sprunger, W. L. Yang, V. Brouet, X. J. Zhou, Z. Hussain, Z.-X. Shen, Z. Zhang, and E. W. Plummer, “Direct Extraction of the Eliashberg Function for Electron-Phonon Coupling: A Case Study of Be($10\bar{1}0$),” *Phys. Rev. Lett.* **92**, 186401 (2004).
5. R. Stedman, Z. Amilius, R. Pauli, and O. Sundin, “Phonon Spectrum of Beryllium at 80K,” *J. Phys. F: Metal Phys.* **6**, 157(1976).
6. I. Yu. Sklyadneva, E. V. Chulkov, W.-D. Schöne, V. M. Silkin, R. Keyling, and P. M. Echenique, “Role of electron-phonon interactions versus electron-electron interactions in the broadening mechanism of the electron and hole linewidths in bulk Be,” *Phys. Rev. B* **71**, 174302 (2005).
7. J. B. Hannon, E. J. Mele, and E. W. Plummer, “Phonon Dispersion at the Be(0001) surface,” *Phys. Rev. B* **53**, 2090(1996).
8. M. Lazzeri, C. Attaccalite, L. Wirtz, and F. Mauri, “Impact of the Electron-Electron Correlation on Phonon Dispersion: Failure of LDA and GGA DFT Functionals in Graphene and Graphite,” *Phys. Rev. B* **78**, 081406(R) (2008).

VITA

Te-Yu Chien was born in Taipei, Taiwan, on February 19, 1979. After graduating from The Affiliated Senior High School of National Taiwan Normal University, Taipei, Taiwan, he attended National Taiwan Normal University in Taipei where he graduated with a Bachelor of Science degree in Physics in 2001. During the undergraduate study, he was selected as the Gifted Student for Science & Mathematics and joined professor Chih-Ta Chia's research group. Right after the undergraduate study, he enrolled in the master program in National Taiwan Normal University and also stayed in the same research group. In his masters program, he was selected as the Outstanding Graduate Student and studied the Raman spectroscopy and the Photoluminescence of the spherical silicon quantum dots. In 2002, he transferred to Ph. D program and passed the qualifying exam. In order to be educated in more delicate way and to experience better scientific environment, he decided to transfer to The University of Tennessee, Knoxville, Tennessee, to finish his Ph. D degree. During the period of waiting for application result in early 2004, he served as a junior high school Science teacher. In Fall, 2004, he entered The University of Tennessee, Knoxville, Tennessee as a doctoral student in Physics studying the electron-phonon coupling on the (0001) surface of beryllium under the instruction of professor Ward Plummer. While as a doctoral student he received the Tennessee Advanced Materials Laboratory Fellowship and was elected as a member of Sigma Pi Sigma Honor Society. He completed his Doctor of Philosophy degree in Physics in 2009.